Signal Processing Techniques for Optical Fiber Sensors Using White Light Interferometry

by

Vikram Bhatia

Thesis submitted to the Faculty of the
Virginia Polytechnic Institute and State University
in partial fulfillment of the requirements for the degree of
MASTER OF SCIENCE
in
Electrical Engineering

APPROVED:

Kent A. Murphy, Chairman

Richard O. Claus

Ira Jacobs

Anbo Wang

September, 1993
Blacksburg, Virginia

Signal Processing Techniques for Optical Fiber Sensors Using White Light Interferometry

by

Vikram Bhatia

Kent A. Murphy, Chairman
Electrical Engineering

Conventional fiber optic interferometric sensors employing a monochromatic source prove to be inadequate for applications requiring absolute, real-time value of magnitude and direction of the applied perturbation. This limitation can be overcome by using a broadband light source to extract unambiguous information from the sensor in the wavelength domain. Several variations in the signal processing techniques for white light interferometry are discussed and compared in terms of resolution, bandwidth and cost. A detailed analysis is made of the principle of operation and basic features of the commercially available absolute sensing system. This compact system is self calibrating, has a 100 micro-strain ($\mu\varepsilon$) strain and 2 °C temperature resolution and is ideal for applications in environments where the parameter to be measured is static or quasi-static. High finesse Fabry-Perot cavities are employed to obtain almost an order of magnitude sensitivity improvement over conventional low finesse cavities.

The principle of white light interferometry is extended to absolute axial stain and temperature sensing in two-mode, elliptical-core fibers. Other novel applications, such as to operation of photoinduced refractive index gratings and fiber characterization are proposed.

Acknowledgments

I wish to thank Dr. Kent A. Murphy, my advisor, for his thoughtful guidance and constant encouragement and also for giving me an opportunity to be his first graduate student. I am extremely grateful to Dr. Richard O. Claus for providing me the opportunity to work at FEORC and improve on my laboratory skills. I would also like to thank Dr. Ira Jacobs and Dr. Anbo Wang for their valuable suggestions and useful discussions, which helped in improving the quality of the work presented here.

I am greatly indebted to the employees of Fiber and Sensor Technologies, Inc., specially Jonathan Greene and Tuan Tran, who had some of the best ideas presented in this thesis. You have been great friends and it has been a pleasure working with you.

I would also like to express my gratitude to the staff and students at FEORC who have made every bit of the last twelve months a memorable experience. A special thanks to Marten de Vries, Russ May, Mike Gunther, Kerri Kalli, Linda Jones, Angie Plante, Rajesh Juluri, Mohit Bhatnagar and Mary Burford.

Finally and most importantly, I am grateful to my parents, Mohan and Aruna Bhatia, and my brother, Pankaj, who in spite of their physical absence, have showered all their love and affection on me.

This work was sponsored in part by the Virginia Center for Innovative Technology. Laboratory space and equipment for the majority of the experiments described here, was provided by the Fiber and Sensor Technologies, Inc.

Table of Contents

List of Illustrations

Chapter 1 - Introduction

In the last decade optical fiber sensors have found myriad applications in military, industrial and commercial fields [1]. Due to certain inherent advantages like immunity to electromagnetic interference, large bandwidth, single ended operation, high resolution, small size and weight and a large dynamic range of measurement [2], fiber sensors have replaced many conventional sensors based on pneumatic and electronic principles.

1.1 Classification of Optical Fiber Sensors

Optical fiber sensors can broadly be classified on the basis of principle of operation or the type of measurand. The parameter or perturbation being measured could be displacement, strain, temperature, pressure, velocity, acceleration, acoustic waves, electric current, etc. On the basis of operating principle fiber sensors are categorized as either phase or intensity sensors.

1.1.1 Intensity Sensors

Intensity sensors are simpler to construct and signal process and hence are less expensive. A common type of intensity sensor is shown in Figure 1.1. It consists of an air gap in one arm of a 2x2 coupler, which is illuminated by a LED. This air gap is modulated due to the effects of an external perturbation. The reflected intensity I, from the second fiber forming the air gap, is monitored using a photodetector and the effects of source variation are compensated for by taking the ratio R of I and I_0,

$$R = \frac{I}{I_0}, \tag{1.1}$$

where, I_0 is the intensity in the output arm of the coupler not containing the air gap sensor. Figure 1.2 shows a plot of R versus the gap length d obtained from an actual experiment.

Since multimode fibers are easier to couple light into, they are widely used to fabricate intensity sensors. The main drawback of these types of sensors is that they are susceptible to erroneous results due to bends in any arm of the coupler except for the input arm.

Although these sensors give the absolute value of the air gap and hence the measurand, each sensor requires separate calibration due to a different shapes of the R versus d curves.

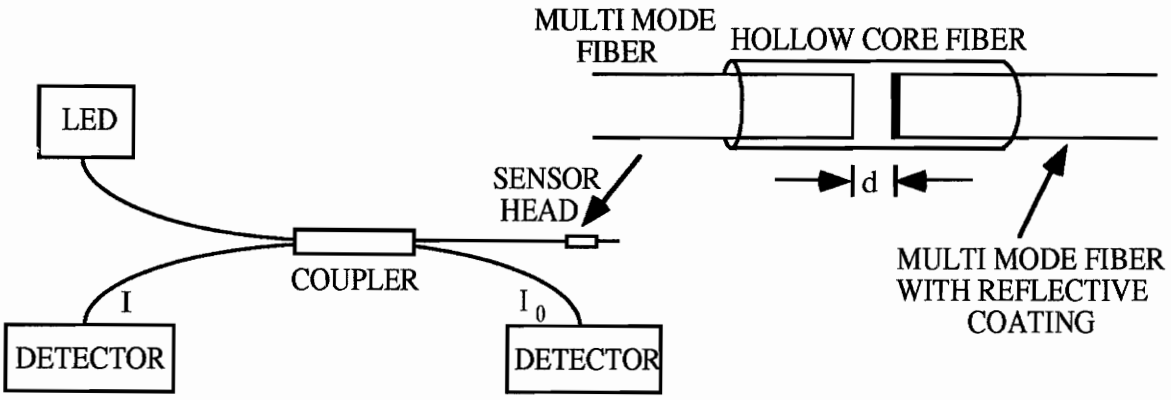

Figure 1.1. A typical configuration of an intensity sensor.

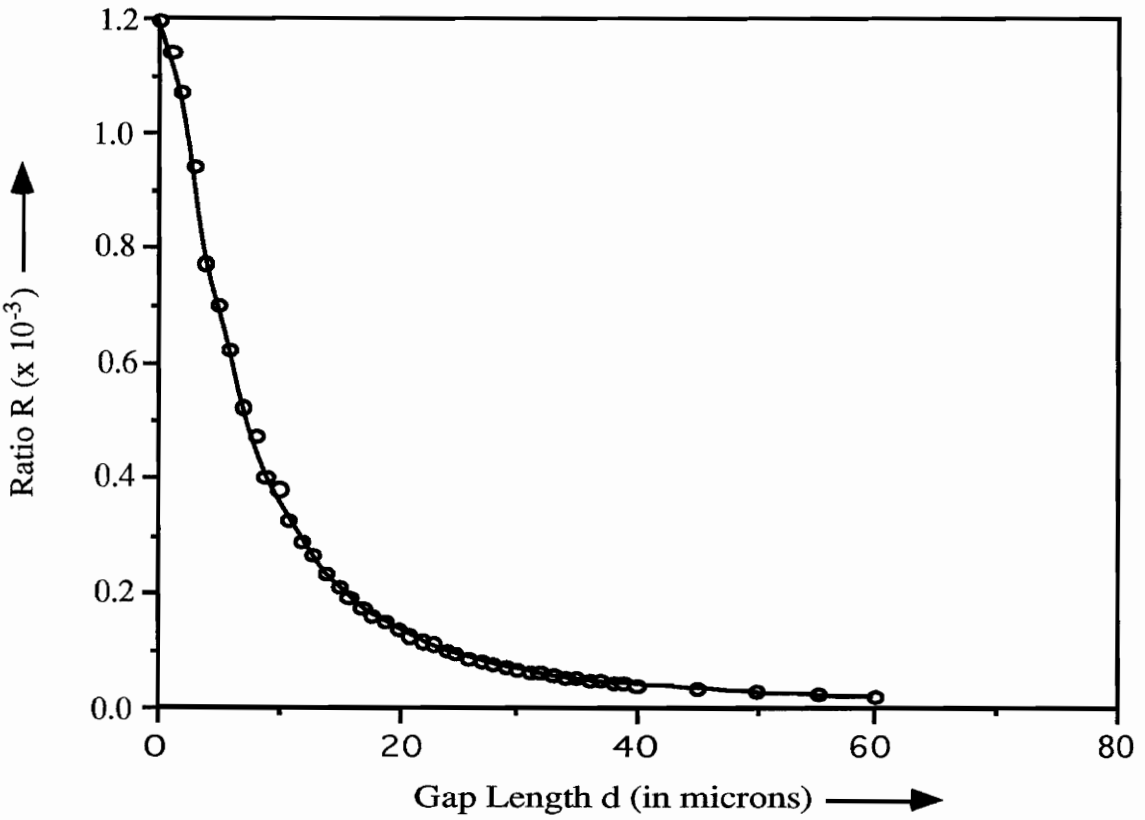

Figure 1.2. Experimental variation of the ratio R with gap length d.

1.1.2 Phase or Interferometric Sensors

Fiber optic phase sensors typically use one of the classical interferometric configurations like Fabry-Perot, Mach-Zender or Michelson for extracting information about the applied perturbation. The phase sensors have two signals, termed as sensing and reference signals (not necessarily propagating in the same fiber), which interfere with each other to provide an intensity modulation at the output. The sensing signal undergoes a phase change due to the perturbation, while the reference arm is kept isolated. A phase difference results between the two signals which manifests itself as an intensity change at the detecting end. If the intensity change can be detected, the applied perturbation can be measured.

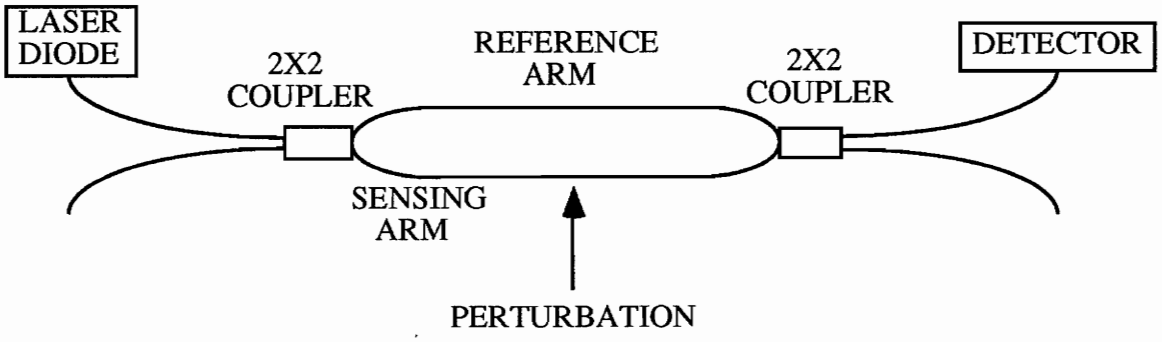

Figure 1.3. A fiber Mach-Zender interferometer.

Figure 1.3 shows a typical fiber Mach-Zender interferometer. It consists of a monochromatic source (emitting at wavelength λ) at one of the input arms of a 2x2 bi-directional single mode coupler. The two output arms of this coupler form the two arms of the interferometer, which are combined by using another 2x2 single mode coupler. Let x be the length of both the sensing (without perturbation) and the reference arms. If an applied perturbation ξ changes the length of the sensing arm by an amount Δx, the phase difference ϕ between the sensing and reference signals is given by,

$$\phi = \frac{2\pi}{\lambda} n\Delta x + \frac{2\pi}{\lambda} x\Delta n \,, \tag{1.2}$$

where, n is the core refractive index and Δn is the change in the value of n due to the perturbation.

At the output the two signals are combined and interfere if and only if the effective path length difference (ΔL) between the two signals is less than the coherence length L_C of the source, where,

$$\Delta L = \Delta x + x\frac{\Delta n}{n}, \tag{1.3}$$

such that,

$$\phi = \frac{2\pi}{\lambda} n \Delta L . \tag{1.4}$$

For a fiber Mach-Zender interferometer, the percentage change in length $\Delta L/L$ is very small compared to the corresponding refractive index change $\Delta n/n$ such that,

$$\phi = \frac{2\pi}{\lambda} x \Delta n . \tag{1.5}$$

Thus the phase change per unit perturbation ξ is given by,

$$\frac{\phi}{\xi} = \frac{2\pi}{\lambda} x \frac{\Delta n}{\xi} . \tag{1.6}$$

If the sensor is operated in a region where the change in refractive index (Δn) is proportional to ξ, i.e., if $\Delta n/\xi$ is a constant then the phase difference is directly proportional to the perturbation,

$$\phi \propto \xi . \tag{1.7}$$

The intensity I at the detector is given by,

$$I = I_{dc} + I_{ac}\cos(\phi) , \tag{1.8}$$

where, I_{dc} and I_{ac} correspond to the dc and ac components, respectively, of the output intensity, as shown in Figure 1.4. A fringe is defined as the change of intensity I between two consecutive maxima or two consecutive minima. Neglecting I_{dc}, we have from Equations (1.7) and (1.8),

$$I \propto \cos(\xi) . \tag{1.9}$$

If we operate the sensor such that the output intensity stays within the linear portion of the transfer function curve (Figure 1.5), the output intensity is directly proportional to ξ,

$$I \propto \xi . \tag{1.10}$$

The Q-point, or the quiescent-point, is the point in the middle of the linear region. The sensor is most sensitive if it is operated at the Q-point, while the sensitivity reduces drastically a quarter of a fringe on both sides.

The Extrinsic Fabry-Perot Interferometer (EFPI), Intrinsic Fabry-Perot Interferometer (IFPI) and the Temperature Insensitive Michelson Interferometer (TIMI) are some other common phase sensor in use these days.

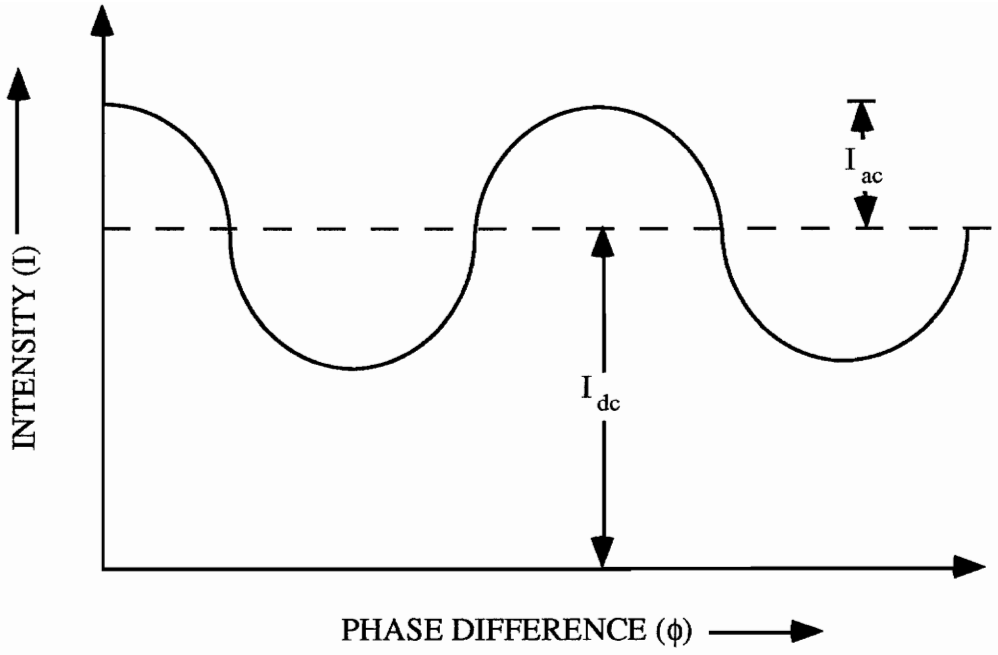

Figure 1.4. Output intensity I as a function of the phase difference ϕ.

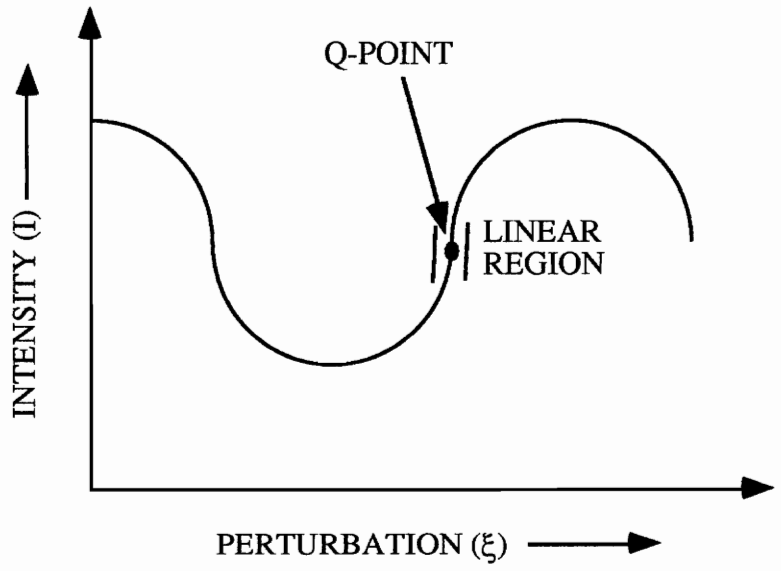

Figure 1.5. Intensity (I) variation with applied perturbation (ξ).

Although the phase sensors are extremely sensitive and hence offer excellent resolution, the problems encountered are, 1) complex signal processing techniques to count fringes, 2) Q-point stabilization problems due to laser wavelength drift, and 3) inability to detect whether an increase or decrease in the value of the perturbation took place if the operating point is a maxima or a minima on the transfer function curve. The phase sensors are differential measurement systems and lose information about the perturbation after the system is powered off and turned on again.

1.2 Need for an Absolute Fiber Optic Sensor

In order to fully utilize the capability of optical fiber sensors, an effort is being made to develop a sensor which gives absolute, real time measurement of various parameters. This sensor should have a high resolution like the phase sensors but should not be limited by the Q-point stabilization problems or the inability to provide directional information. Other desired features include bend insensitivity, large bandwidth and dynamic range. This kind of a sensor should be self calibrating and should possess the capability to retain information about the perturbation after its turned off, so that it can be taken to any remote location for measurement purposes.

Wang *et al.* [3] proposed the split spectrum approach in which they used an intensity sensor with an edge filter at the end of the multimode fiber in order to reflect a certain wavelength spectrum back as a reference signal. Although unlike other intensity sensors this sensor is supposed to be bend insensitive, it does not offer a high resolution and requires a separate calibration process for each sensor.

The above intensity sensor uses wavelength as the basis for sensing and it was thought that a phase sensor, also using wavelength as the sensing parameter, could be fabricated to give an absolute fiber sensor. Although this approach, termed as white light interferometry, has been known since a long time, to our knowledge nobody has been able to fabricate a complete commercially available system because the combination of the right source, sensor, and detection scheme has proved to be elusive.

The work described here aims at developing an almost 'ideal' fiber optic sensor which can overcome the limitations of intensity and phase sensors, while at the same time retaining the inherent advantages of these sensors. This type of sensor would use white light

interferometry in EFPI cavities and would have a real time, absolute output with high resolution, dynamic range and frequency response. White light interferometry in elliptical-core, two-mode fibers would also be investigated.

1.3 Overview

Chapter 2 describes the principle of operation of the proposed sensor, namely, white light interferometry. In Chapter 3 we review the theory behind high finesse Fabry-Perot cavities. Chapter 4 involves the description of sensor fabrication, the analysis of the experimental results obtained and techniques to multiplex a large number of sensors. Some variations of white light interferometry are discussed in Chapter 5. The theory behind the operation of a distributed, absolute sensor using a two-mode, elliptical-core fiber is then described in Chapter 6. Chapter 7 summarizes the advantages of the absolute sensor, its potential applications and identifies future areas of research in this field.

Chapter 2 - White Light Interferometry in Fabry-Perot Cavities

In this chapter we discuss Fabry-Perot cavities and the principle behind the operation of the absolute sensing system, namely, white light interferometry.

2.1 Fiber Fabry-Perot Interferometers

Fiber Fabry-Perot Interferometers (FPI) are used in two basic configurations termed Intrinsic and Extrinsic. The Intrinsic Fabry-Perot Interferometer (IFPI) is shown in Figure 2.1. It uses an isolated laser diode (LD) as the source. The Fabry-Perot cavity is formed by fusing a small length of a single mode fiber to one of the output arms of a bi-directional 2x2 coupler. The signals that form the interference pattern, R and S, are reflected from two ends of this fused fiber. The reflected intensity is monitored to detect any variations in the refractive index or length of the Fabry-Perot cavity due to applied perturbations like strain and temperature. The high temperature sapphire sensor proposed by Wang *et al.* [4] and the balanced sensor proposed by Lee and Taylor [5] are good examples of IFPIs.

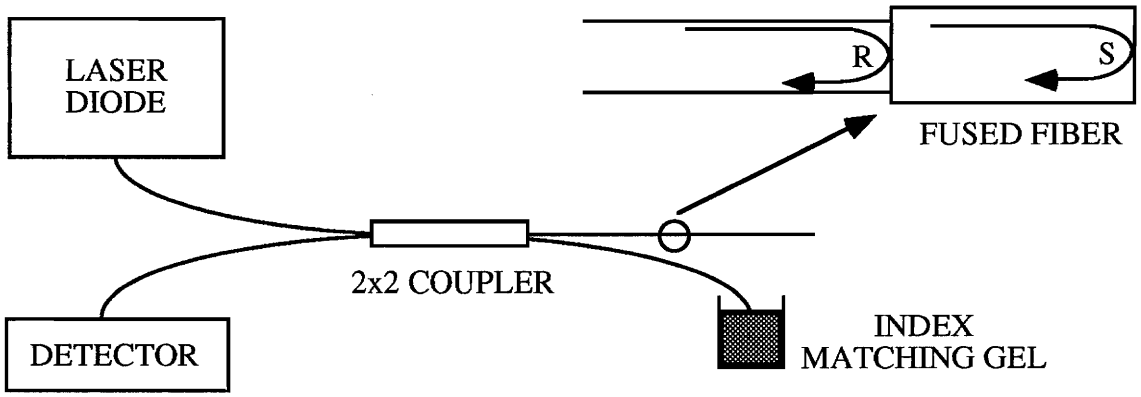

Figure 2.1. The Intrinsic Fabry-Perot Interferometer (IFPI).

IFPIs suffer from many inherent drawbacks. Once the reflecting fiber is fused to the input fiber the gage length cannot be varied. Also the length of the fused fiber should be less than

half the coherence length of the LD and so for a source with a small coherence length, this sensor is difficult to fabricate. Also the external perturbation might change both the cavity length and the refractive index, causing the phase difference between the sensing and reference signals to have a non-linear dependence on the applied perturbation.

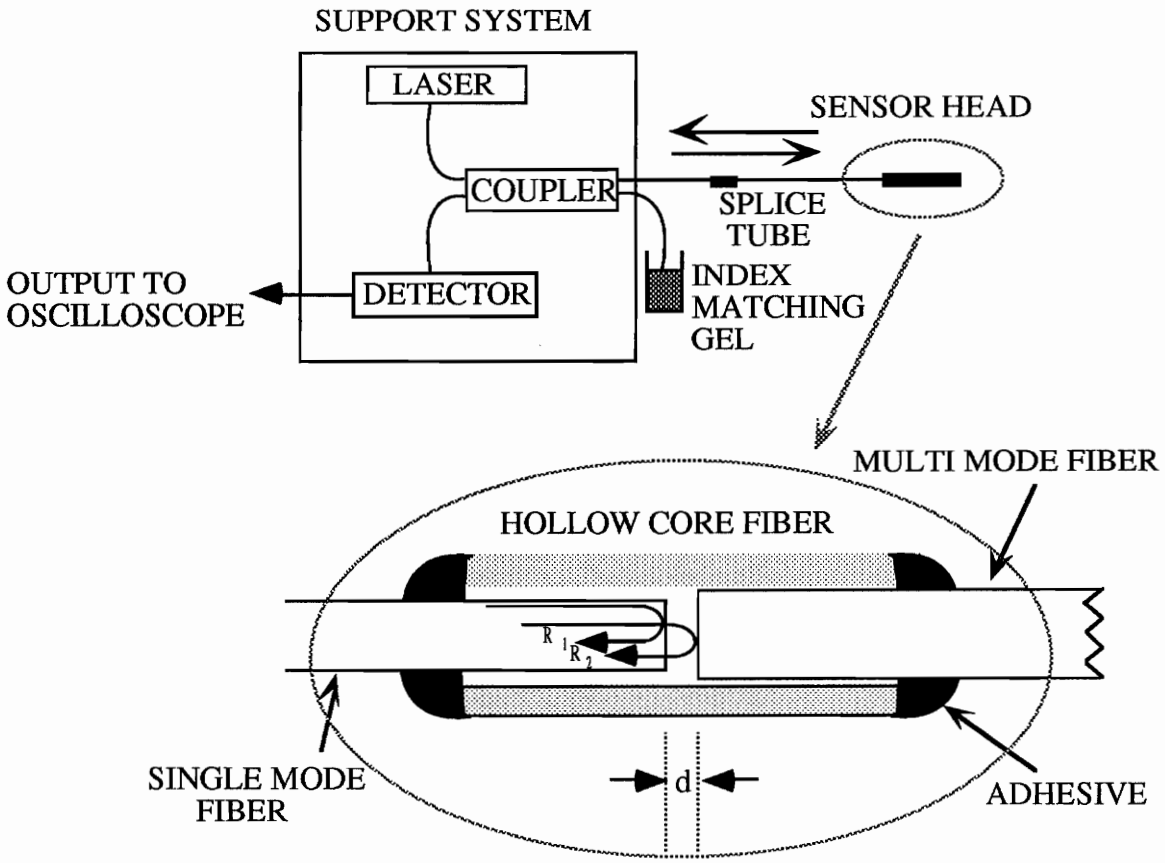

Figure 2.2. The Extrinsic Fabry-Perot Interferometer (EFPI).

Thus, a need was felt for a FPI which is easy to construct and has only the cavity length (and not the refractive index) as the function of the measurand. In 1990, the Extrinsic Fabry-Perot Interferometer (EFPI) was proposed [6]. This sensor uses air as the Fabry-Perot cavity and its basic configuration is shown in Figure 2.2. The cavity is formed between an input single mode fiber and a reflecting single mode or multimode fiber. For uncoated fiber ends, a 4% Fresnel reflection results at both ends of the cavity. The first

reflection, called the reference reflection, is independent of the applied perturbation. The second reflection, termed the sensing reflection, is dependent on the length of the cavity, d, which is modulated by the applied perturbation. These two reflections interfere (provided $2d<L_C$, the LD's coherence length) and the intensity I at the detector varies as a function of the cavity length,

$$I = I_1 + I_2 + 2\sqrt{I_1 I_2}\cos(\phi)\,, \tag{2.1}$$

where (Figure 2.3), I_1 is the intensity of the reference signal, I_2 is the intensity of the sensing signal and ϕ is given by,

$$\phi = \frac{4\pi}{\lambda} d\,, \tag{2.2}$$

where, λ is the emission wavelength of the LD.

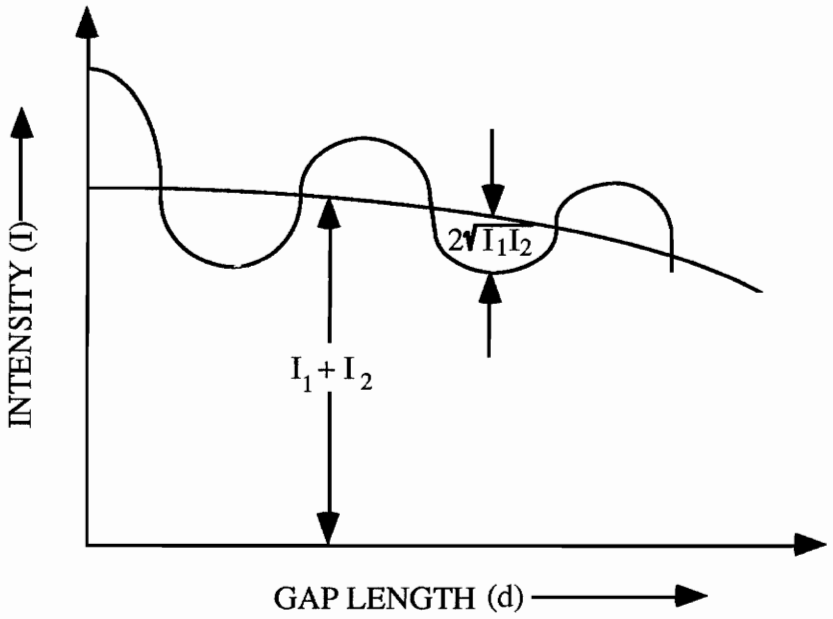

Figure 2.3. Typical output from an EFPI.

Putting $I_{dc} = I_1 + I_2$ and $I_{ac} = 2\sqrt{I_1 I_2}$,

$$I = I_{dc} + I_{ac}\cos(\phi)\,. \tag{2.3}$$

Neglecting I_{dc}, we get,

$$I = I_{ac}\cos(\frac{4\pi}{\lambda}d)\,. \tag{2.4}$$

The fringe contrast C is given by,

$$C = 2I_{ac} = 4\sqrt{I_1 I_2} = \frac{I_{max} - I_{min}}{I_{max} + I_{min}}, \qquad (2.5)$$

where, I_{max} and I_{min} are the maximum and minimum intensities, respectively, at the output. In general, the fringe contrast reduces with d, as I_2 falls with increasing d (see Figure 1.2). If the sensor is operated at the Q-point, the output intensity is proportional to the gap length, d,

$$I \propto d .$$

To find the magnitude of the perturbation, either the sensor has to be maintained at the Q-point or if the perturbation is large, a fringe counting technique has to be employed. This signal processing increases the cost of the system dramatically. Also this sensor is extremely sensitive if it is operated at the Q-point but the sensitivity reduces dramatically a quarter of a fringe away on both sides (Figure 2.4). Thus, the sensitivity becomes a function of the gap length d.

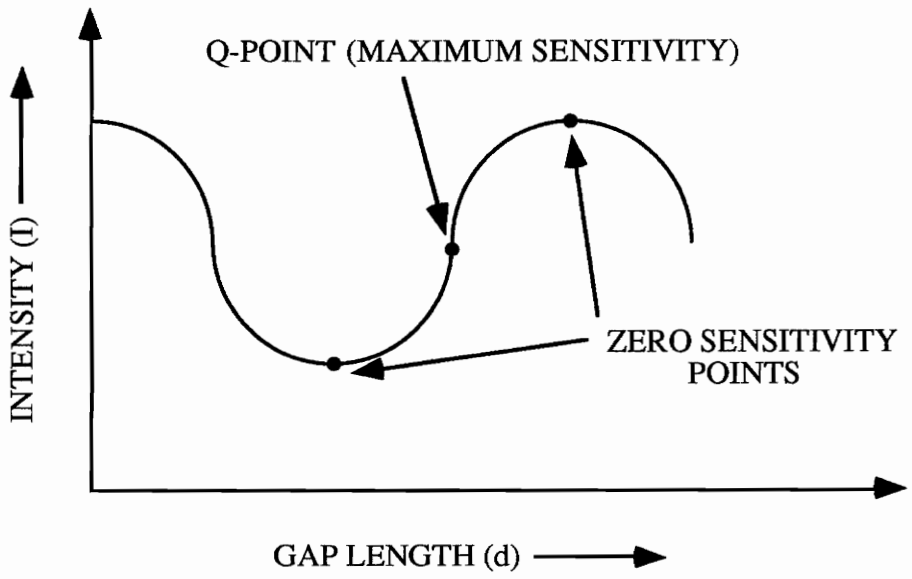

Figure 2.4. Sensitivity variation of an EFPI along its transfer function curve.

2.2 Existing Direction Detecting Techniques

If we can somehow obtain two signals which are in quadrature (or 90° out of phase) there

would be at least one signal which is not at the minimum sensitivity point on the transfer function curve. These quadrature phase-shifted signals would also enable us to deduce directional information about the measurand.

As is obvious from Equation 2.4, the output intensity, I, is a function of both the gap length, d, and the wavelength, λ, and is plotted in Figure 2.5. Thus, there are two ways to obtain signals which are 90° out of phase 1) Quadrature Phase-Shifted EFPI and, 2) the two wavelength approach.

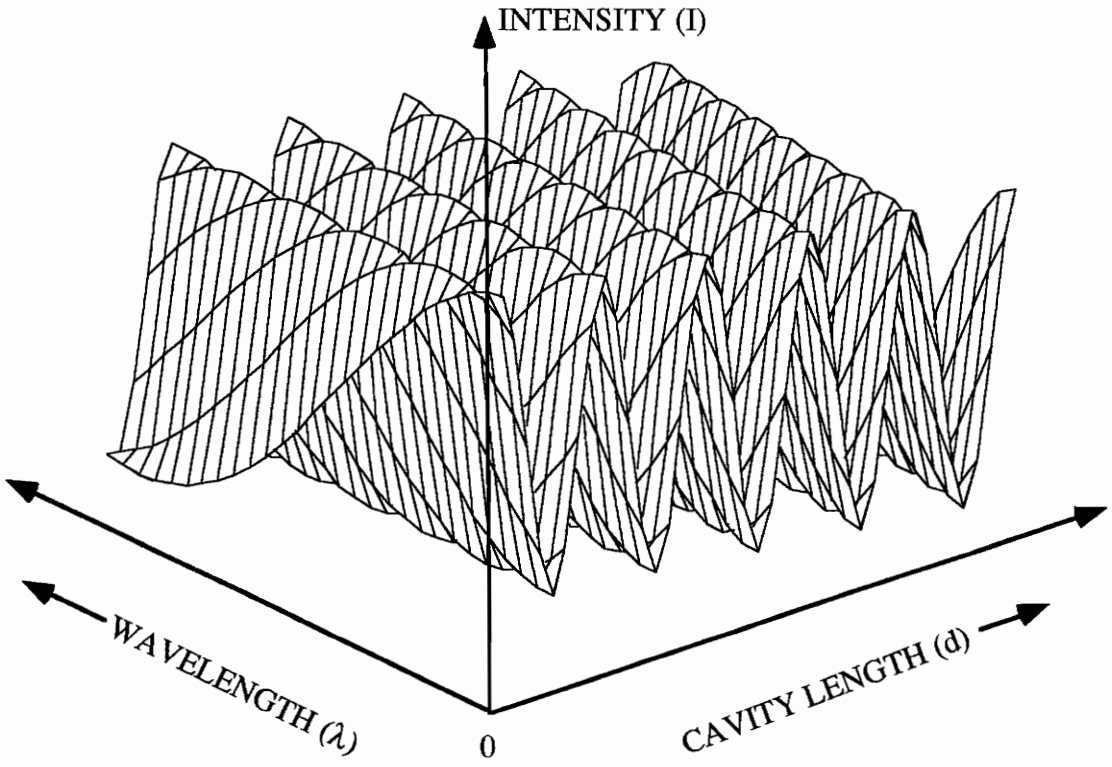

Figure 2.5. Intensity output of an EFPI as a function of the cavity length (d) and wavelength (λ).

2.2.1 Quadrature Phase-Shifted EFPIs

The Quadrature Phase-Shifted EFPIs proposed by Murphy *et al.* [7] requires two EFPI cavities in close proximity to obtain two signals in quadrature. The arrangement of this

sensor is shown in Figure 2.6. The two Fabry-Perot cavities are formed between a pair of longitudinally separated input single mode fibers (cladding diameter 125 μm) and a 250 μm reflecting multimode fiber. If d_1 be the cavity length of the top cavity and d_2 be that of the lower one, the phase difference between the two signals (from Equation 2.3) is,

$$\Delta\phi = \frac{4\pi}{\lambda} d_1 - \frac{4\pi}{\lambda} d_2 . \tag{2.6}$$

For the two signals to be out of phase by 90°, we require $\Delta\phi$ to be an odd multiple of $\pi/2$,

$$\frac{4\pi}{\lambda} (d_1 - d_2) = (2n + 1)\frac{\pi}{2} , \tag{2.7}$$

or,

$$d_1 - d_2 = \frac{(2n + 1)\lambda}{8} , \tag{2.8}$$

where, n is any integer.

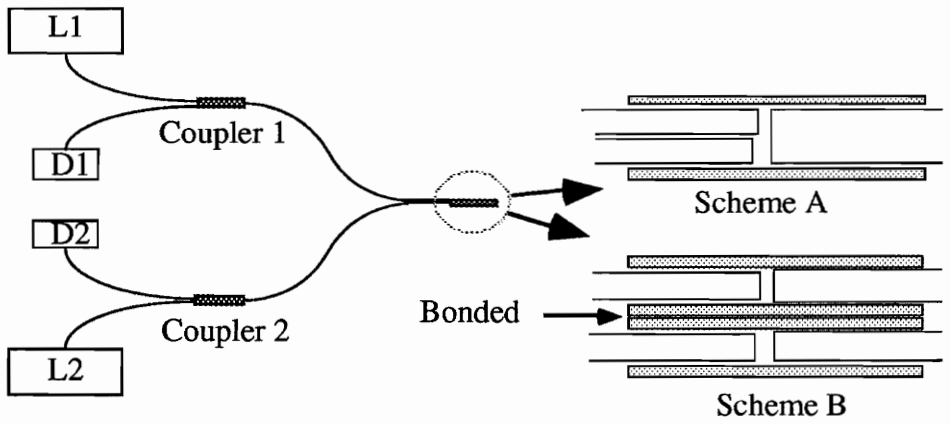

Figure 2.6. Two configurations of Quadrature Phase-Shifted EFPIs [7].

For the simplest case (n=0),

$$d_1 - d_2 = \frac{\lambda}{8} . \tag{2.9}$$

Although this sensor gives directional information, complex signal processing techniques are required. Also the difference between d_1 and d_2 can only be fixed, discrete values, which makes the sensor fabrication difficult. Moreover, cyclic strain could cause the two signals to go out of quadrature.

2.2.2 Two Wavelength approach

The two wavelength approach utilizes a single EFPI with two optical sources, as shown in Figure 2.7. A 4x4 coupler is used to obtain the intensity modulated signal from an EFPI. Bandpass filters with center wavelength λ_1 and λ_2 and bandwidths less than half the difference between the two wavelengths are employed to get two signals in quadrature, such that,

$$\frac{4\pi}{\lambda_1} d - \frac{4\pi}{\lambda_2} d = (2n + 1)\frac{\pi}{2}, \tag{2.10}$$

or,

$$d = \frac{(2n + 1)}{8}\left(\frac{\lambda_1\lambda_2}{\lambda_2 - \lambda_1}\right). \tag{2.11}$$

For n=0,

$$\frac{1}{\lambda_2} = \frac{1}{\lambda_1} - \frac{1}{8d}. \tag{2.12}$$

Here again for a fixed wavelength λ_1, the second wavelength λ_2 becomes a function of the gap d and hence the two signals are in quadrature for only fixed values of gap length, d. So unless λ_2 can be changed using a feedback loop, or the change in gap is so small that the two wavelengths are almost always in quadrature, this scheme is not feasible.

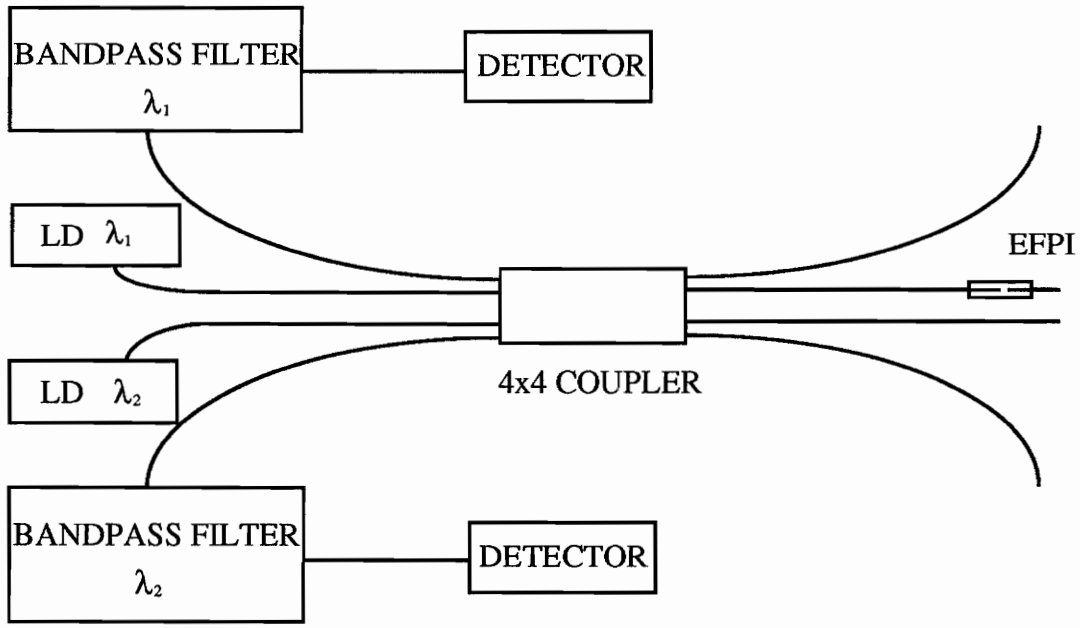

Figure 2.7. Experimental setup for the two wavelength approach.

2.3 White Light Interferometry

If a broadband source like a white light source is used instead of a LD and the phase difference $\Delta\phi$ between two fixed wavelengths λ_1 and λ_2 is monitored,

$$\Delta\phi = \frac{4\pi}{\lambda_1} d - \frac{4\pi}{\lambda_2} d . \qquad (2.13)$$

A white light source can be thought to be equivalent to a large number of LDs placed successively in the wavelength domain. Since, ϕ in Equation (2.2) is a function of λ, the outputs due to each assumed LD differ in phase and hence, in output intensity from one another. This phase difference can only be obtained if we utilize an optical spectrum analyzer and measure the broadband response in the wavelength domain. This measurement technique which employs a broadband source and an optical spectrum analyzer to extract information from interferometers is termed as white light interferometry [8]. The most basic setup of this system using an EFPI is shown in Figure 2.8. The signal processing in this setup can be done by the constant wavelength or the constant phase techniques [9].

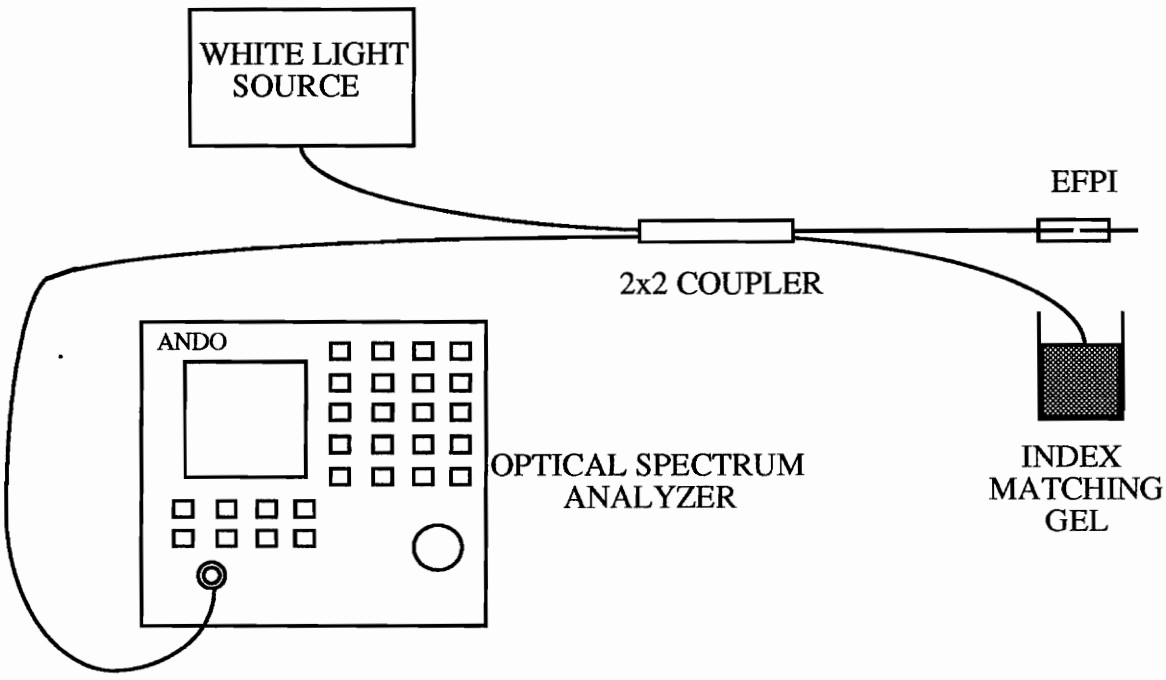

Figure 2.8. Setup for performing white light interferometry in EFPI cavities.

2.3.1 Constant Wavelength Technique

From Equation (2.13),

$$d = \frac{\lambda_1\lambda_2}{4\pi(\lambda_2 - \lambda_1)}\Delta\phi \ . \tag{2.14}$$

Thus, if the phase difference $\Delta\phi$ between two wavelengths, λ_1 and λ_2, is known, the gap d can be determined absolutely. This method which uses two fixed wavelengths is called the Constant Wavelength Technique.

2.3.2 Constant Phase Technique

In the constant wavelength technique, it becomes cumbersome to compute the exact phase difference between any two fixed wavelengths. So, usually in white light interferometry the constant phase technique is employed. A phase difference value (generally 2π or its multiples) is fixed, such that,

$$\Delta\phi = 2n\pi = \frac{4\pi}{\lambda_1}d - \frac{4\pi}{\lambda_2}d \ , \tag{2.15}$$

or,

$$d = \frac{n(\lambda_1\lambda_2)}{2(\lambda_2 - \lambda_1)} \ , \tag{2.16}$$

where, n is a whole number. For n=1, we have,

$$d = \frac{(\lambda_1\lambda_2)}{2(\lambda_2 - \lambda_1)} \ , \tag{2.17}$$

and we simply have to determine two wavelengths corresponding to two successive maxima or minima on the optical spectrum analyzer. The simulated I versus λ curves for different cavity lengths are shown in Figures 2.9 (a), (b) and (c), where it is assumed that the fringe constant does not vary with changing cavity lengths.

2.4 Advantages of White Light Interferometry

An Absolute EFPI (AEFPI) using white light interferometry overcomes many of the limitations encountered in the use of the conventional EFPI and the Quadrature Phase-shifted EFPI. The improvements include :

1) Ability to detect the cavity length, d, absolutely and not differentially, without using two EFPI cavities or two LDs.
2) Reduction of signal processing as fringe counting is eliminated.
3) Self-calibration and real-time outputs since optical source wavelengths are absolute.

4) Shift in Q-point due to source drift is no longer a problem. In fact, shift in spectrum of the broadband source has no effect on the system whatsoever.

5) Large dynamic range, unlike the conventional EFPI.

6) Reduced system cost as the need for isolated LDs and fringe counting equipment is eliminated.

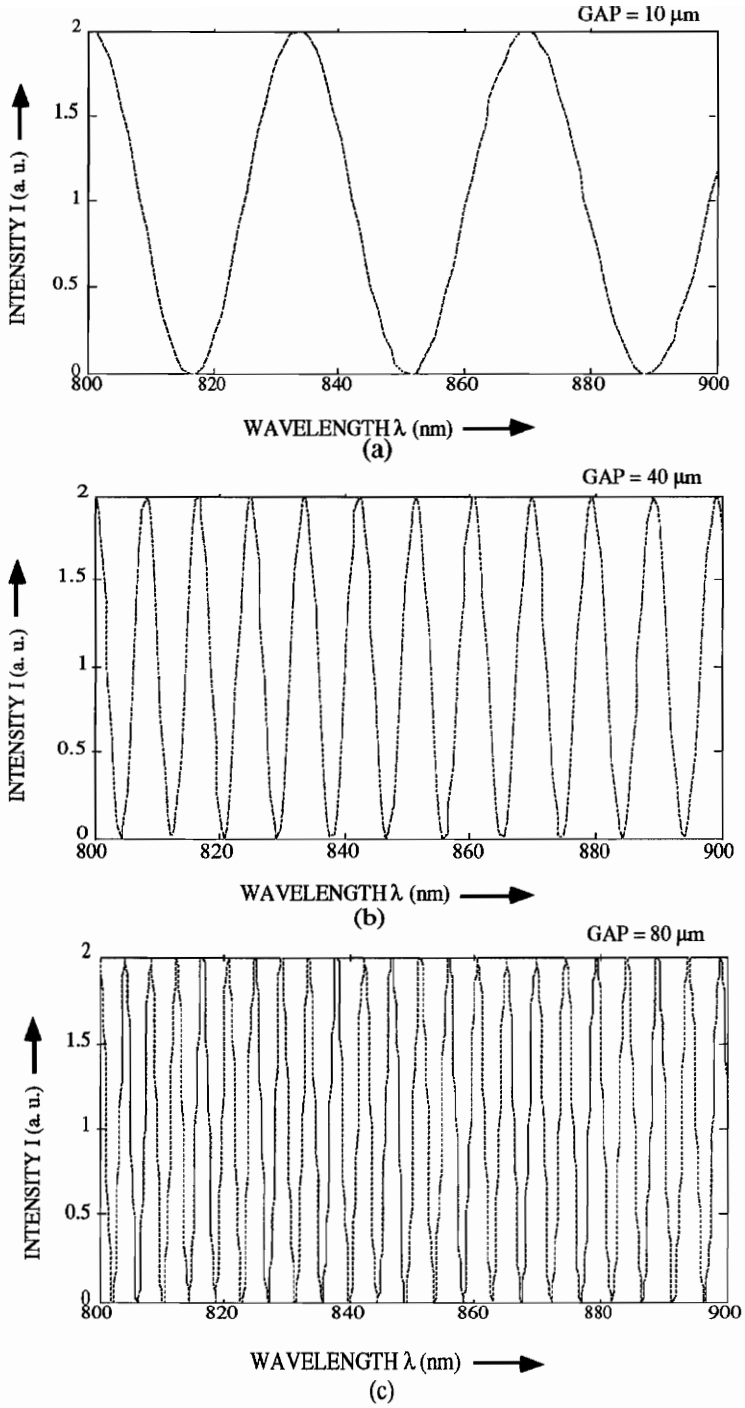

Figure 2.9. Intensity versus wavelength for various values of cavity lengths, (a) 10 μm, (b) 40 μm and (c) 80 μm.

Chapter 3 - High Finesse EFPI Cavities

In the analysis of EFPI cavities in the previous chapter, we have assumed that the multiple reflections from the two air/glass interfaces (*i.e.*, other than the first-order reflections), do not contribute to the intensity modulation at the output and so there is a simplified two beam interference. This assumption is justified because the Fresnel reflection coefficient, r (for normal incidence),

$$r = \left(\frac{n_1 - n_2}{n_1 + n_2}\right)^2 , \tag{3.1}$$

for the air/glass interface is just 4% (for $n_1 = 1.48$ and $n_2 = 1.00$), where n_1 and n_2 are the refractive indices of the two media forming the interface. As shown in Figure 3.1, the second and higher order reflections have negligible amplitudes. A is the amplitude of the incident wave. The amplitudes of the higher order reflections are further reduced by losses due to multiple traversal of the air gap.

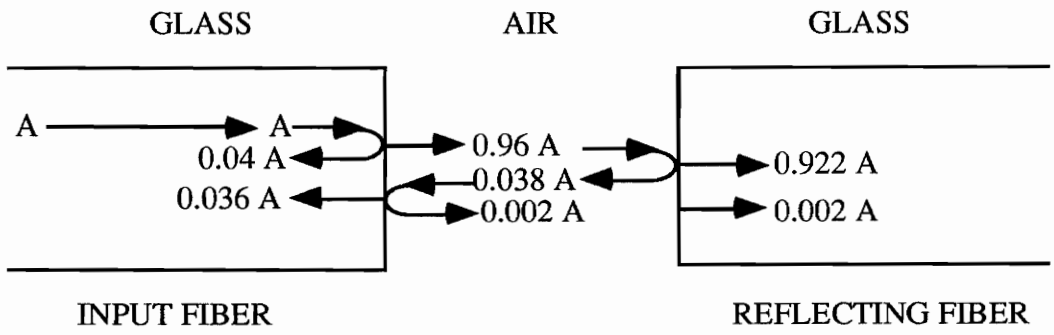

Figure 3.1. First and higher order reflections in a conventional EFPI cavity.

But if n_1 can be made higher by coating the ends of the input and the reflecting fiber with multilayer dielectric films or with partially transparent films of metals, r can be increased and the amplitude of the second and higher order reflections would become high enough to cause a change in the intensity distribution at the detector.

In this chapter we discuss the modification in the EFPI fringe pattern obtained from fibers coated with thin metal films. We analyze the characteristics of such cavities and investigate the improvement in the sensitivity due to the use of metal coatings.

3.1 Finesse of a Lossless Fabry-Perot Cavity

Consider the EFPI shown in Figure 3.2, with the two single mode fibers which have thin metal coatings. Let input light of amplitude A be incident on the i^{th} interface (i = 1, 2 for the two interfaces). Assuming that the mirrors have no absorption, there is a $\pi/2$ phase shift between the transmitted and the reflected waves at both interfaces. Let r_i, t_i be the mirror reflectance and transmittance, respectively. Then the reflected and transmitted amplitudes are given by $jA\sqrt{r_i}$ and $jA\sqrt{t_i}$, respectively. Since both the mirrors are assumed to be lossless, $r_i + t_i = 1$.

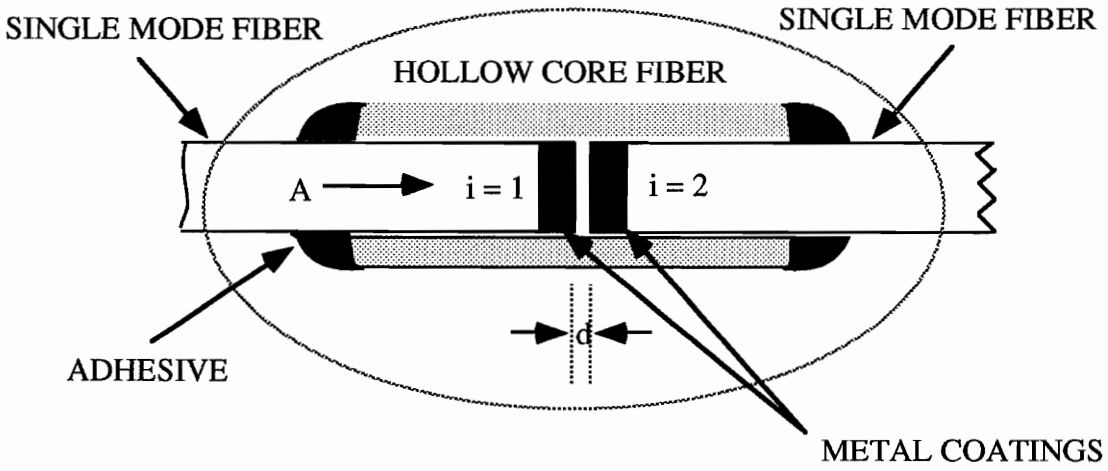

Figure 3.2. A high finesse EFPI cavity.

The amplitude of the resulting transmitted wave (A_T) is sum of all the waves that are transmitted through the second interface. The ratio of the transmitted power to the incident power is called the transmittance, T, of the cavity and it can be shown that,

$$T = \left|\frac{A_T}{A}\right|^2 = \frac{t_1 t_2}{1 - r_1 r_2 - 2\sqrt{r_1 r_2}\cos(\phi)}, \qquad (3.2)$$

or,

$$T = \frac{(1 - r_1)(1 - r_2)}{1 - r_1 r_2 - 2\sqrt{r_1 r_2}\cos(\phi)}, \tag{3.3}$$

where, $\phi = 4\pi d/\lambda$ is the round trip phase shift in the cavity.

Similarly, the reflectance, R, of the cavity is the ratio of the reflected power to the incident power and is given by [10],

$$R = \frac{r_1^2 + r_2^2 + 2\sqrt{r_1 r_2}\cos(\phi)}{1 - r_1 r_2 - 2\sqrt{r_1 r_2}\cos(\phi)}. \tag{3.4}$$

Assuming $r_1 = r_2$ (and hence, $t_1 = t_2$), we get,

$$T = \frac{(1 - r)^2}{1 - r^2 - 2r\cos(\phi)}, \tag{3.5a}$$

or,

$$T = \frac{1}{1 + \frac{4r}{(1 - r)^2}\sin^2(\phi/2)}. \tag{3.5b}$$

Letting,

$$k = \frac{4r}{(1-r)^2}, \tag{3.6}$$

we get,

$$T = \frac{1}{1 + k\sin^2(\phi/2)}. \tag{3.7}$$

Similarly,

$$R = \frac{k\sin^2(\phi/2)}{1 + k\sin^2(\phi/2)}. \tag{3.8}$$

Plotting T and R against ϕ in Figure 3.3 (a) and (b) respectively, for different values of r, we obtain what is known as the Airy Function. Figure 3.4 is the plot of R and T for r = 0.95. As is obvious, the two patterns are complementary in that, T + R = 1.

3.1.1 Effect of Low Mirror Reflectance

For small values of r (r<<1), as in a conventional EFPI with uncoated ends, k in Equation (3.6) is small and Equation (3.7) and (3.8) reduce to,

$$T = 1 - \frac{k}{2}(1 - \cos\phi), \tag{3.9}$$

$$R = \frac{k}{2}(1 - \cos\phi). \tag{3.10}$$

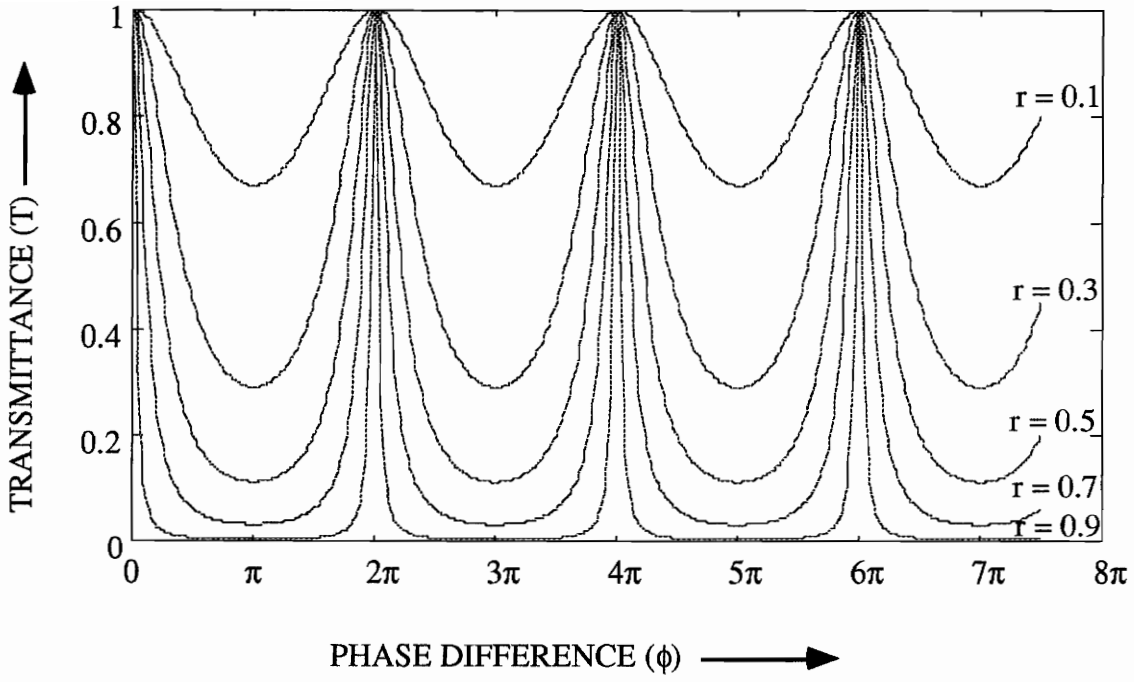

(a)

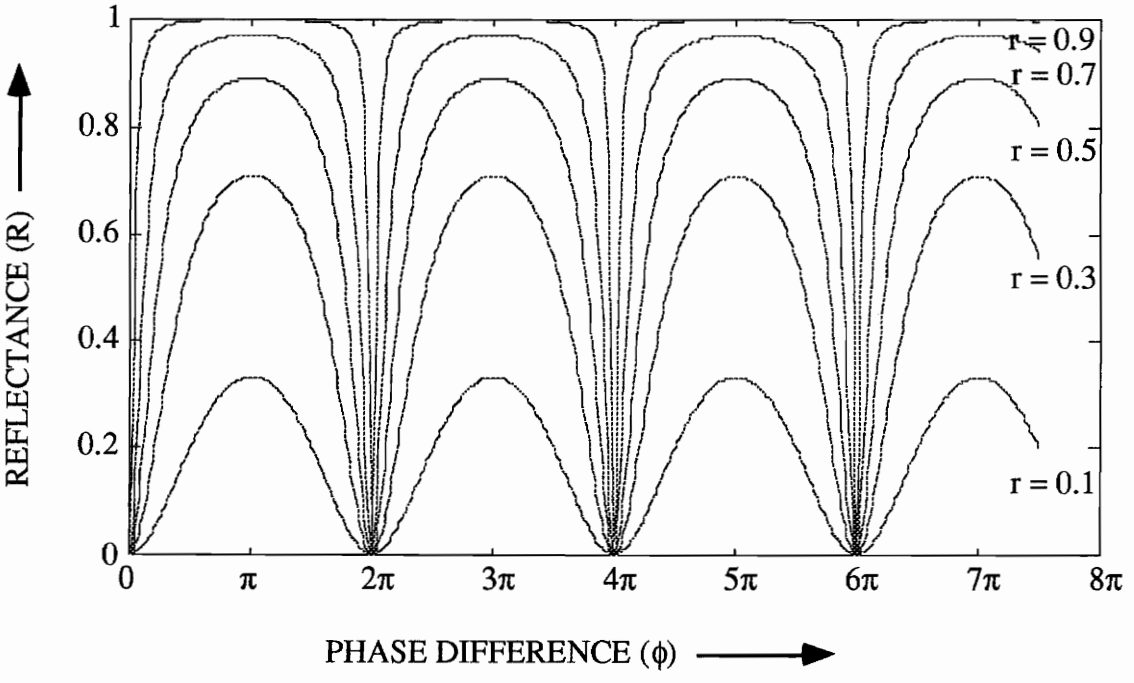

(b)

Figure 3.3. (a) Transmittance (T) and (b) Reflectance (R) versus phase difference (ϕ).

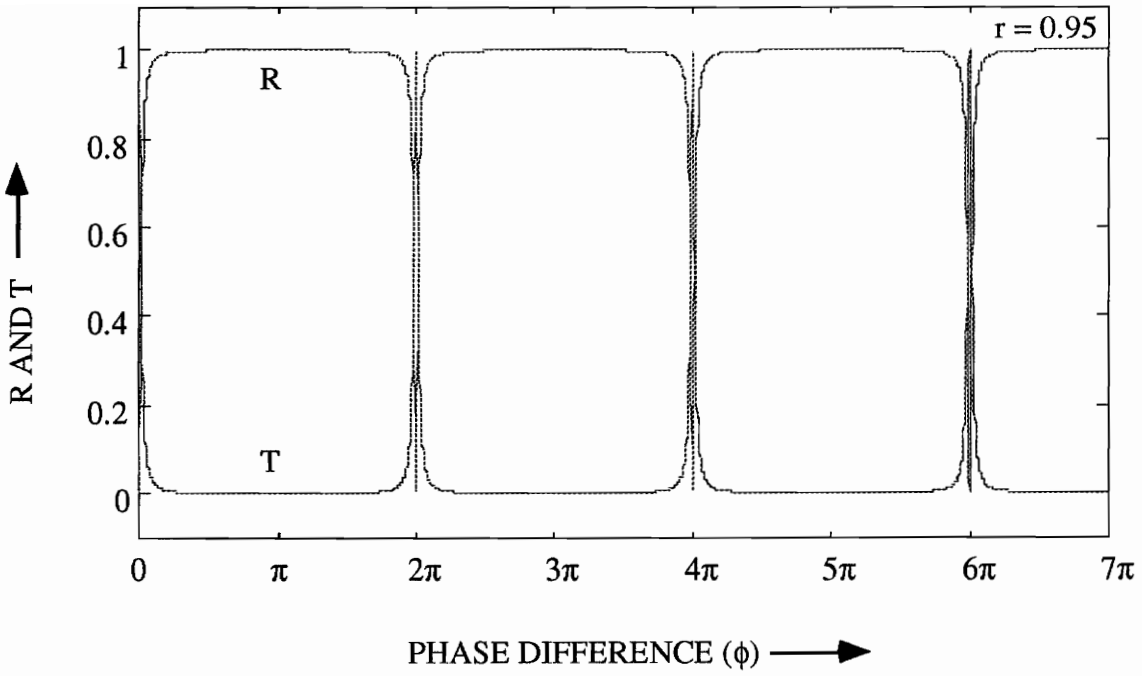

Figure 3.4. Reflectance (R) and Transmittance (T) for r = 0.95.

Equation (3.10) is similar to Equation (2.3) in Chapter 2,

$$I = I_{dc} + I_{ac}\cos\phi \ ,$$

for the two beam interferometer and we get a sinusoidal intensity modulation at the output.

3.1.2 Effect of High Mirror Reflectance

As r is increased, k in Equation (3.6) becomes larger and so the dc term (k/2) in Equation (3.10) increases and that (1-k/2) in Equation (3.9) decreases. Also, as is evident from Figure 3.3, the intensity of the minima of the transmitted pattern reduces and the maxima peaks become compressed.

Such a pattern is generally characterized by a parameter called the finesse. The finesse of a cavity is defined as the ratio of the separation between adjacent transmitted peaks and the half width of a peak. If ε be the half width (Figure 3.5) of a peak,

$$\frac{1}{1+ k\sin^2(\varepsilon/4)} = \frac{1}{2} \ . \qquad (3.11a)$$

For large values of k, we have a small ε and Equation (3.11) reduces to,

$$1+k\left(\frac{\varepsilon}{4}\right)^2 = 2\,, \tag{3.11b}$$

or,

$$\varepsilon = \frac{4}{\sqrt{k}}\,. \tag{3.12}$$

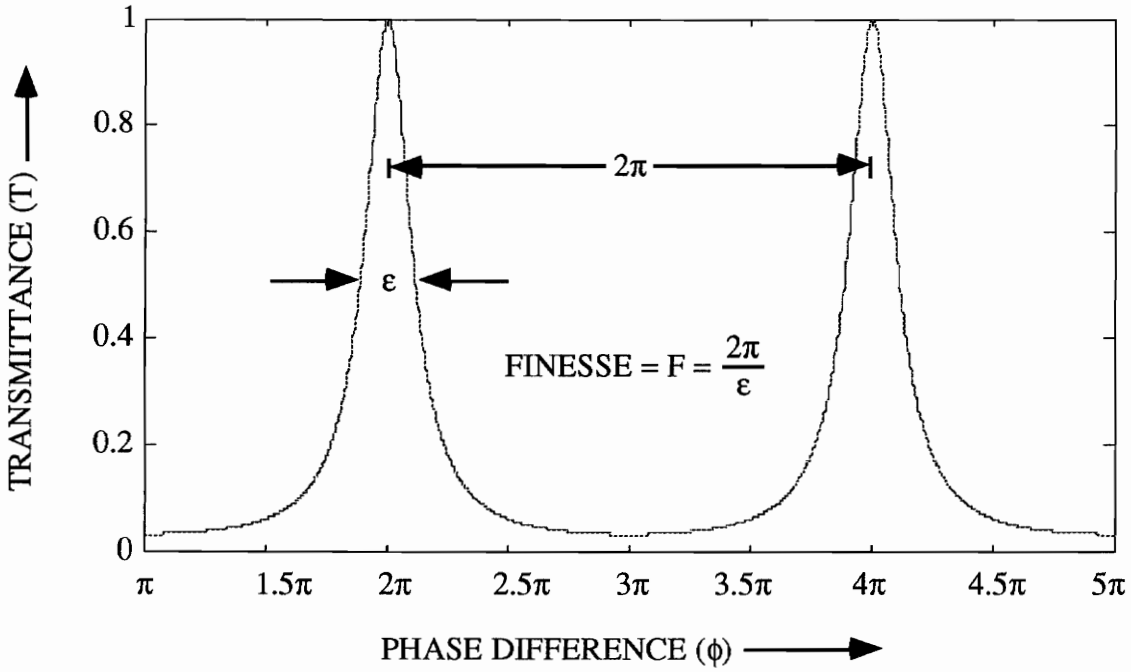

Figure 3.5. Finesse (F) of a Fabry-Perot cavity.

The finesse, F, is then,

$$F = \frac{2\pi}{\varepsilon} = \frac{\pi\sqrt{k}}{2}\,, \tag{3.13}$$

or,

$$F = \frac{\pi\sqrt{r}}{1-r}\,. \tag{3.14}$$

Figure 3.6 is the plot of the finesse F versus the mirror reflectance, r. The finesse increases gradually with r initially and for r > 0.95, its value becomes very high [11].

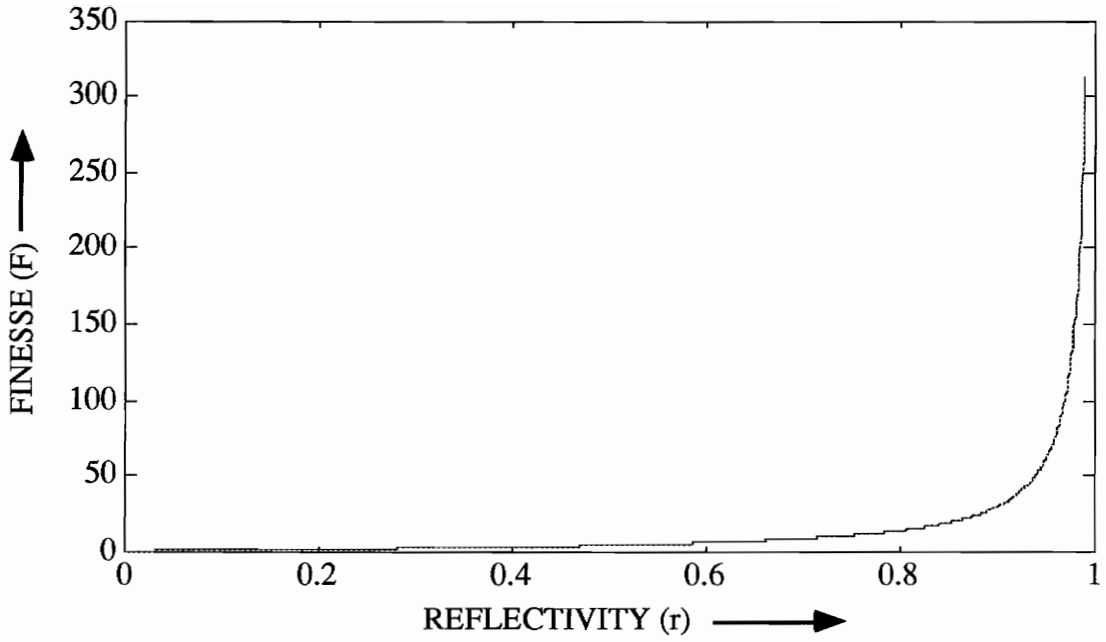

Figure 3.6. Change in the finesse (F) of a Fabry-Perot cavity with interface reflectivity (r).

3.2 Metal films as Reflecting Surfaces

Although both metal and dielectric films can be used to increase the finesse of the FPI cavity, for the application in white light interferometry, metal films are more suitable. The reason for this is that the reflection coefficient (r) has a high value over a larger wavelength band in metal films than in their dielectric counterparts.

When thin metal films are used to increase the finesse of the EFPI cavity, there are two major deviations from the ideal case [12]:

1) Metal films absorb light and hence the sum of the transmittance (t) and reflectance (r) is less than unity. The absorption coefficient, a, results in,

$$r + t + a = 1. \tag{3.15}$$

Combining Equations (3.3) and (3.7),

$$T = \left(1 - \frac{a}{1 - r}\right)^2 \frac{1}{1 + k\sin^2(\phi/2)}. \tag{3.16}$$

Comparing Equation (3.16) with (3.7) we see that the absorption diminishes the intensity of the transmitted light by a factor $[1 - a/(1-r)]^{-2}$. Figure 3.7 shows a plot of T versus ϕ for a = 0, 0.02, 0.05 and 0.08 for r = 0.9. Figure 3.8 depicts the change in the T versus ϕ transfer function curve for various values of r (a = 0.08). An important point to note here is that although the finesse still increases with r, the fringe contrasts drops significantly.

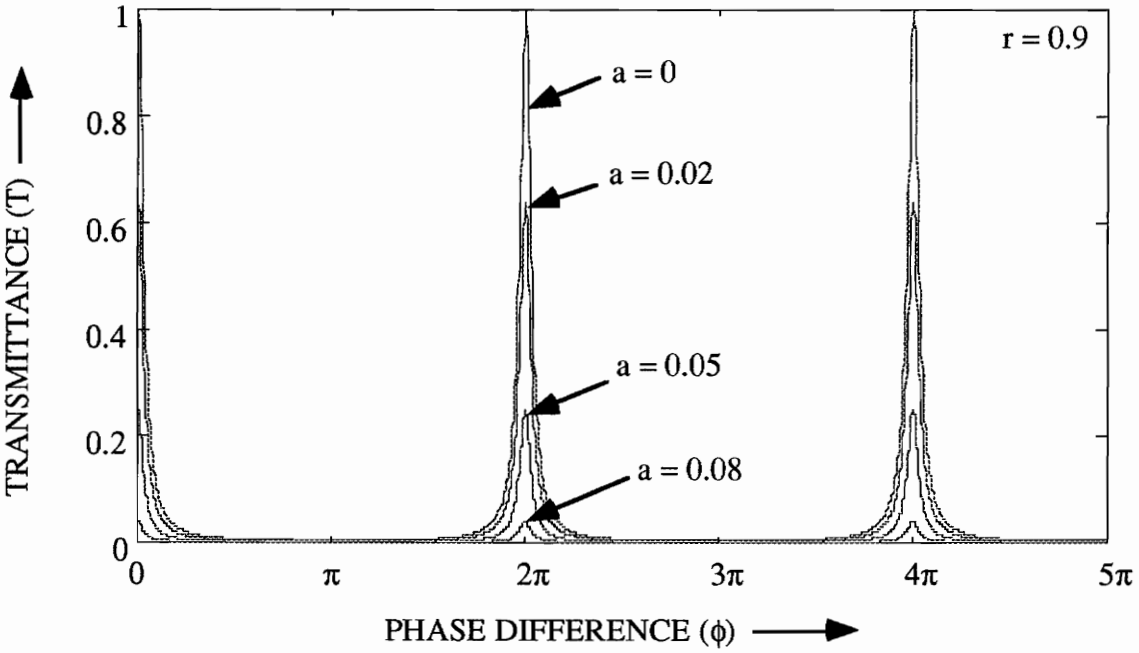

Figure 3.7. Transmittance (T) versus phase difference (ϕ) for constant r (0.9) and varying values of absorption coefficient (a).

2) The phase change between the incident and reflected waves at an interface is no longer π and Equation (2.2) in Chapter 2 is modified to,

$$\phi = \frac{4\pi}{\lambda} d + 2\theta \,, \tag{3.17}$$

where, θ is the phase change on reflection. For normal incidence, the phase change (θ) at the interface results in an error in the measurement of the cavity length by a factor $\theta\lambda/2\pi$ in the classical EFPI. In the absolute EFPI which utilizes two wavelengths, λ_1 and λ_2, the differential phase difference ($\Delta\phi$) given in Equation (2.13) in Chapter 2 is then modified to,

$$\Delta\phi = \frac{4\pi}{\lambda_1} d - \frac{4\pi}{\lambda_2} d + 2(\theta_1 - \theta_2) . \qquad (3.18)$$

Thus, the error resulting from phase change due to reflection at metal films is more pronounced in a conventional fiber EFPI than it is in the absolute EFPI configuration. Although this phase change leads to an error in the gap measurement which is less than half the wavelength of operation, it sets a lower limit on the accuracy of both the systems.

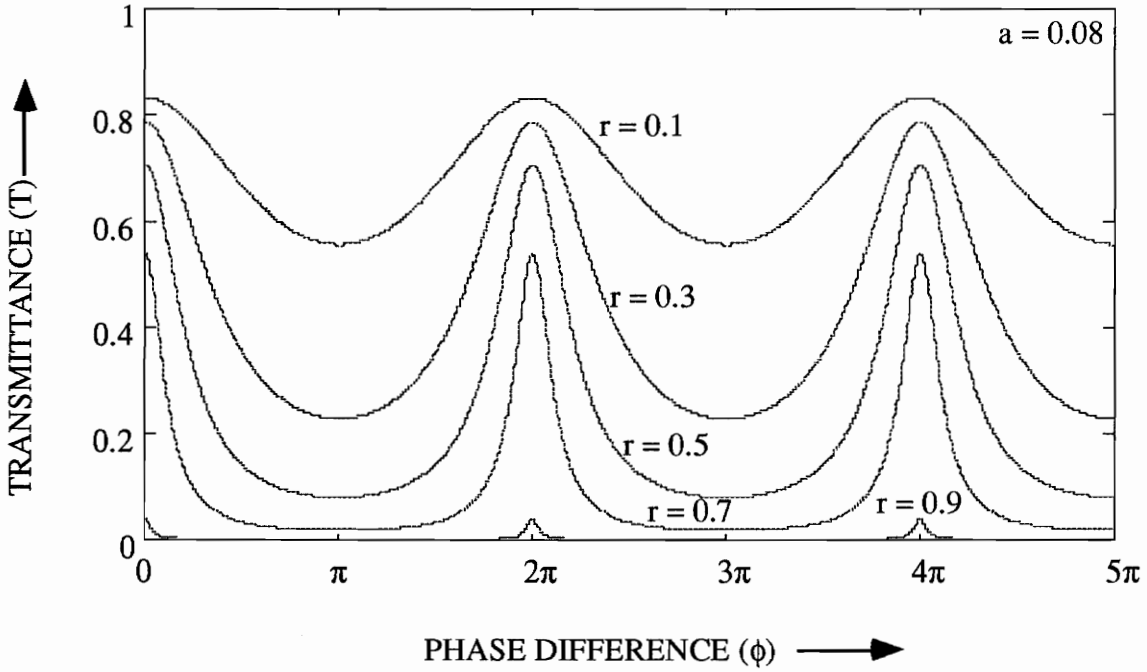

Figure 3.8. Transmittance (T) versus phase difference (ϕ) for constant a (0.08) and varying reflection coefficients (r).

3.3 Important Characteristics of a Fabry-Perot Cavity

Apart from finesse, a Fabry-Perot cavity is characterized using two other parameters - Peak Transmission and Contrast Factor.

Peak Transmission τ is the maximum value of the cavity transmittance, T,

$$\tau = T_{max} . \qquad (3.19)$$

From Equation (3.16) we have,

$$\tau = \left(1 - \frac{a}{1 - r}\right)^2 . \tag{3.20}$$

Figure 3.8 shows the drop in τ as r increases.

Contrast Factor C is defined as the ratio of the maximum and minimum values of T,

$$C = \frac{T_{max}}{T_{min}} . \tag{3.21}$$

From Equations (3.16), (3.13) and (3.6), we have,

$$C = 1 + k = \left(\frac{1 + r}{1 - r}\right)^2 = 1 + \frac{4F^2}{k^2} . \tag{3.22}$$

As is seen from Equations (3.13) and (3.22), the finesse (F) and the contrast factor (C), increase and decrease, respectively, with the mirror reflectance (r). Thus, simultaneous requirements of high F and C are incompatible and an optimum value of r exists for the best possible performance.

Due to an uneven cleave at the fiber end face or non-uniform metal deposition, the two interfaces forming the cavity might not be plane or parallel. Dufour and Picca [13], and Chabbal [14] have shown that such effects lead to a reduction in the cavity finesse and the peak transmission. In fact as reflectivity, r, approaches unity, the finesse of the cavity formed by two non-parallel and/or non-uniform interfaces reaches an upper limit F_d, which depends on the interface defects [12].

3.4 Sensitivity Improvement in High Finesse Cavities

It will be shown in Chapter 4, the EFPI in the white light interferometry configuration performs better in transmittive mode than in reflective mode. Consequently, the improvement in sensitivity resulting from high finesse cavities over a conventional EFPI is considered for the transmissive mode only.

Let us define a quantity ξ as the deviation in the round trip phase shift ϕ from the value at a transmittance peak, where $\xi = 0$ and $\phi = (2n + 1)\pi$ (n is an integer),

$$\xi = \phi - (2n + 1)\pi . \tag{3.23}$$

Near a transmittance peak ($\xi << 1$), we can express $\cos\phi$ as,

$$\cos\phi = \cos[\xi + (2n + 1)\pi] \cong -\left(1 - \frac{\xi^2}{2}\right) . \tag{3.24}$$

The sensor is said to posses maximum sensitivity when it is operated at the value of ξ

where the slope of the T versus ξ curve has the maximum value. So the sensitivity S for a high finesse EFPI operated in tranmittance is defined as,

$$S = \frac{1}{\sqrt{T}}\left(\frac{\partial T}{\partial \xi}\right), \tag{3.25}$$

where, T can be obtained from Equations (3.5a) and (3.24), and is given as,

$$T = \frac{t^2}{(1 - r)^2 + r\xi^2}. \tag{3.26}$$

The sensitivity can then be obtained as follows,

$$S = \frac{2tr\xi}{\left[(1 - r)^2 + r\xi^2\right]^{3/2}}. \tag{3.27}$$

The maximum value of the sensitivity occurs when $\partial^2 T/\partial \xi^2 = 0$, that is,

$$\xi = \frac{1 - r}{\sqrt{3r}}. \tag{3.28}$$

From Equations (3.27) and (3.28), the maximum sensitivity S_{max} is,

$$S_{max} = \frac{3tr\sqrt{r}}{4(1 - r)^2} = \frac{3(1 - r - a)r\sqrt{r}}{4(1 - r)^2}. \tag{3.29}$$

Figure 3.9 depicts the plot of the maximum sensitivity, S_{max}, as a function of the reflectivity, r, (for a = 0.06). For r = 0.9 (90% mirror reflectivity), the sensitivity is 2.561. A similar expression for sensitivity in reflection mode has been derived in [10].

It has been shown elsewhere that for a low finesse cavity, the sensitivity, $S = \sqrt{2r}$. For an air-glass interface in a conventional EFPI, r = 0.04 and hence the sensitivity is only 0.283. Thus, the advantage of using a high finesse cavity (F = 29.8 for r = 0.9) over a simple air-glass interface cavity is that the sensitivity of the system improves by a factor of 9.

3.5 Significance of Type and Thickness of Metal Coatings

As mentioned earlier metal coatings are preferred to dielectric films when a broadband source is used. The reflectivity of the metal coating (at a particular wavelength) and hence the sensitivity of the system, depends not only on the type of metal used, but also on the thickness of the film [15].

Figure 3.10 depicts the change in the reflectivity of an aluminum film with its thickness (h) for three wavelengths of interest namely, 630 nm, 827 nm and 1250 nm. Due to increase in

the refractive index of the film from the enhanced thickness, the Fresnel reflection coefficient, r, in Equation 3.1 becomes larger. This increase in coating thickness effectively enhances the finesse of the FP cavity.

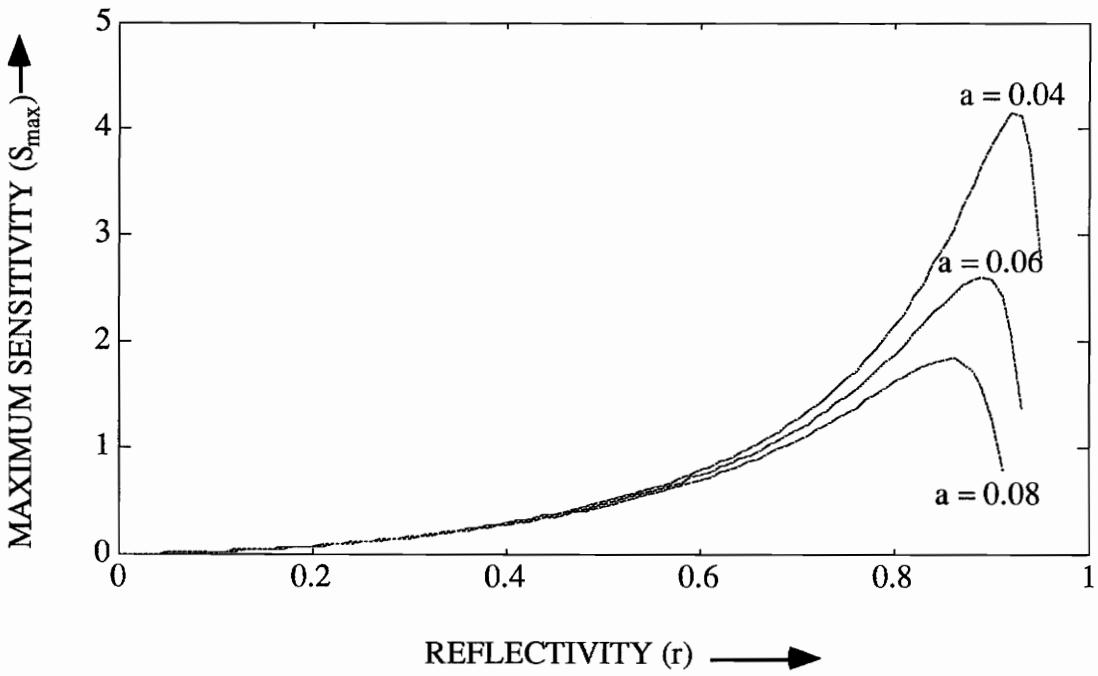

Figure 3.9. Improvement in the maximum sensitivity (S_{max}) of an EFPI with reflectivity (r) for different values of the absorption coefficient (a).

In Figure 3.11, the reflection coefficient (r) for the three common metals employed in the coating process is shown as a function of the thickness (h) at 827 nm. Although aluminum has higher value of reflectivity (r) for smaller values of h, gold and silver possess a larger r for thickness more than 250 Å. Thus for a value of r greater than 0.9, gold and silver are preferred over aluminum.

The three parameters, reflectivity, r, transmissivity, t, and absorption, a, are shown for gold coating (at λ = 827 nm) for thickness h in Figure 3.12. For a value of h greater than 120 Å, the reflectivity becomes more than the transmissivity. An interesting point to note here is that the absorption, a, remains less than 3% for all values of thickness of interest.

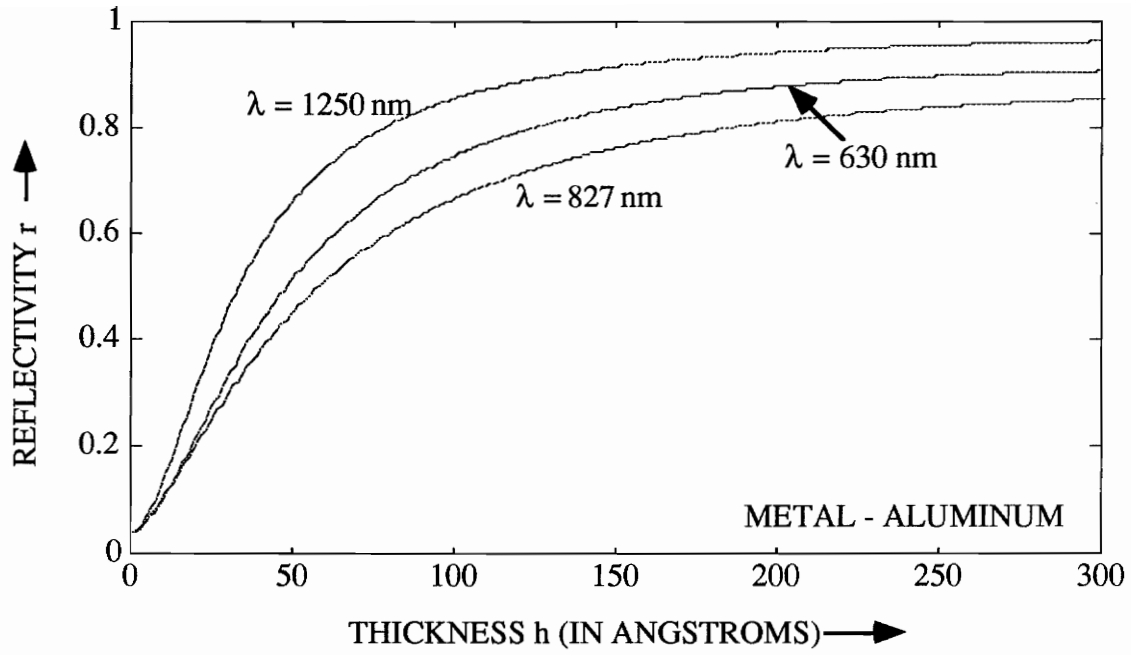

Figure 3.10. Variation in the reflectivity (r) of an aluminum film as a function of its thickness (h).

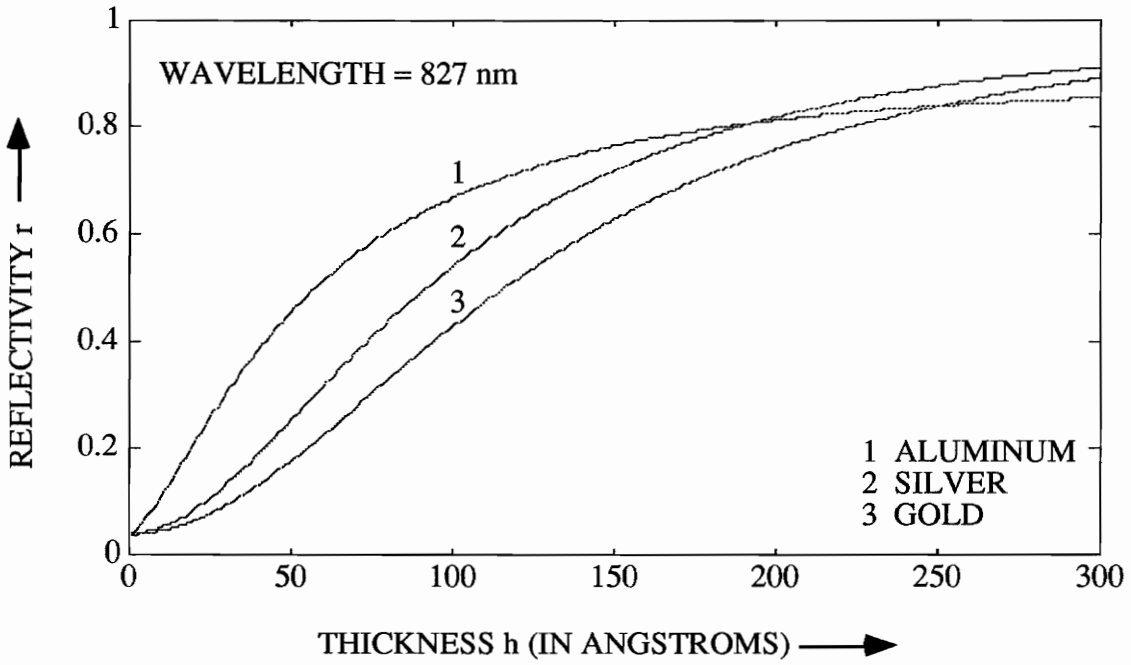

Figure 3.11. Reflectivity versus the film thickness for various metals at 827 nm.

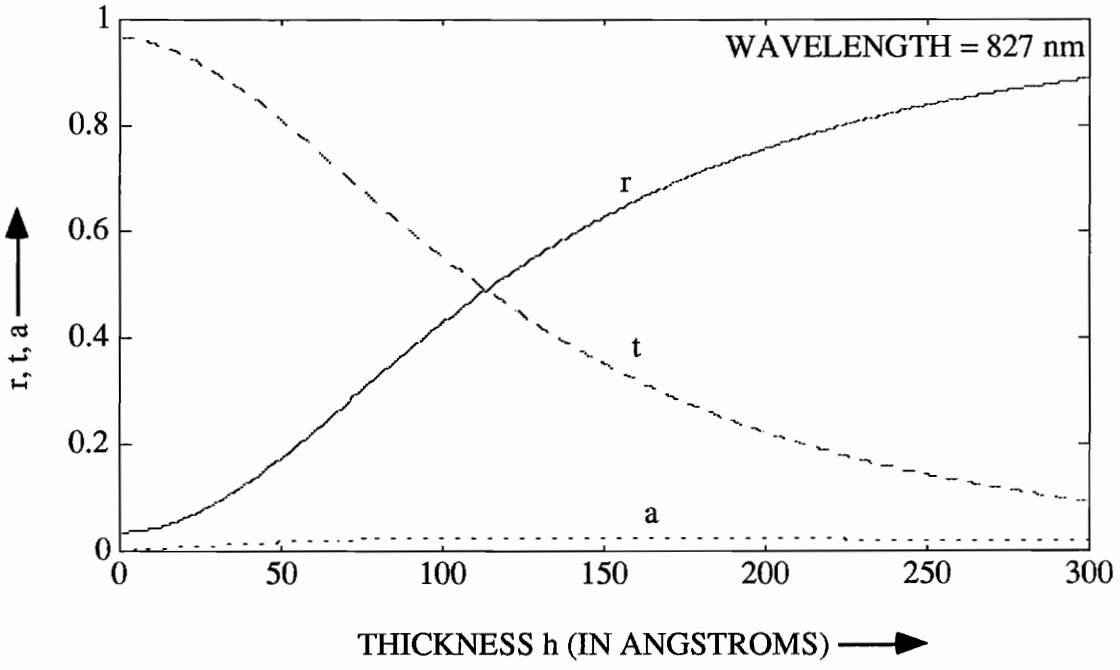

Figure 3.12. Change in reflection (r), transmission (t) and absorption (a) for a gold film at 827 nm.

Figure 3.13 shows the change in the three significant factors of a FP cavity with the thickness, h, again at 827 nm. These are the reflectivity, r, the value of the maximum sensitivity, S_{max} (from Equation 3.29), and the sensitivity increase, I, over a conventional EFPI (S = 0.283 for r = 0.04) operating at its Q-point,

$$I = \frac{S_{max}}{0.283} . \tag{3.30}$$

Thus an EFPI with a 300 Å coating of gold is about 18 times more sensitive in comparison with a conventional EFPI without any coating. High finesse cavities are hence employed in interferometers to obtain enhanced system sensitivity.

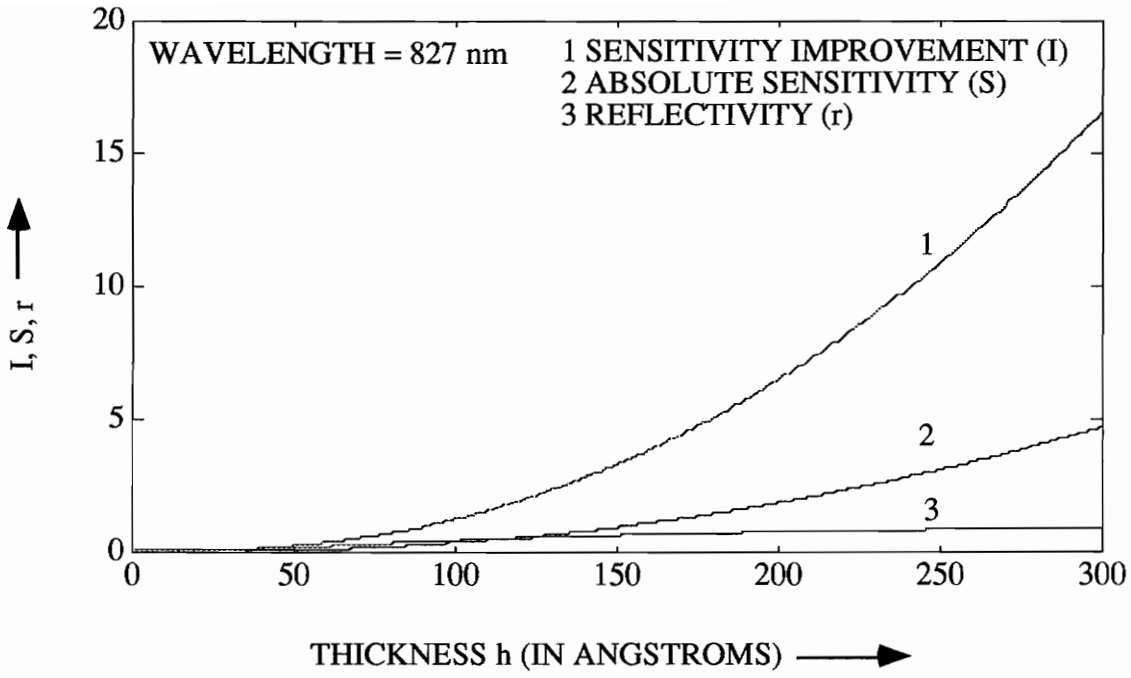

Figure 3.13. Sensitivity improvement (I), absolute sensitivity (S) and interface reflectivity (r) at 827 nm for an EFPI cavity formed between two gold coated fiber end faces.

Chapter 4 - System Setup And Experimental Results

In this chapter we discuss the basic configuration of the Absolute EFPI (AEFPI) sensing system. The principal components of the system are listed and basic laboratory experiments using this configuration are described and the experimental results analyzed. An expression for the strain resolution of the system is obtained in terms of various parameters of the system. Finally techniques to multiplex a number of sensors are analyzed.

4.1 Differences Between Conventional and Absolute EFPI Systems

In Chapter 2 we discussed how absolute, real-time information can be derived from an EFPI if white light interferometry is used. The two basic components of the white light interferometry configuration are a broadband light source and an optical spectrum analyzer at the output. The constant phase method would be used for signal processing since it is easier to implement than the constant wavelength technique. High finesse FP cavities increase the sharpness of the peaks in transmission mode and hence the determination of two wavelengths 2π out of phase is a relatively simpler task.

As was shown in Chapter 3, the increase in reflectivity of the two interfaces increases the peak transmission of the EFPI cavity, hence moving the transmitted signal further away from the noise floor of the system. In the reflected mode the maxima are spread over a range of wavelengths and hence the exact determination of two out of phase wavelengths becomes difficult. Also the well defined minima are near the noise floor, and might not be able to provide useful information about the cavity length. Thus high finesse EFPI cavities are generally employed in the transmission mode. This also eliminates the use of a 2x2 bi-directional coupler and hence prevents a possible 6 dB loss in the signal received by the spectrum analyzer.

Thus the basic differences between a conventional EFPI and the AEFPI systems can be summarized as follows:

1) The AEFPI uses a broadband source while the conventional EFPI employs a narrow band line source.

2) Unlike a conventional EFPI system, the AEFPI system uses high finesse cavities.

3) The demodulation in a conventional EFPI is done using an oscilloscope (time domain fringes) while that in the AEFPI is performed by an optical spectrum analyzer (wavelength domain fringes).

4) The AEFPI performs better in transmission while the conventional EFPI exhibits superior results in reflection mode.

4.2 AEFPI System Configuration

The basic setup of the AEFPI system developed jointly by researchers at FEORC and F&S [16] is shown in Figure 4.1.

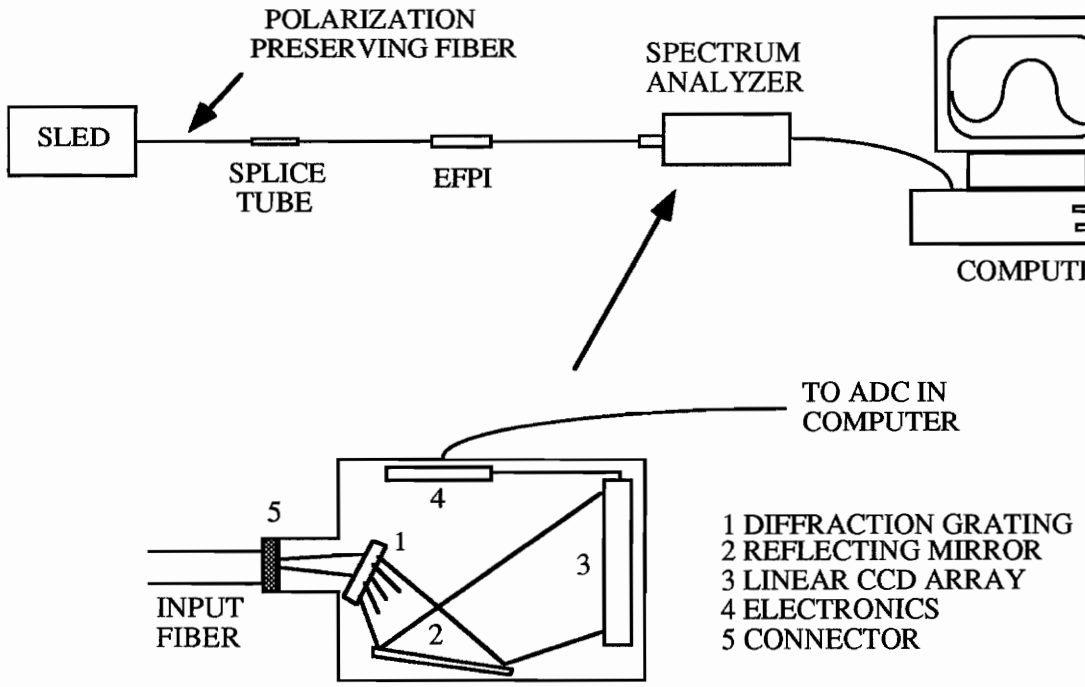

Figure 4.1. Setup of the Absolute EFPI (AEFPI) system.

The broadband source utilized for white light interferometry is a Superluminescent LED or simply, a SLED. A SLED has the same 3 dB bandwidth as a LED but has a much higher power output in comparison with a LED. The SLED used in the system was acquired from EG&G Corporation and is centered at approximately 830 nm. It has an output power (into

a single mode fiber) of 1.4 mW at a drive current of 120 mA. The SLED was pigtailed by OZ Optics in Canada using a polarization preserving, relatively bend insensitive single mode fiber at 830 nm. The output spectrum of this SLED is shown in Figure 4.2.

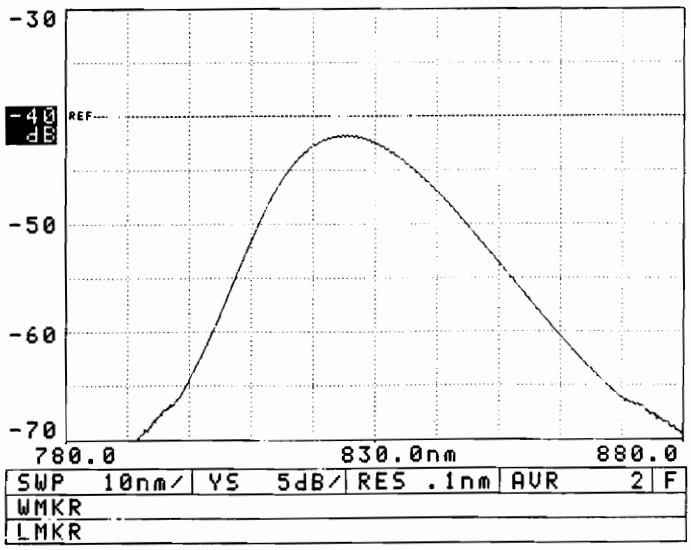

Figure 4.2. Spectrum of the EG&G Corporation SLED employed in the AEFPI system.

The optical spectrum analyzer was obtained from Ocean Optics, Florida. It is reportedly the world's smallest optical spectrum analyzer and has to be interfaced to a computer for data acquisition and processing. It basically consists of a 1800 lines/mm diffraction grating which spreads out the incoming light spatially based on its frequency (or wavelength) content, followed by a linear CCD (Charge Coupled Device) array of a certain number of pixels. The grating in use determines the wavelength range of operation, which in the above case was 780 to 865 nm. The resolution of the AEFPI system depends on the number of pixels in the CCD array and the wavelength range. The CCD array in the Ocean Optics spectrum analyzer has 1024 pixels. Each element on the array is excited by light of corresponding wavelength and this leads to the charging of the CCD element to a certain voltage depending on the intensity of incident light. Thus each element behaves as a capacitor which has a certain charging and discharging time. The charging and discharging of the element has to be completed before a change in the incident intensity occurs,

otherwise the information in the light signal would be lost. The charging and the discharging time add up to what is defined as the Integration Time, T, of the array. Thus the integration time of the spectrum analyzer determines the maximum rate of change (of measurable strain and temperature) or frequency response of the AEFPI system.

The analog signal from the CCD array is then fed to a Analog to Digital Converter (ADC). The speed of the ADC also determines the allowed upper limit of the perturbation frequency. The digital signal from each pixel is then displayed on a personal computer screen. Since each pixel corresponds to a particular wavelength we effectively get a plot of output intensity versus wavelength. This output pattern from the EFPI consists of a series of peaks and troughs.

A computer code was then devised in C++ to determine the pixel locations corresponding to the intensity peaks. The pixel number corresponding to a maxima was determined by finding the point at which transition from a positive intensity versus wavelength slope to a negative slope occurred. The pixel numbers were converted to wavelength values by using a calibration curve obtained from Ocean Optics [17]. The wavelength values corresponding to all the intensity peaks were then stored in vector form. Two consecutive wavelength values λ_m and λ_n ($\lambda_n > \lambda_m$) in the middle of this vector were then used to determine the "unaveraged" gap length d_u,

$$d_u = \frac{\lambda_m \lambda_n}{2(\lambda_n - \lambda_m)} . \tag{4.1}$$

The "averaged" gap length d_a is obtained as follows,

$$d_a = \frac{1}{N-1} \sum_{i=1}^{N-1} \frac{\lambda_i \lambda_{i+1}}{2(\lambda_{i+1} - \lambda_i)} , \tag{4.2}$$

where, λ_i (i = 1 to N) is the vector of wavelengths corresponding to intensity peaks. The averaged gap length is used in applications where a high degree of accuracy is required or where a large noise floor is present.

For strain calculations, the computer code requests for the gage length, L (defined in Section 2.1), of the sensor in use. The strain ε is then given by,

$$\varepsilon = \frac{d_a^1 - d_a^0}{L} , \tag{4.3}$$

where, d_a^1 and d_a^0 are respectively, the averaged gap lengths after and before stress is

applied.

For temperature sensing, the calibration curve for temperature versus gap length has to be determined first. This calibration curve is then stored in the computer and for a given gap the corresponding temperature is displayed.

A fiber was chosen such that it operates in the single mode domain for the entire SLED spectrum. This fiber was obtained from Ensign-Bickford. Although fiber at 830 nm is more expensive than that at 1300 nm, the unavailability of the required source (SLED) and spectrum analyzer at 1300 nm, compelled us to use a 830 nm system.

The high finesse EFPI cavity was obtained by using two 830 nm fibers coated with a metallic film on one of the end faces. The coating process was carried out using an evaporation chamber. The end of each cleaved fiber was checked to ensure it was flat and perpendicular to the fiber axis. The fibers were taped (using a high temperature tape) carefully on a aluminum block which was then fixed to a circular aluminum plate, with the fiber ends protruding out. This plate was then placed inside the evaporation chamber and the fiber ends were coated first with a thin film (30 Å) of chromium. A chromium coating was used because the metal coatings adhere better if there is a film of chromium below. High purity gold was then used to obtain gold coating of the required thickness. The thickness was controlled using the thickness monitor of the evaporation chamber. To protect this layer of gold from scratching a film of silica 100 Å was deposited on it.

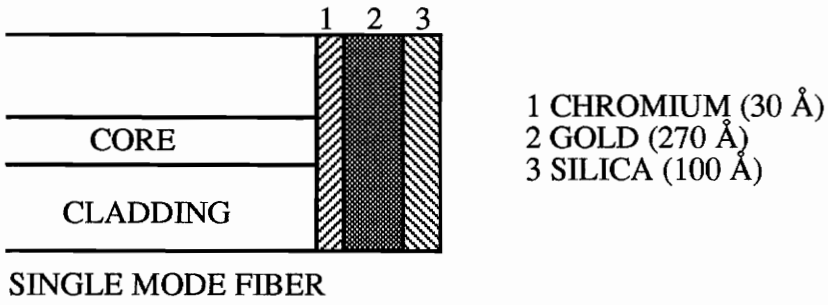

Figure 4.3. A typical single mode fiber endface used for high finesse EFPI fabrication (not drawn to scale).

The endface of a typical coated fiber is shown in Figure 4.3. Although silica has no appreciable effect on the reflectivity of the interface, chromium increases the absorption

coefficient and hence reduces the peak transmission of the cavity.

The scanning rate of the CCD array in the spectrum analyzer can be varied to suit a particular application. Also the grating can be displaced manually by using a set screw on the outside. This can be utilized to move the dispersed light spatially to obtain the correct pixel number corresponding to a particular wavelength.

4.3 Strain Resolution of the AEFPI System

The resolution of the AEFPI system depends on four main factors:

1) The diameter of the input fiber determines the spread of the pattern incident on the diffraction grating. The output from the grating depends on the spread angle at the input and thus each wavelength component may excite a certain number of pixels on the CCD array. To obtain a less spread out pattern, the fiber should have a smaller core size.

2) The Numerical Aperture or NA of the fiber also affects the spread at the input to the grating. So for a better resolution the NA of the input fiber should be small.

3) The number of diffraction lines on the grating also influences the resolution of the AEFPI system. The higher is the number of diffraction lines, the better is the resolving power of the system, since the wavelength range for a given number of pixels reduces.

4) The most important factor affecting the resolution of the system is the number of pixels on the CCD array for a fixed wavelength range. As is obvious, increasing the number of pixels can improve the overall resolution.

Of these four factors, the first two are constant for a given input fiber. In fact the product of the fiber diameter and NA has to be constant for single mode operation at a particular wavelength. So the improvement in resolution due to decrease in any one of these parameters is offset by the corresponding degradation resulting from the other one. A CCD array having more than 1024 pixels becomes expensive to implement and also increases the scanning time of the array. Thus the only factor that can be changed to obtain an enhanced system resolution is the period (in lines/mm) of the diffraction grating. Initially the Ocean Optics spectrum analyzer in use had 1200 lines/mm grating and a wavelength range from 700 to 950 (bandwidth 250 nm). This wavelength bandwidth reduced to 85 nm (780 to 865 nm) when the original grating was replaced with one having 1800 lines/mm. This increased the number of pixels per unit wavelength, resulting in a better wavelength resolution (0.2 nm) of the spectrometer.

Let us now examine how the strain resolution of the AEFPI system depends on the factors such as the bandwidth of the diffraction grating (Ω) and the number of pixels (N) in the CCD array. The wavelength resolution $\Delta\lambda$ of the CDD array can be written as,

$$\Delta\lambda = \frac{\Omega}{N} . \tag{4.4}$$

The strain ε detected by the sensor is given by,

$$\varepsilon = \frac{\Delta L}{L} , \tag{4.5}$$

where, ΔL is the change in the cavity length and L is the gage length of the sensor. The change in detected strain, $\Delta\varepsilon$, is then given by,

$$\Delta\varepsilon = \frac{\Delta d}{L} , \tag{4.6}$$

where, Δd is the change in ΔL.

The strain resolution f is then defined as,

$$f = \Delta\varepsilon_{min} , \tag{4.7}$$

where, $\Delta\varepsilon_{min}$ is the minimum detectable value of strain change $\Delta\varepsilon$.

For wavelength resolution $\Delta\lambda$, the corresponding minimum detectable gap change Δd can be found from,

$$d + \Delta d = \frac{(\lambda_1 + \Delta\lambda)(\lambda_2 + \Delta\lambda)}{2(\lambda_1 - \lambda_2)} , \tag{4.8}$$

where, λ_1 and λ_2 ($\lambda_1 > \lambda_2$) are two wavelength corresponding to intensity peaks. For $\Delta\lambda << 1$, this can be simplified to,

$$\Delta d = \frac{\Delta\lambda(4d + \lambda_1)}{2\lambda_1} . \tag{4.9}$$

At optical wavelengths $\lambda_1 << d$ and if we assume that one peak always occurs at the center wavelength λ_0, Equation (4.9) can be written as,

$$\Delta d = \frac{2d}{\lambda_0}\Delta\lambda . \tag{4.10}$$

For the system fabricated, the minimum detectable gap change Δd (for d = 50 μm) from the above expression is found to be 5.7 nm. In actual applications, the presence of noise increases this value to 1 μm.

From Equations (4.4), (4.6), (4.7) and (4.10), we obtain the strain resolution f,

$$f = \frac{2d\Omega}{\lambda_0 NL}. \tag{4.11}$$

Thus the improvement in resolution can be obtained by using a source with a higher center wavelength, a CCD array with more pixels, a sensor with a larger gage length and a smaller cavity length or a diffraction grating with more number of lines per unit length. An important point to remember here is that as the line spacing in the grating approaches the wavelength of input light, the diffraction pattern becomes skewed and might result in erroneous conclusions about strain measurements [12]. Thus there exists an optimum value of the number of lines per unit length of the grating at which the system resolution is the best.

From Equation (4.11), the strain resolution for the system in use is 0.57 micro-strain (με). Again due to the presence of noise, the minimum detectable strain has a value 100 με.

4.4 Experimental Analysis of the AEFPI System

The AEFPI system was used to perform extensive strain and temperature measurement tests.

A high finesse EFPI with one end free to move inside the hollow core, was fabricated. The input and output fibers were secured to two longitudinally separated translation stages. The free end of the EFPI was pulled out and the output was monitored on the computer screen. Figure 4.4 shows the plot of the measured gap d_m versus the actual gap d_a for the EFPI under test. Although a slight variation from linearity is observed, it can be ignored as it could have resulted from error in reading the translation stage instead of being an inherent part of the AEFPI system. The dynamic range of the system for an EFPI was found to be from 0 to 500 μm. The minimum detectable gap was 1 μm.

The temperature testing of the system involved mounting the EFPI on a thin stainless steel rectangular base and fixing the sensor on this base using a high temperature adhesive. The metal base was then placed on a hot plate and the temperature of the plate was recorded using a thermocouple while it was being heated.

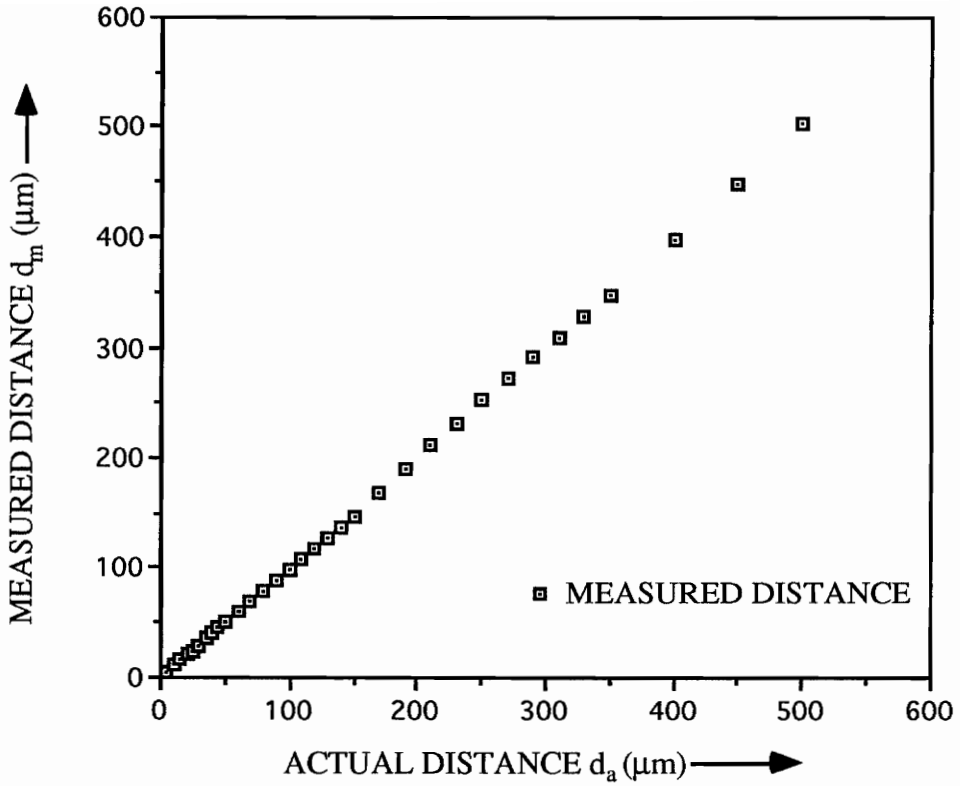

Figure 4.4. Measured gap (from the AEFPI system) versus the actual gap using a high finesse EFPI.

Figure 4.5 shows the plot of the change in the cavity length d with temperature T. The cavity length changed by 62 μm for 125 °C change in temperature. Thus the temperature resolution of the system is almost 2 °C. The gap length change with temperature was found to be repeatable for all sets of observations. The temperature measurement range is limited to 200 °C owing to the use of fiber with acrylic coating. Employing polyimide coated fiber can increase this range to 400 °C. Aluminum and gold coated fibers can be used for temperatures as high as 600 °C and 800 °C, respectively.

Figure 4.6 (a) and (b) show the transmitted outputs obtained on the computer from an EFPI with gap lengths 50 μm and 100 μm, respectively. The high finesse Airy function output is clearly visible.

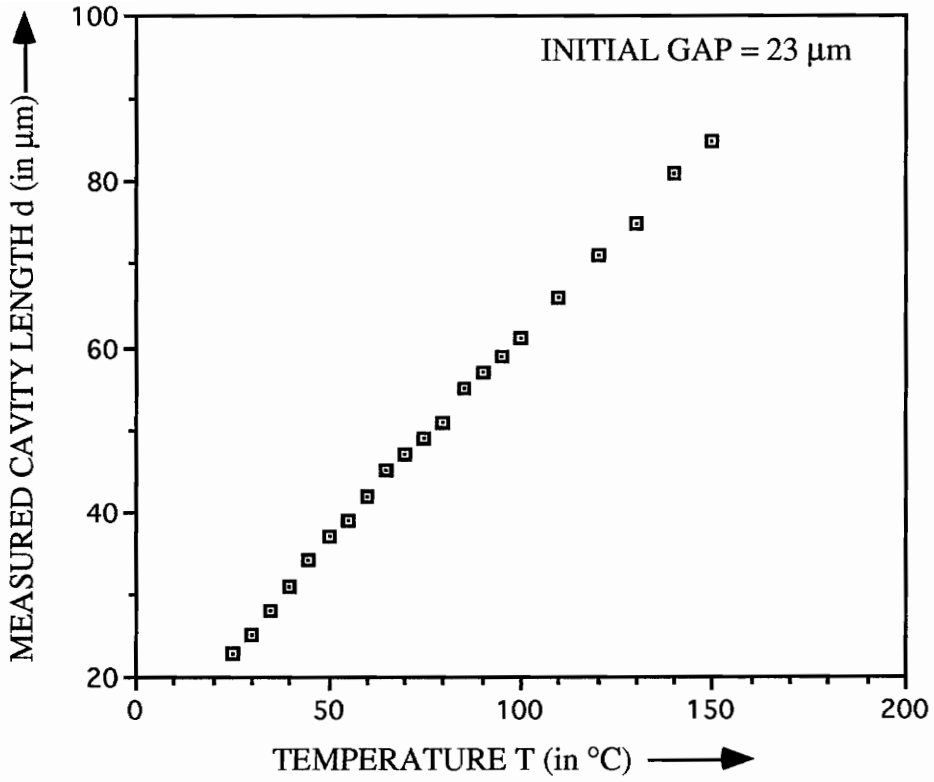

Figure 4.5. Change in gap (d) with temperature (T) for an EFPI mounted on a stainless steel bar.

The miniaturized Temperature Insensitive Michelson Interferometric (TIMI) sensor proposed by Murphy *et al.* [18] was next tested for its compatibility with the Absolute sensing system. It was mounted on a translation stage such that its axis was perpendicular to a 100% front reflecting mirror. The parameter of interest here is the distance between the TIMI head and the mirror. The translation stage was moved parallel to the axis of the TIMI and the averaged distance was monitored on the computer screen. Figure 4.7 depicts the variation of the measured gap as the TIMI is pulled away from the mirror. The minimum detectable gap was again 1 μm but the dynamic range increased to almost 2 mm. The curve in Figure 4.7 was found to be almost invariant for many sets of observations.

One of the reasons for the superior performance of the TIMI in comparison to the high finesse EFPI might be that both the sensing and reference reflections take place off almost

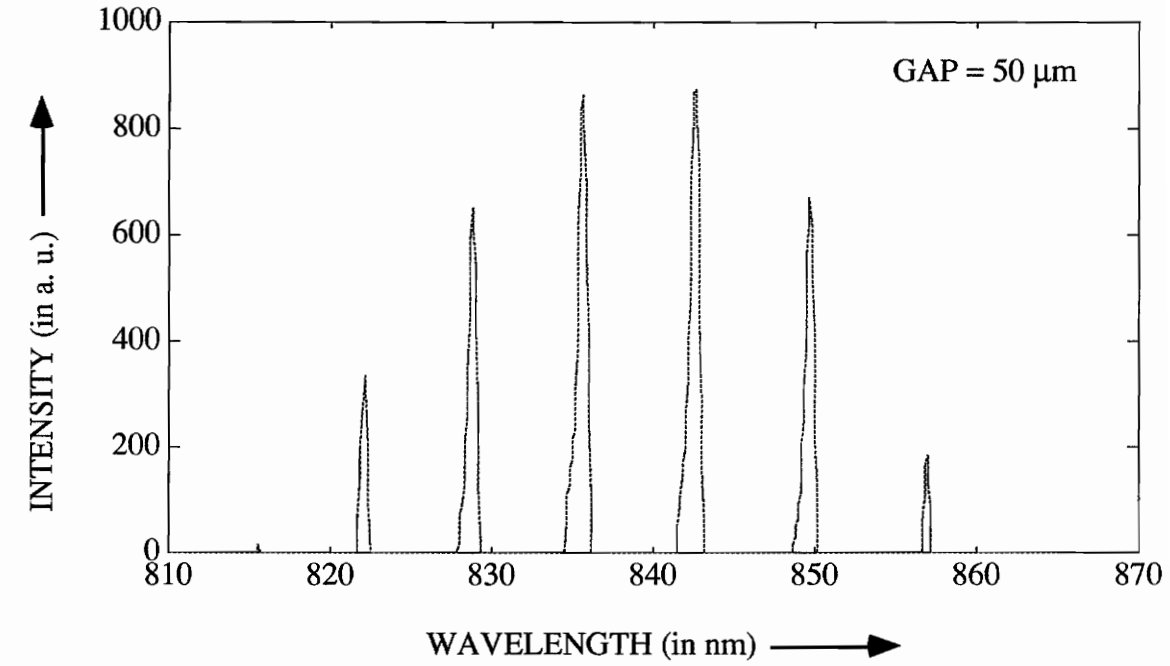

(a)

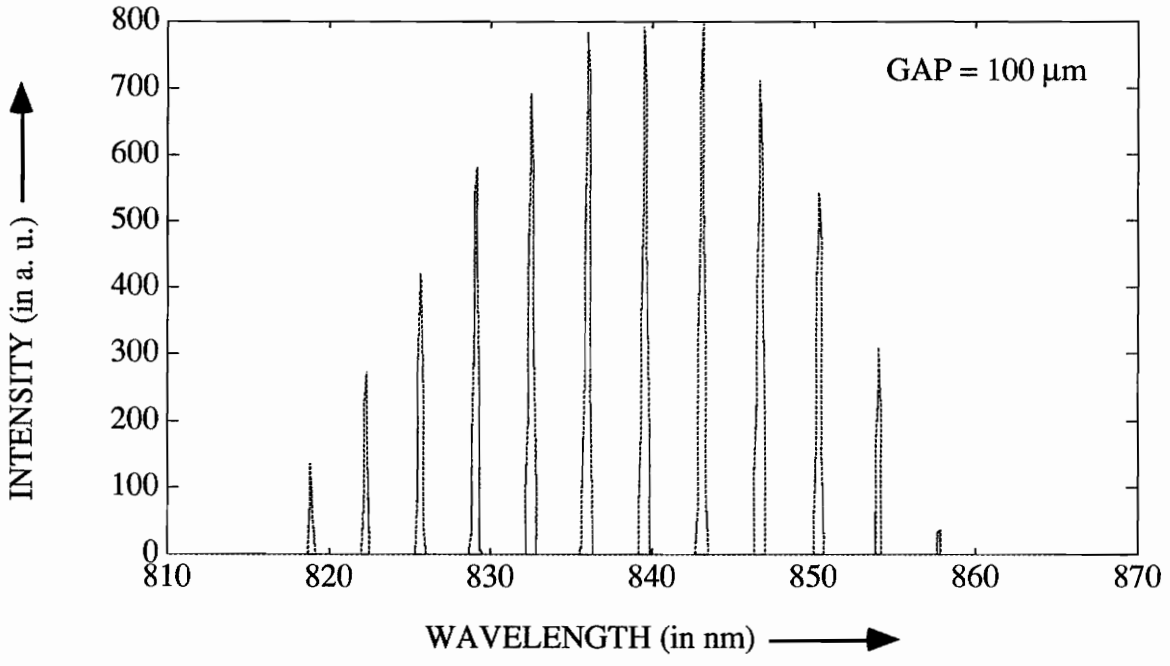

(b)

Figure 4.6. Output from the AEFPI system for different cavity lengths, (a) 50 μm and (b) 100 μm.

100% reflecting mirrors in a TIMI while the typical reflection coefficient r is only 0.85 to 0.9 in a high finesse EFPI. As was seen in the previous chapter, the finesse actually starts peaking only after the reflectivity exceeds 95%. Also in a TIMI, the sensing signal is reflected off a large surface area and hence, once maximum fringe contrast has been obtained, misalignment is not much of a problem. So the dynamic range of a TIMI is much higher than that of a high finesse EFPI and hence the TIMI can be employed in applications where large strain values are expected.

The maximum displacement rate at which the system performance is satisfactory is only about 2 μm/s. Any strain or temperature change which modulates the cavity length faster than 5 Hz cannot be detected by the AEFPI system. Thus this system is suitable for only static and quasi-static measurements and for sensing the initial and final values of quickly changing parameters.

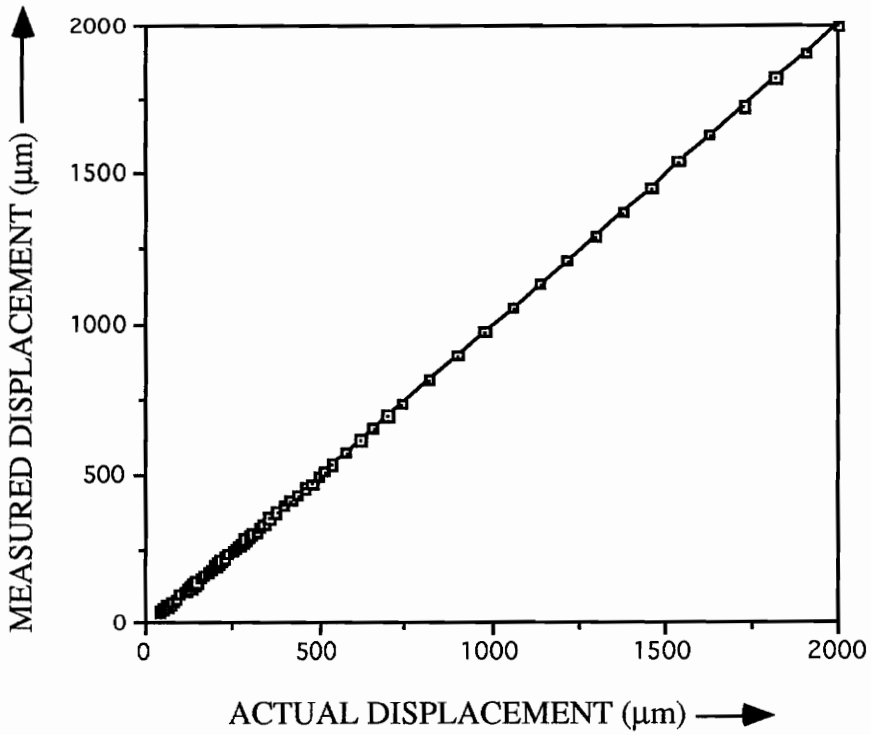

Figure 4.7. Measured gap versus the actual gap for a TIMI.

4.5 Multiplexing of Sensors in the AEFPI Configuration

Multiplexing of fiber sensors is a common method for multi-parameter point sensing and single-parameter distributed sensing. Multiplexing of EFPIs in the absolute sensing arrangement can basically be carried out in two ways 1) common source method, and 2) common spectrum analyzer method.

4.5.1 Common Source Method

As the name suggests, in the common source technique the sensors are multiplexed by using a single SLED. The light from the SLED is divided into N equal parts using a NxN coupler. Each of the N high finesse sensors is spliced to one of the output arms of this coupler. The transmitted pattern for each sensor is obtained by using a separate spectrum analyzer dedicated to a particular sensor. The output from each spectrum analyzer is fed to a single computer for signal processing. The use of a NxN coupler reduces the fringe contrast in every sensor by 10logN dB. The setup for the common source method is depicted in Figure 4.8.

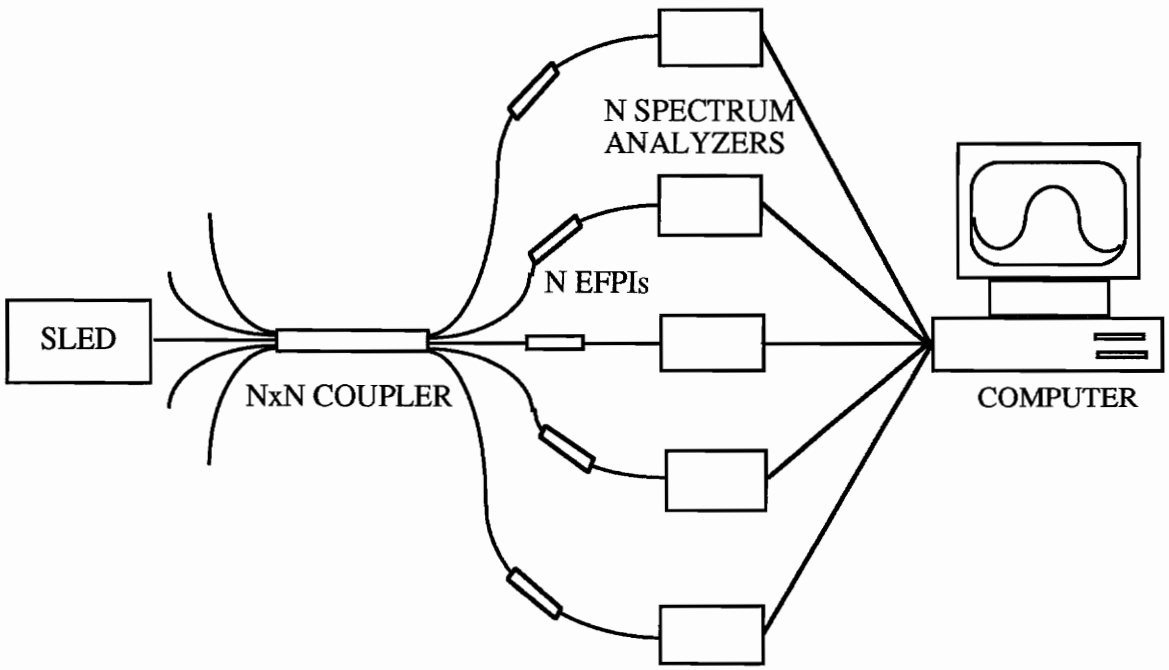

Figure 4.8. Common source method for multiplexing sensors.

4.5.2 Common Spectrum Analyzer Method

The common spectrum analyzer method is similar to the common source method in that N sensors can again be multiplexed to a single system. There are N SLEDs covering different regions of the optical spectrum and the output fiber from each source is spliced to an input arm of a NxN coupler. One of the output arms of this coupler is fed into an optical spectrum analyzer. Signal processing is again done using an ADC followed by a computer. Figure 4.9 shows the arrangement for the common spectrum analyzer multiplexing technique.

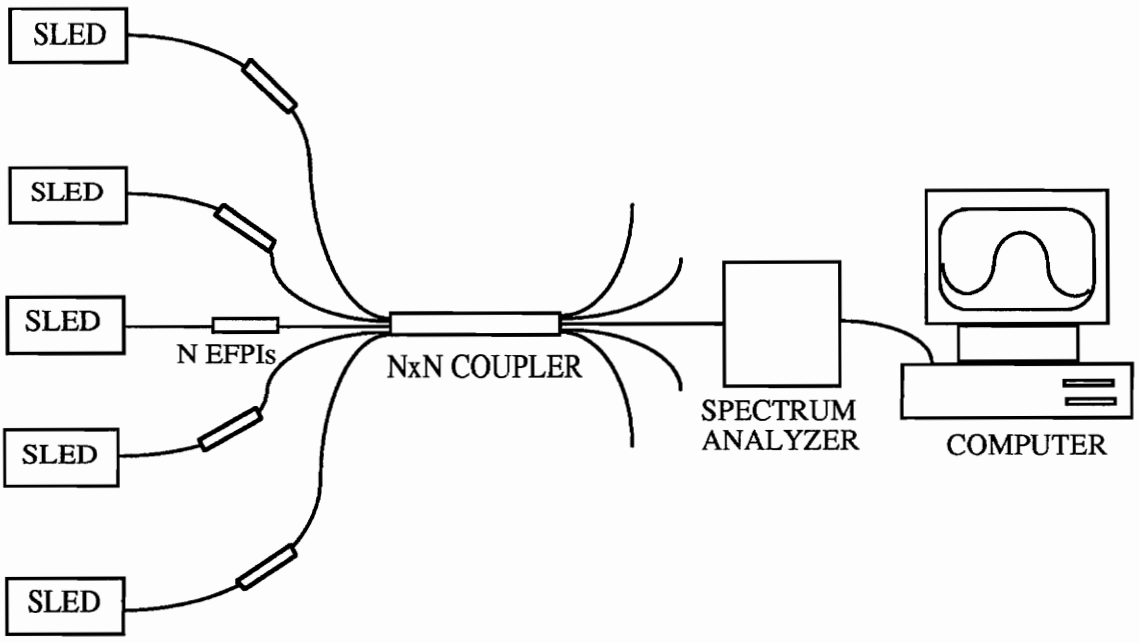

Figure 4.9. Common spectrum analyzer method for multiplexing sensors.

Of the two multiplexing techniques discussed above, the common source method is preferable because it does not compromise the system resolution. In the common spectrum analyzer technique, a grating with a smaller number of lines/mm has to employed to obtain a wider wavelength range. If the number of pixels is assumed to remain the same, the wavelength resolution and hence the strain resolution decreases.

Chapter 5 - Other Variations Of White Light Interferometry

In this chapter we discuss some other popular forms of white light interferometry. Experimental results using these techniques are presented and analyzed. Finally these schemes are compared with the method employed in Chapter 4 and the relative merits and demerits are listed.

5.1 Wavelength Tuning

In Chapter 4 a broadband source was used to extract information from an EFPI. For fixed cavity lengths a technique called wavelength tuning can also be used for sensing various perturbations.

In this scheme, for a gap length, d, the wavelength of a narrow line source, like a LD (laser diode), is varied between two fixed values, say λ_1 and λ_2, and the phase variation $\Delta\phi$ is monitored on an oscilloscope screen,

$$\Delta\phi = \frac{4\pi}{\lambda_1} d - \frac{4\pi}{\lambda_2} d \,, \tag{5.1}$$

or,

$$d = \frac{\lambda_1 \lambda_2}{4\pi(\lambda_2 - \lambda_1)} \Delta\phi \,. \tag{5.2}$$

The wavelength of the LD is generally varied by changing the bias current. This also causes the output intensity to fluctuate and the process of measuring the phase difference $\Delta\phi$ might become difficult, specially at low values of current.

McClintok *et al.* [19] have discussed a technique to use wavelength tuning for strain measurements. The input current is changed by varying the thermo-electric cooler's resistance and the output power is normalized by using a detector at the end of the unused arm of the coupler (Figure 5.1).

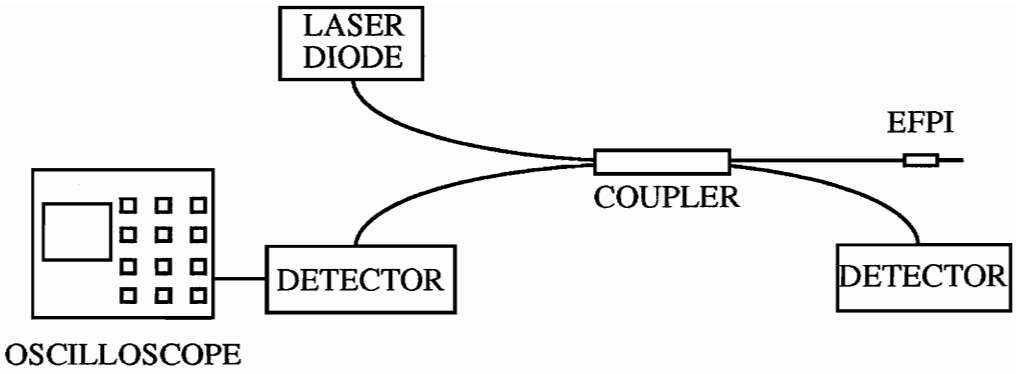

Figure 5.1. Setup for white light interferometry based on the wavelength tuning technique.

5.2 Wavelength Shifting

When the cavity length in an EFPI is small, the peaks are well spaced in the wavelength domain. A small variation in this gap can cause these peak to shift. So instead of using a grating/CCD array combination at the output, the signal processing can be performed by using a bandpass filter (centered at the peak) followed by a photodetector.

Figure 5.2 depicts the output in the wavelength domain for gaps 3 μm and 3.1 μm. As is obvious the peaks shift by a certain amount for a 0.1 μm change in gap. If the initial gap is always fixed, we select an optical bandpass filter centered at one of the wavelength peaks. Any change in the gap length will make this peak shift to a new value and decrease the output intensity of the filter. If this intensity, I, is monitored using a photodetector, absolute gap measurements are possible provided the calibration curve of the output intensity, I, versus the cavity length, d, is known.

The output might be affected by source intensity fluctuations or bends in the fiber and again a detector has to be used in the unused arm of the coupler to compensate for these effects. Figure 5.3 shows the setup for this scheme.

Proof of concept experiments were performed [20] using the arrangement shown in Figure 5.4. The EFPI was embedded in a reinforced concrete specimen and the output was monitored on the OSA while the specimen was being loaded.

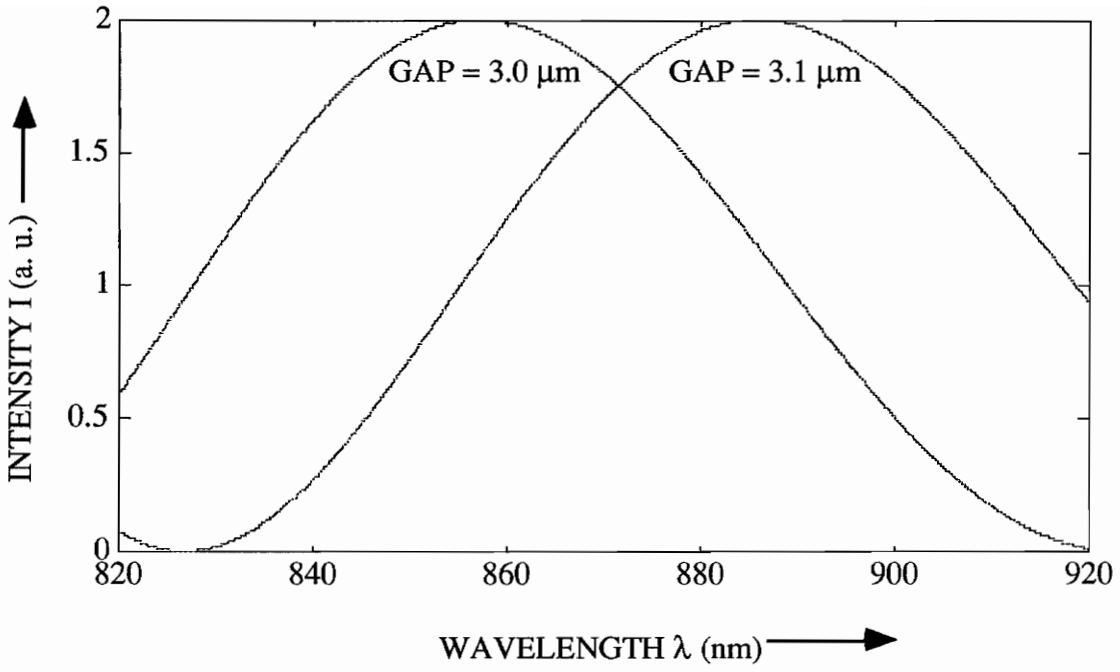

Figure 5.2. Shift in intensity peak due to change in cavity length from 3 μm to 3.1 μm.

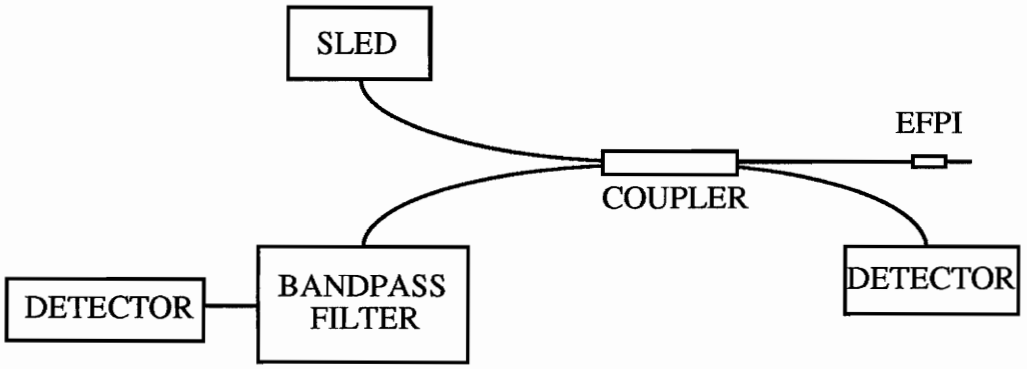

Figure 5.3. Setup for white light interferometry based on wavelength shifting technique.

Figure 5.5 (a) and (b) show the output as the load is increased and decreased, respectively. The shift in the peaks is clearly visible and this shift was recorded to calculate strain as the load increased and then fell back to zero. Shifts in three peaks were monitored to verify the consistency of the scheme.

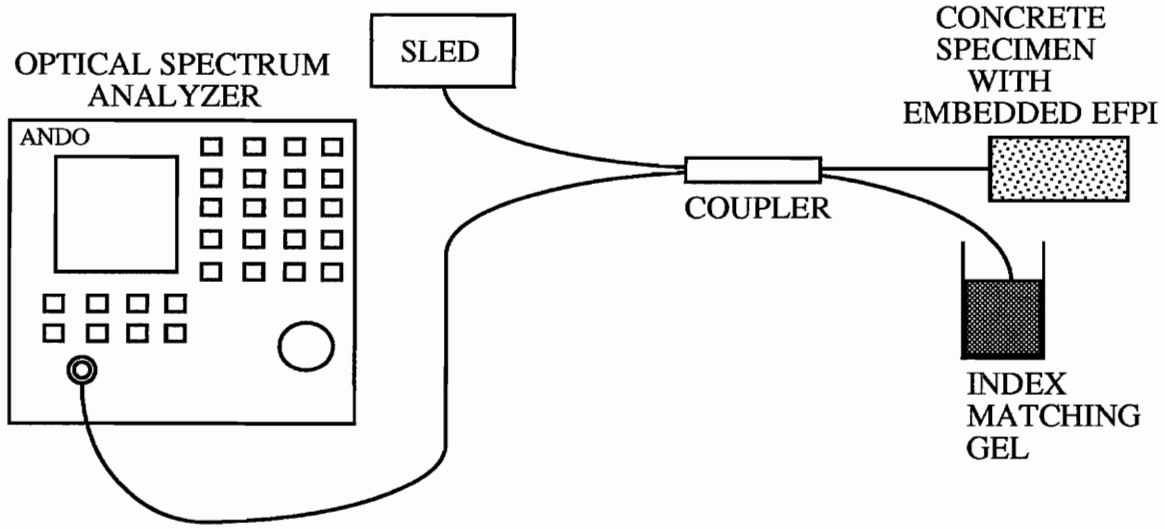

Figure 5.4. Experimental setup to measure strain in a concrete specimen during loading and unloading.

Figure 5.6 shows the plots for the measured strain versus the applied load for three different peaks. The plots are similar and hysteresis is observed in each one of these. To obtain the calibration curve the cavity lengths at no load and at 1000 lbs. load were determined using the constant phase technique described in Chapter 4.

5.3 Path Matching

Path matching is one of the most popular forms of white light interferometry. Two interferometers are usually required to extract information from the system, namely, the sensing interferometer, and the demodulation interferometer.

The coherence length of a typical source in white light interferometry is very small and generally less than the optical path length difference between the interfering beams. So the two beams propagate to the demodulation interferometer with the phase information intact. If the cavity lengths of the two interferometers are exactly matched, the phase difference at the sensing interferometer is compensated for and interference occurs. Fringes can then be

obtained on an oscilloscope, overcoming the signal processing required with the use of a grating/CCD array combination.

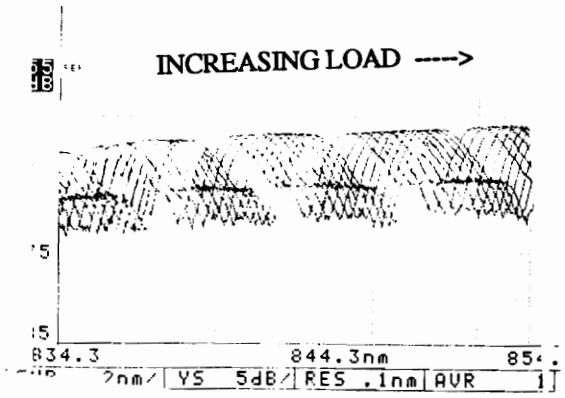

(a)

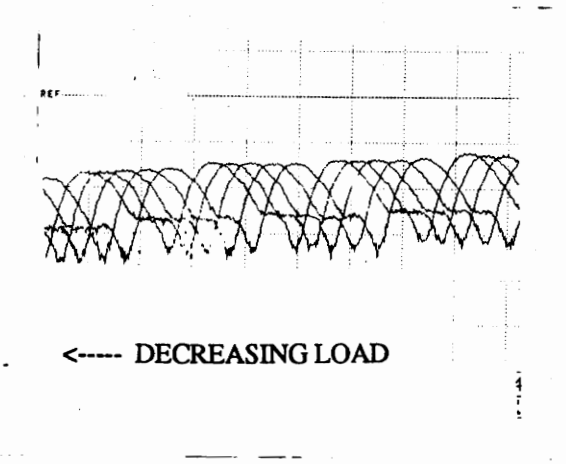

(b)

Figure 5.5. Output on the ANDO Optical Spectrum Analyzer screen as the load on the concrete specimen is (a) increased and (b) decreased.

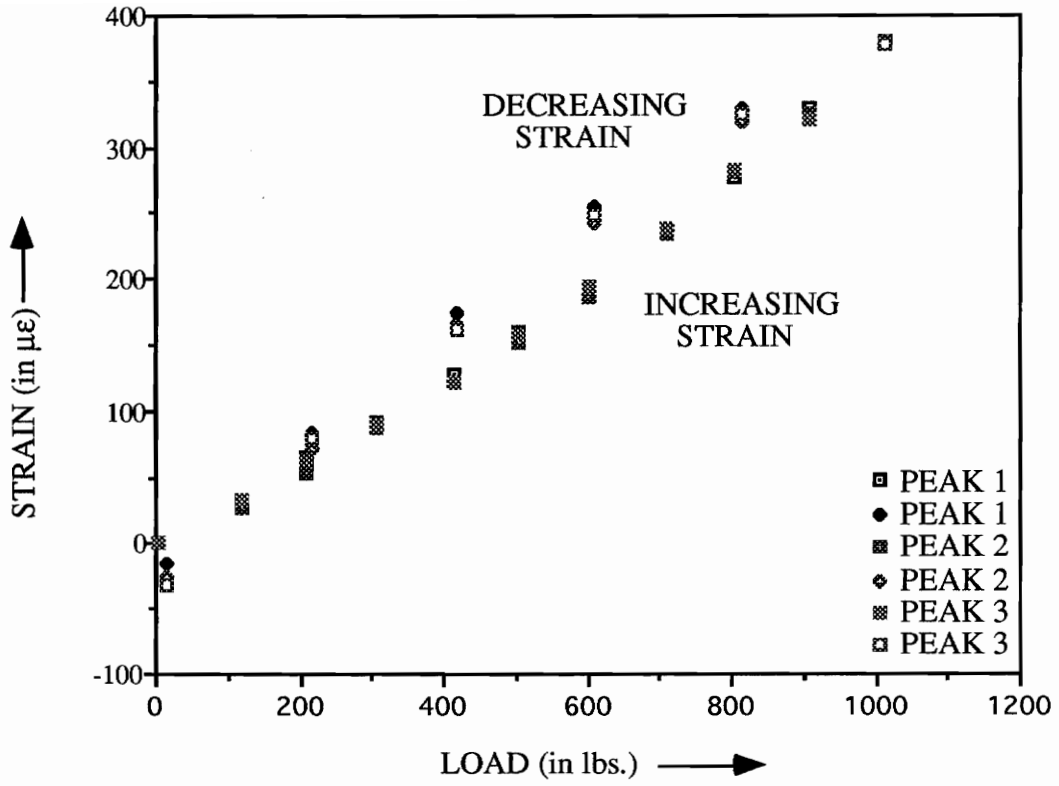

Figure 5.6. Strain measured by monitoring shifts of three peaks in the optical spectrum.

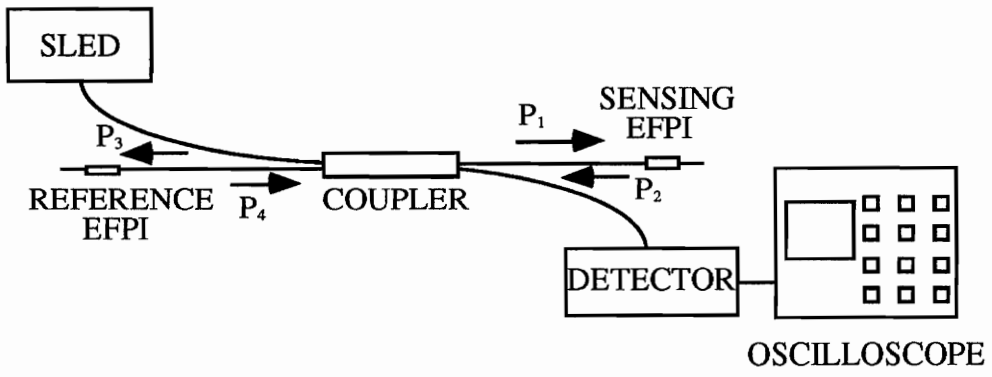

Figure 5.7. Experimental setup for white light interferometry based on path matching technique.

Lee and Taylor [5] have done extensive theoretical and experimental analysis of path matched Fabry-Perot cavities. As can be seen in Figure 5.7, both the sensing and the demodulation EFPIs are used in reflection mode. Both the EFPIs have low finesse cavities. Let P_1 be the power incident on the sensing EFPI and P_2 be that reflected back. After losses in the coupler and fibers (such that $P_3 = \alpha P_2$), let P_3 be the power incident on the demodulation (or reference) EFPI and P_4 be the power reflected back from this EFPI. If $\Delta\phi$ is the phase shift in the sensing EFPI resulting from an external perturbation, P_4 can be expressed as [5],

$$P_4 = 4\alpha r^2 P_1(1 + 0.5\cos(\Delta\phi)), \tag{5.3}$$

where, r is the reflectivity of the four interfaces in the two mirrors.

The power reflected from the reference EFPI undergoes a sinusoidal variation with respect to the perturbation phase shift ($\Delta\phi$). Figure 5.8 (a) shows the power spectral density (PSD) S_1 of the reference EFPI, which is the same as the sensing EFPI when the interferometers are matched ($\Delta\phi = 0$). Figure 5.8 (b) is the square of the output in Figure 5.8 (a) and depicts the reflected spectrum from the path matched EFPIs. The output PSD S_2 of the sensing EFPI for $\Delta\phi = \pi$ is plotted in Figure 5.8 (c). The peaks are out of phase from those in Figure 5.8 (a) by π radians. Figure 5.8 (d) is the product of spectra in Figure 5.8 (a) and (d). The fringe contrast in Figure 5.8 (d) is much less than that in Figure 5.8 (b) because the sensing and the reference interferometers are not path matched in the former. The fringe visibility V is defined as,

$$V = \frac{P_{4max} - P_{4min}}{P_{4max} + P_{4min}}, \tag{5.4}$$

where, P_{4max} and P_{4min} are respectively the maximum and minimum values of P_4. For the system with path matched EFPIs, the maximum visibility is 0.5. For a path length difference ΔL between the sensing and the reference EFPIs, the visibility is [5],

$$V = 0.5\, e^{-(C\Delta L)^2}, \tag{5.5}$$

where, C is a constant directly proportional to the source spectral width.

A similar analysis can be done for high finesse cavities except for the fact that the output would have a more complex dependence on $\Delta\phi$ than the sinusoidal variation in low finesse cavities.

Lee and Taylor have used two path matched EFPIs for temperature sensing. As the sensing EFPI undergoes a temperature change its path imbalance with the reference EFPI increases and the visibility reduces. A typical output is shown in Figure 5.9. The maximum fringe visibility is obtained when no temperature change is present. The fringe visibility drops exponentially with increasing or decreasing temperature, assuming the cavity length changes linearly with temperature.

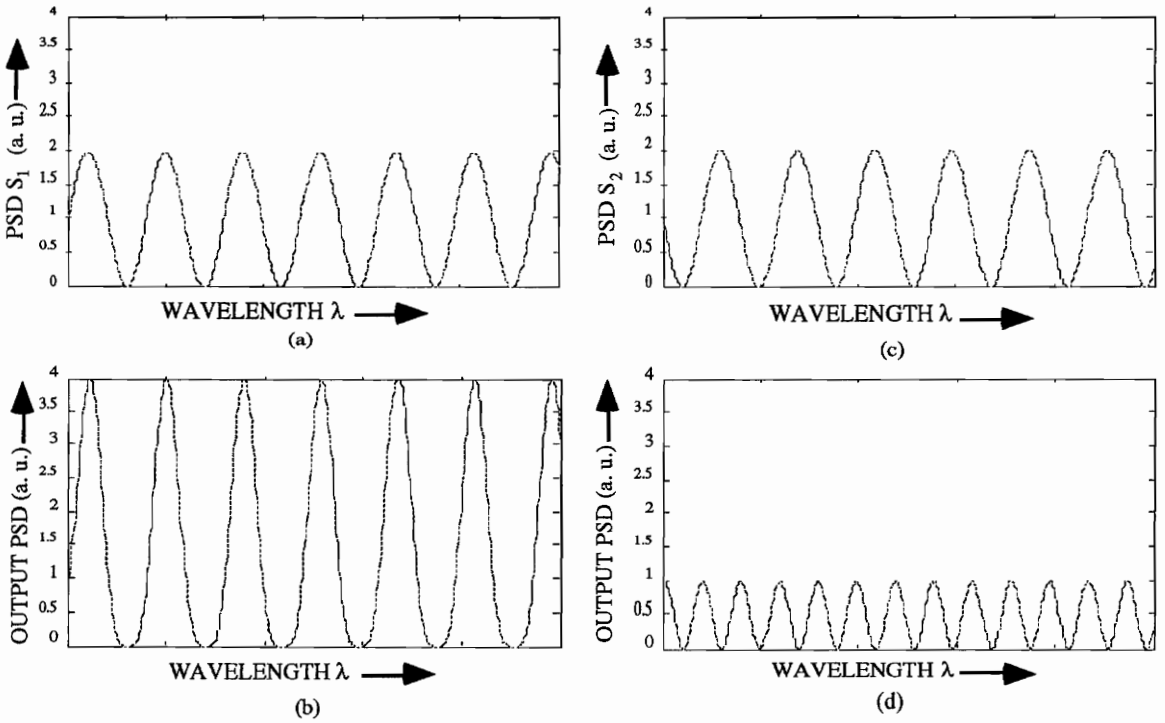

Figure 5.8. (a) Power Spectral Density (PSD) of the reference EFPI, (b) output PSD when the sensing and the reference EFPIs are path matched, (c) PSD of the sensing EFPI, π radians out of phase and (d) output PSD when the sensing and reference EFPIs are π radians out of phase.

Proof of concept experiments were performed in the laboratory to verify path matching. The reference EFPI was first set up in the reflected mode and then in the transmitted mode. Similar performance was observed in both configurations. The reference EFPI was set to a particular gap (greater than the coherence length of the SLED) while the sensing EFPI was

strained. For path matched sensing and reference EFPIs, an increase in the output was observed on the oscilloscope screen. Even slight variations (like 1-2 μm) from the path matched condition, led to a drastic drop in the fringe visibility. The envelope of the fringe pattern was found to be exponential. One of the reasons for the sharp drop in the visibility could be the higher value of the SLED spectral width (50 nm) as compared to that of the LED used by Lee and Taylor (30 nm). The cavity length of the reference EFPI was varied and path matching was obtained for a different gap in the sensing EFPI.

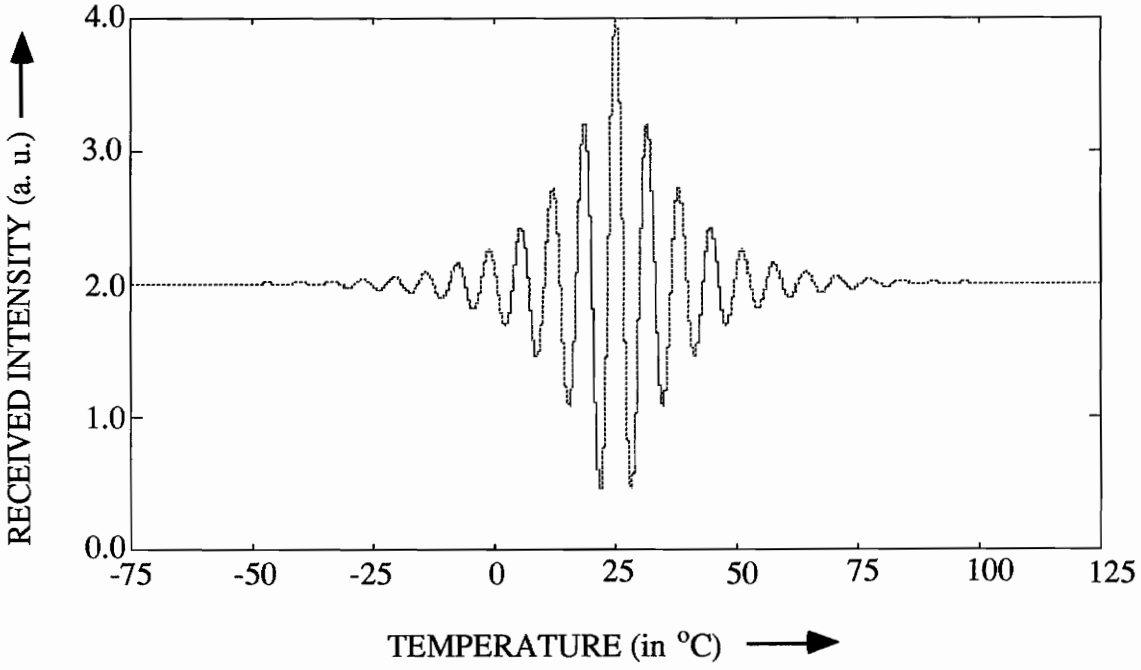

Figure 5.9. Typical change in intensity with temperature for path matching technique.

Belleville and Duplain [21] have described a strain sensor using path matching. They use a Fizeau interferometer to demodulate phase information from a sensing Fabry-Perot cavity (Figure 5.10). The cavity length in the Fizeau interferometer varies as along the position on the wedge. So there would be a position on it at which the distance between the glass plates is exactly equal to the cavity length d of the EFPI. A CCD array placed parallel to the Fizeau Interferometer would hence have an intensity distribution depending on d. If the pixel with the highest intensity can be tracked, real-time, absolute strain measurements are

possible. This sensor is reported to have a sensitivity of 0.25 με and a CCD scanning rate of 1 kHz.

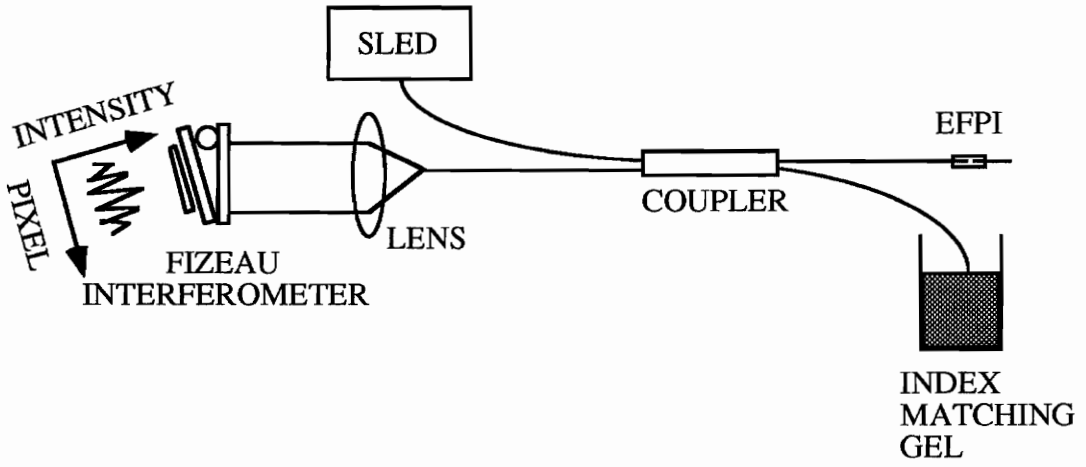

Figure 5.10. Setup for path matching using a Fizeau interferometer [21].

5.4 Relative Merits and Demerits of Signal Processing Techniques

Wavelength tuning requires a tunable laser diode, which should have a large dynamic range (about 90 nm for a 10 μm cavity length). Laser wavelength drifts due to surrounding temperature variations can also degrade the performance of the sensor. Moreover, the gap should remain fixed during the process the wavelength is being tuned. The advantage of employing wavelength tuning is that the signal processing becomes simpler and thus cheaper. This scheme can hence be utilized in conventional interferometric sensors to find the cavity length immediately after sensor fabrication. Wavelength shifting is the least expensive of all configurations of white light interferometry. It can be designed to have a high frequency response. The limitation of the wavelength shifting method is that it can only be used in applications which do not modulate the cavity length by a very large amount. Such a scheme requires a small cavity length and a separate calibration process for each sensor. Thus wavelength shifting is suitable for temperature and strain monitoring during the curing states of concrete and fiber composite samples.

Path matching is a simple to implement sensing scheme. The broadband source used does not require isolators, as do the laser sources in wavelength tuning. The biggest limitation of

path matching is that the reference interferometer is to be kept isolated from all external perturbations. Also for the setup used by Lee and Taylor, any deviation from the path matched condition leads to a decrease in the output intensity and like in conventional interferometers, extracting directional information about the applied perturbation becomes an impossible task. This drawback can be overcome by employing the Fizeau interferometer for demodulation which results in a spatial pattern instead of a temporal interference pattern. Bulk optic Michelson interferometers have also been commonly used as reference interferometers for path matching [22].

The constant phase technique described in Chapter 4 is independent of source intensity fluctuations and wavelength drifts. It possesses a large dynamic range and provides real time absolute information. It is self calibrating and there is no lower limit on the initial cavity length. Although wavelength shifting and path matching have better frequency response characteristics, the relative merits of the constant phase technique make it a prime candidate for applications requiring absolute perturbation detection.

Chapter 6 - White Light Interferometry in Elliptical-Core, Two-Mode Fibers

Two-mode, elliptical-core fibers have been demonstrated in the past for distributed sensing of strain, pressure, temperature and vibration [23]. But as in a conventional EFPI, the output from these sensors is not absolute and lacks directional information.

In this chapter we first review the theory behind the operation of two-mode, elliptical-core (e-core) fiber sensors. The limitations of this system are addressed and a theoretical model to extract absolute information from a two-mode, e-core fiber sensor using white light interferometry, is proposed. Experimental results are then analyzed and finally, other applications of white light interferometry to two-mode, e-core fibers are discussed.

6.1 Two-Mode, Elliptical-Core Fiber Sensors

A single mode, circular-core fiber operated just below its cutoff wavelength, allows the propagation of the LP_{11} modes along with the fundamental LP_{01} mode. Under the weakly-guiding approximation, two orthogonal polarizations of the LP_{01} mode and the four degenerate LP_{11} modes propagate along the length of the fiber. Although a two-lobe pattern is obtained at the output resulting from the complex interference occurring between these six linearly polarized modes, the measurement of any applied perturbation is difficult due to the instabilities in this pattern resulting from environmental disturbances.

The two-lobe pattern is stabilized with the use of highly elliptical-core fibers. In such fibers the degeneracy between the four higher order LP_{11} modes is lifted and they thus have different cut-off wavelengths. These four modes are now divided into two eigen-polarizations each of the LP_{11}^{odd} and LP_{11}^{even} modes. Just below the single mode cutoff wavelength only the two orthogonally polarized LP_{11}^{even} modes propagate along the fiber and for a large wavelength range (200-300 nm), the two LP_{11}^{odd} modes remain cutoff. Thus the modes that now propagate are the LP_{01}^{x}, LP_{01}^{y}, $LP_{11}^{even,x}$ and $LP_{11}^{even,y}$, where x and y denote the two orthogonal polarization axes. The interference between these four modes leads to an intensity modulation at the output far field that manifests itself in the form of

two output lobes which continuously exchange power, in a well described manner, for any applied perturbation.

For any arbitrary input polarization of monochromatic light if the intensity in any one of these two output lobes is monitored using a pinhole spatial detector, an amplitude modulation is observed in the obtained sinusoidal pattern. This amplitude modulation is due to the fact that polarization interference between the two orthogonally polarized modes (for each spatial mode) accompanies the modal interference between the spatial LP_{01} and LP_{11}^{even} modes. The output intensity, I, in any of the output far field lobes is given by,

$$I = I_{ac}\cos(\phi_i) , \tag{6.1}$$

where, I_{ac} is the maximum value of I and ϕ_i is the phase difference between the spatial or polarization modes,

$$\phi_i = \Delta\beta_i l . \tag{6.2}$$

Here $\Delta\beta_i$ (i = 1, 2, x, y) is the modal (i = 1, 2 for LP_{01}, LP_{11}^{even} modes, respectively) or polarization birefringence and, l, is the length of the fiber.

In a two mode fiber, $\Delta\beta_1 = \Delta\beta_{1x} - \Delta\beta_{1y}$ and $\Delta\beta_2 = \Delta\beta_{2x} - \Delta\beta_{2y}$ are the two polarization birefringences, while $\Delta\beta_x = \Delta\beta_{1x} - \Delta\beta_{2x}$ and $\Delta\beta_y = \Delta\beta_{1y} - \Delta\beta_{2y}$ are the two modal birefringences. Each of these birefringences has an associated beat-length $L_i = 2\pi/\Delta\beta_i$, where beat-length is defined as the change in fiber length required to obtain a 2π variation in ϕ_i.

If linearly polarized light is launched along either the major or the minor axis of the e-core fiber, the polarization birefringence is eliminated and only the similarly polarized (x or y) spatial modes interfere. The amplitude modulation in the output intensity pattern of a single lobe is now removed. The change in the phase difference $\delta\phi_i$ between the two spatial modes is given by,

$$\delta\phi_i = \delta(\Delta\beta_i)l + \Delta\beta_i\delta l , \tag{6.3}$$

where, $\delta(\Delta\beta_i)$ (i = x, y) is the change in the differential propagation constant and δl is the change in the length of the fiber. Figure 6.1 shows the output intensity in the far field as a function of ϕ_i. As is obvious any change in ϕ_i results in the intensity change in each of the output lobes and can be brought about by tuning the wavelength of operation (as β_i and hence $\Delta\beta_i$ is a function of wavelength) or by applying an external perturbation which changes both l and $\Delta\beta_i$. An important application of two-mode, e-core fibers is in the

measurement of the magnitude of wavelength shift in line sources utilizing the concept of change in the differential propagation constant with wavelength [24].

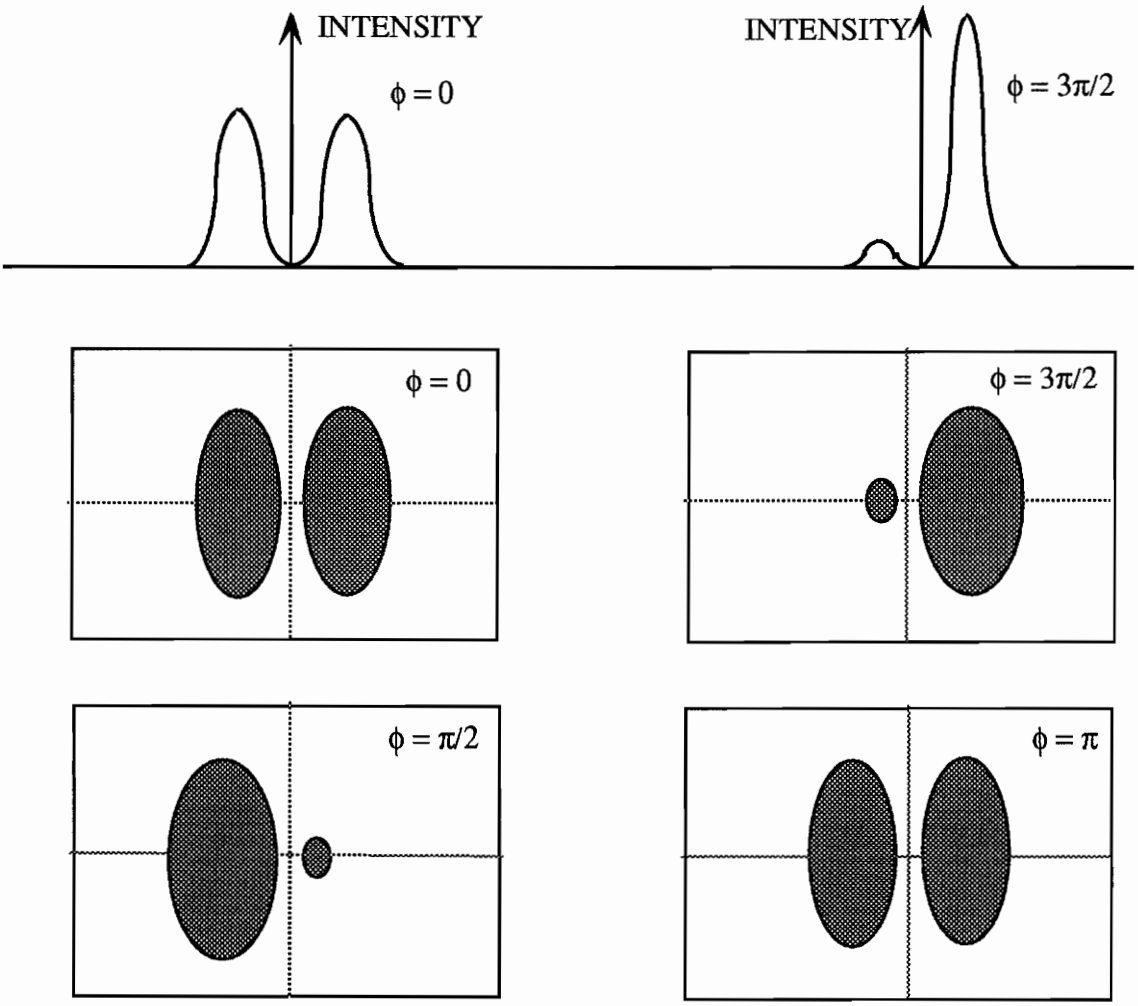

Figure 6.1. Output from a two-mode, elliptical-core fiber as a function of phase difference ϕ.

In the simplest terms, the output of one of the two lobes in a two-mode, e-core fiber can be described as that from a conventional EFPI using a line source. Thus, a two-mode, e-core fiber sensor suffers from the same limitations as a conventional EFPI. These include the inability to provide absolute and directional measurement and the loss of information if the

source is turned off. Thus the signal processing again becomes expensive due to the employment of either a feedback loop to maintain the Q-point or a fringe counter to measure the magnitude of a large perturbation. Also this system can only monitor dynamic perturbations and fails when static measurements are to be made. These factors have prevented the large-scale commercialization of two-mode, e-core fiber sensors to date.

6.2 Variation of the Differential Propagation Constant with Wavelength

The differential propagation constant ($\Delta\beta_i$, i = x, y) is a function of the wavelength of operation λ. The general variation of $\Delta\beta_x$ and $\Delta\beta_y$ is shown in Figure 6.2. The differential propagation constants for both the eigen polarizations initially increase with wavelength, reach a peak and finally drop down to a low value. $\Delta\beta_x$ is less than $\Delta\beta_y$ for all the values of λ since the beat-length along the major axis is more than that along the minor axis. For input light at any orientation other than that along the major or minor axis, $\Delta\beta$ lies between the two curves of Figure 6.2.

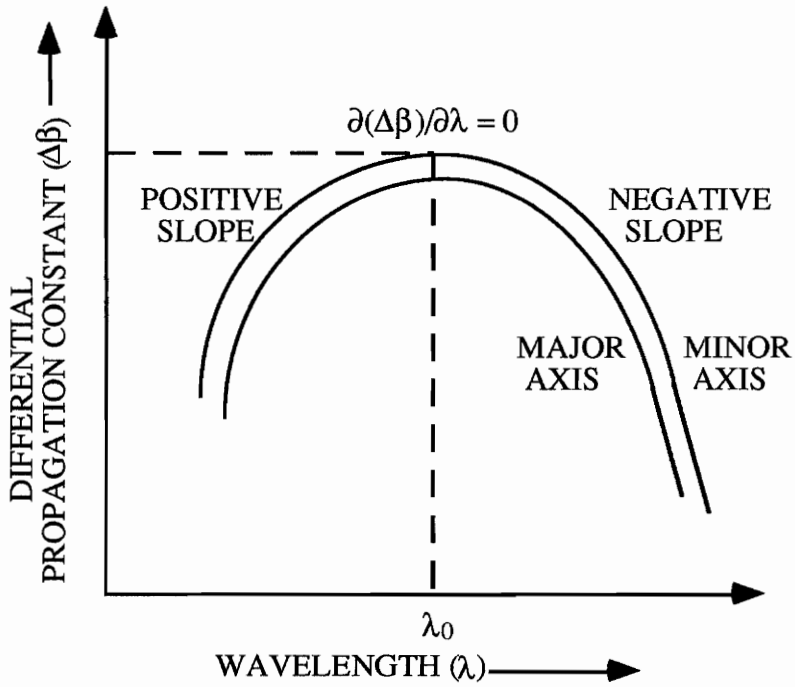

Figure 6.2. Typical variation of the differential propagation constant ($\Delta\beta$) with wavelength (λ) along the major and minor axis for a two-mode, elliptical-core fiber [24].

6.3 White Light Interferometry

Many of the problems encountered while using a conventional EFPI were surmounted when it was used in white light interferometry configuration (Chapter 4). Using white light interferometry the limitations of two-mode, e-core fibers listed in Section 6.2 can also be overcome. That is, if a broadband optical source is used to illuminate a two-mode, e-core fiber and if the output from one of the lobes is monitored on the OSA, a pattern similar to that from the AEFPI would be obtained. To confirm this concept, a white light source was used at the input and the output was obtained on the OSA. Although an intensity modulation was obtained, the fringe pattern was not very smooth due to the low signal to noise ratio at the output. To overcome this problem a SLED was used as the source but when the output far-field pattern was projected on a white sheet of paper, instead of two elliptical lobes only a single, almost circular lobe was observed. The presence of a single lobe is due to the fact that the two lobes are "washed-out" by the presence of all the wavelengths and this gives rise to a single circular lobe. Also for a certain part of the spectrum of the SLED, the e-core fiber in use was three mode and the presence of this third mode could have resulted in the circular pattern at the output far field.

The intensity in the two lobes, I_1 and I_2 for a single wavelength can be said to be complementary, *i.e.* ,

$$I_1 + I_2 = I \,, \tag{6.4a}$$

where, I is the input intensity and all losses in the fiber are ignored. This can be compared to the reflection and transmission patterns in the AEFPI. Neglecting absorption and other losses, for each wavelength, we get,

$$T + R = I_0 \,, \tag{6.4b}$$

where, I_0 is the input intensity and T and R are the transmitted and reflected intensities at that wavelength. We can thus conclude that if the whole lobe obtained from the two-mode, e-core fiber is monitored on the OSA, we would simply obtain the spectrum of the SLED. This observation was confirmed when the entire lobe was allowed to fall on the detector face of the OSA and no intensity modulation was observed. This condition corresponds to monitoring the sum of the transmitted and reflected intensities in an EFPI and thus at each wavelength this sum is constant because of the two anti-phase components.

If the spatial output from the fiber is so selected that only a part of the circular lobe impinges on the detector face then fringes would be obtained in the wavelength domain,

provided the part that is chosen contains unequal portions of the two lobes obtained at any single wavelength. This fact is more obvious if we see Figure 6.3.

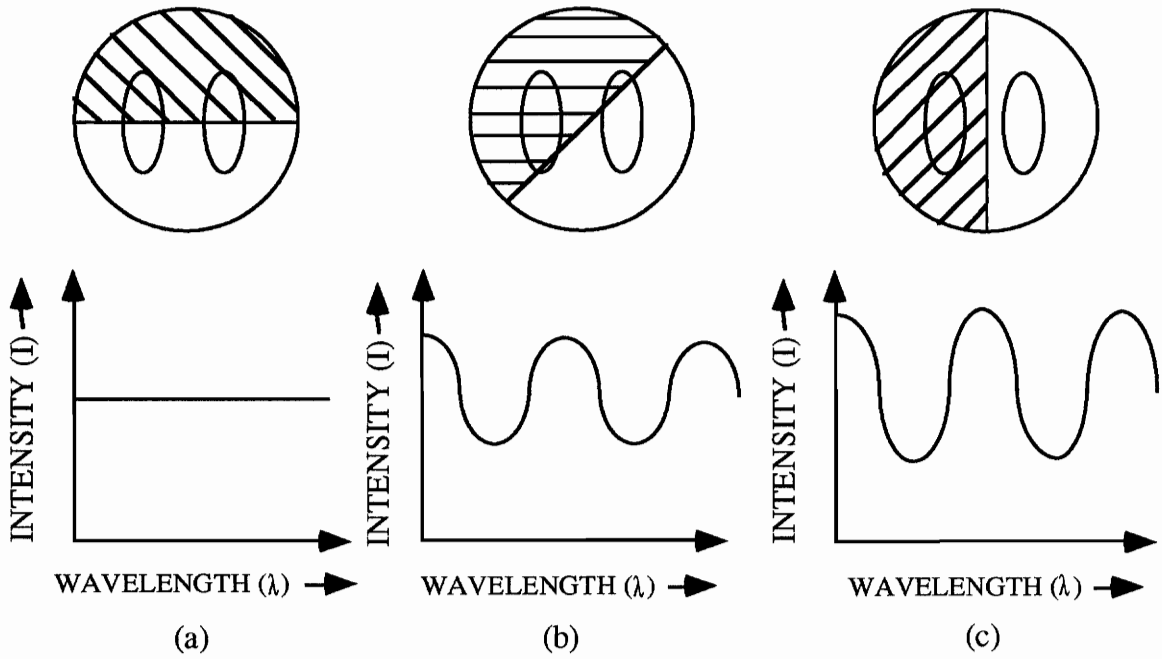

Figure 6.3. Intensity variations (bottom) depending on the selection of the far field output (top).

If we choose the portion highlighted in Figure 6.3(a), the output intensities from the two lobes would add up to be constant at any wavelength. In Figure 6.3(b), since unequal portions of the two lobes are considered, different wavelengths have different intensities and an intensity modulation is obtained at the output. Finally, as seen in Figure 6.3(c), if only that part of the circular lobe which has a single elliptical lobe is allowed on the OSA detector, maximum fringe contrast is obtained for the output fringe pattern. Thus, the selection of the output determines the fringe contrast on the OSA. If θ be the angle of a line m with respect to the line joining the center of the two lobes n, and if the output is so chosen that it always lies above m for $0° < \theta < 90°$ and below m for $90° < \theta < 180°$, as shown in Figure 6.4(a), then the fringe contrast F will vary as shown in Figure 6.4(b).

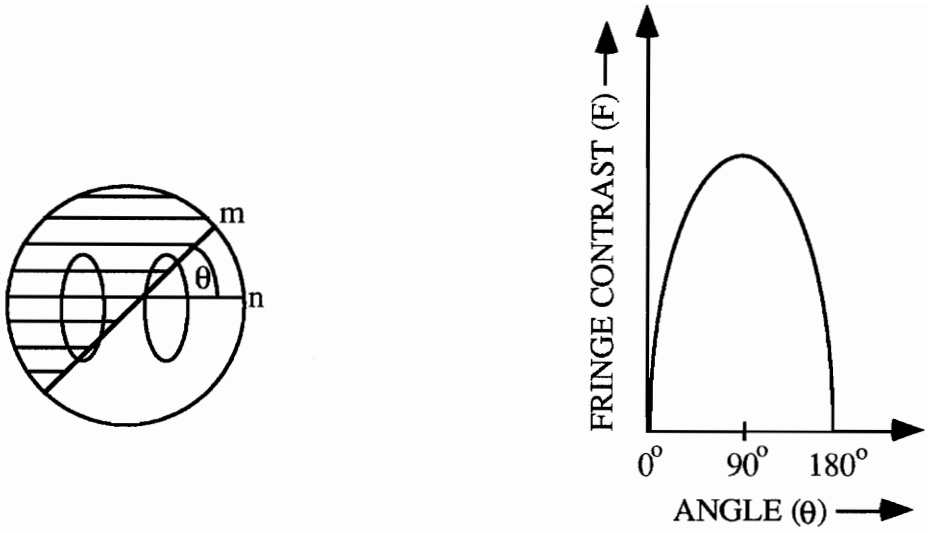

Figure 6.4. Variation of the fringe contrast (F) as a function of the angle (θ).

Huang *et al.* [25] have obtained expressions for output phase change with axial strain and temperature change at a single wavelength (633 nm). These expressions can also be applied to wavelengths around 830 nm with a slight change in numerical constants.

6.3.1 Axial Strain

The change in the output phase difference $\delta\phi_i$ with change in axial length δl is given by [25],

$$\frac{\delta\phi_i}{\delta l} = 0.953\Delta\beta_i + 0.605\lambda\frac{\partial(\Delta\beta_i)}{\partial\lambda}. \tag{6.5}$$

If we can find two wavelengths, λ_1 and λ_2, that differ in phase by $2n\pi$, (n is a whole number),

$$\delta l = \frac{2n\pi}{0.953(\Delta\beta_{i,1} - \Delta\beta_{i,2}) + 0.605\left(\lambda_1\left[\frac{\partial(\Delta\beta_i)}{\partial\lambda}\right]_{\lambda_1} - \lambda_2\left[\frac{\partial(\Delta\beta_i)}{\partial\lambda}\right]_{\lambda_2}\right)}, \tag{6.6}$$

where, $\Delta\beta_{i,1}$ and $\Delta\beta_{i,2}$ are the differential propagation constants at λ_1 and λ_2,

respectively, and $\left[\frac{\partial(\Delta\beta_i)}{\partial\lambda}\right]_{\lambda_1}$ and $\left[\frac{\partial(\Delta\beta_i)}{\partial\lambda}\right]_{\lambda_2}$ are the slopes of the differential propagation curve with respect to(w. r. t.) wavelength at λ_1 and λ_2, respectively. Thus to find the value of axial strain $\delta l/l$ we need to know the slope of the $\Delta\beta_i$ curve w. r. t. wavelength at λ_1 and λ_2 and the difference in the values of $\Delta\beta_i$ at λ_1 and λ_2.

6.3.2 Temperature Changes

The change in phase difference, $\delta\phi_i$, due to temperature change, δT, is given by [25],

$$\frac{\delta\phi_i}{\delta T} = -1.05\lambda\left[\frac{\partial(\Delta\beta_i)}{\partial\lambda}\right]. \tag{6.7}$$

Again if we can find two wavelengths λ_1 and λ_2 such that they differ in phase by $2n\pi$, we have,

$$\delta T = \frac{2n\pi}{1.05\left(\lambda_2\left[\frac{\partial(\Delta\beta_i)}{\partial\lambda}\right]_{\lambda_2} - \lambda_1\left[\frac{\partial(\Delta\beta_i)}{\partial\lambda}\right]_{\lambda_1}\right)}. \tag{6.8}$$

To determine the temperature change we need the value of the slope of $\Delta\beta_i$ curve w. r. t. wavelength at λ_1 and λ_2.

6.4 Experimental Determination of Axial Strain and Temperature Changes

To determine axial strain and temperature we require the variation of the differential propagation constant with the operating wavelength. The setup shown in Figure 6.5 was used to estimate this curve.

A SLED (at 830 nm) was used to launch light in an elliptical-core fiber, with a 1050 nm single mode cutoff wavelength. No attempt was made to launch light along the axes of the e-core fiber. The output was monitored on the OSA and the output end of the fiber was moved around using a positioner until maximum fringe contrast was obtained on the OSA.

Figure 6.6 shows such plots obtained on the OSA for different values of fringe contrast in an unperturbed fiber. If no perturbation is applied to the e-core fiber, we obtain from Equation 6.3,

$$\frac{\delta\phi_i}{\delta\lambda} = \frac{\partial(\Delta\beta_i)}{\partial\lambda}1. \tag{6.9}$$

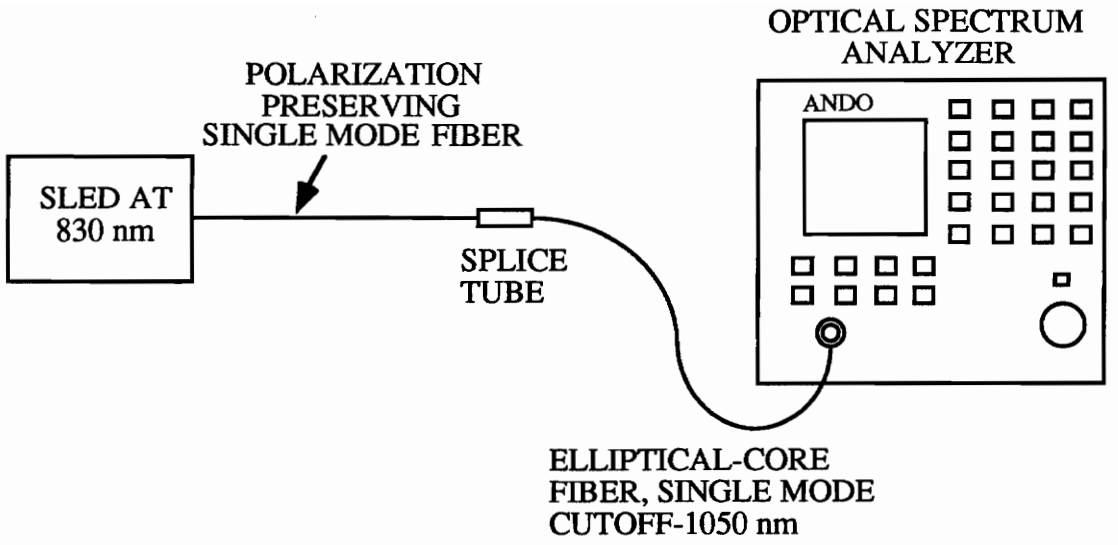

Figure 6.5. Setup to determine the variation of the differential propagation constant ($\Delta\beta$) with wavelength (λ).

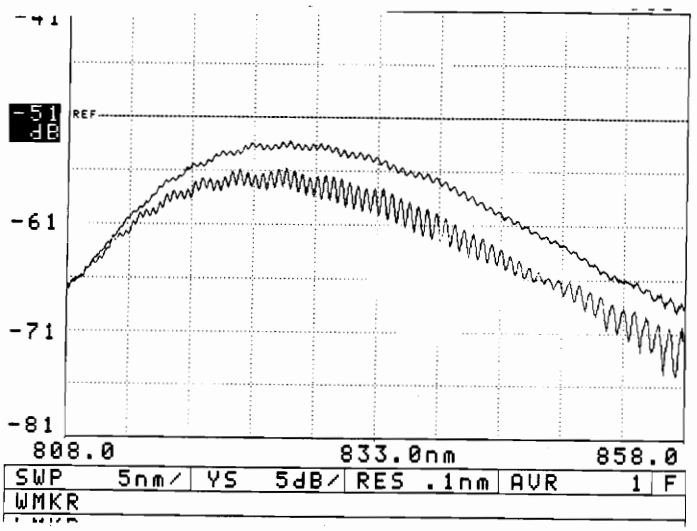

Figure 6.6. Different fringe contrasts at the output far field from the same unperturbed fiber by selecting different portions of the output lobe.

If we can find two wavelengths, λ_3 and λ_4, which are 2π apart in phase,

$$\frac{\partial(\Delta\beta_i)}{\partial\lambda} = \frac{2\pi}{1}\frac{1}{\Delta\lambda}, \tag{6.10}$$

where, $\Delta\lambda = \lambda_4 - \lambda_3$. This would give us the value of the slope of the differential propagation curve at the average wavelength $(\lambda_3 + \lambda_4)/2$. A typical plot for the slope versus the wavelength is shown in Figure 6.7. As is expected, this slope is at first positive, and then after a certain wavelength λ_0, becomes negative. The approximate wavelength λ_0 at which this slope goes to zero is obtained by interpolation. For the fiber used this wavelength was 914 nm for the arbitrary input polarization. The value of the slope could not be determined for the complete two-mode domain of the fiber used as the spectral width of the SLED was limited.

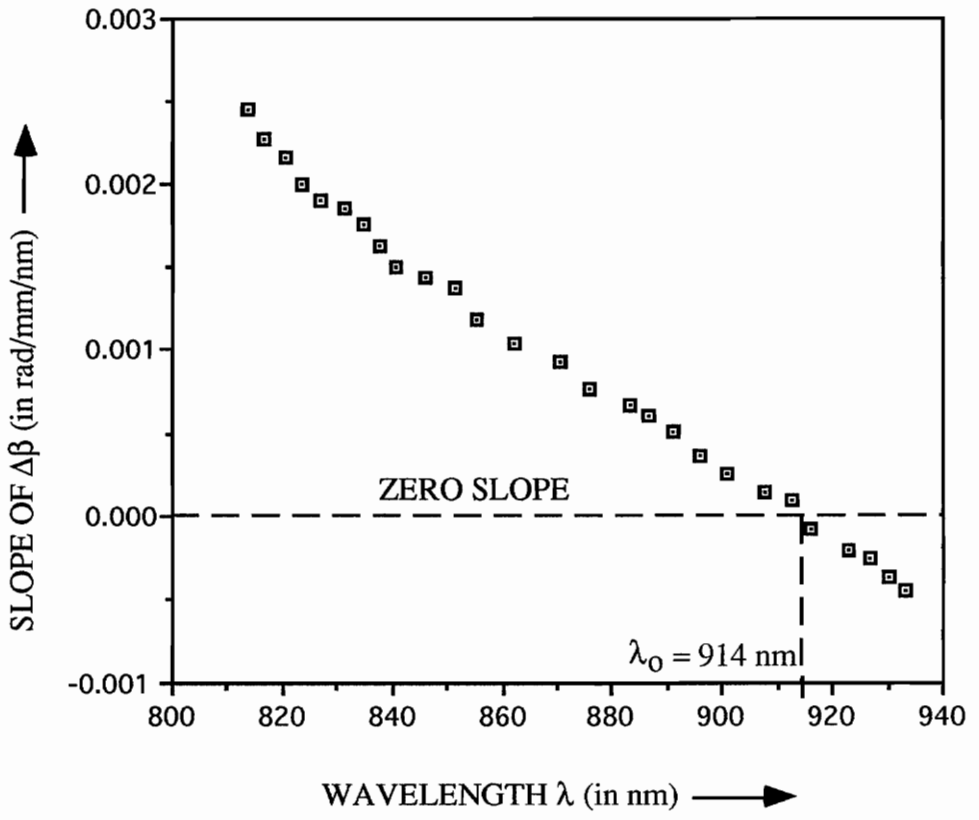

Figure 6.7. Slope of the differential propagation constant curve with wavelength for an arbitrary input polarization.

The value of the differential propagation constant at a wavelength λ_t is found as follows,

$$\Delta\beta_i = \Delta\beta_0 - \left[\frac{\partial(\Delta\beta_i)}{\partial\lambda}\right]_{\lambda_t} (\lambda_0 - \lambda_t), \qquad (6.11)$$

where, $\left[\frac{\partial(\Delta\beta_i)}{\partial\lambda}\right]_{\lambda_t}$ is the value of the slope of the differential propagation constant curve at the wavelength λ_t and $\Delta\beta_0$ is the value of $\Delta\beta$ at the zero slope wavelength λ_0. So to find the absolute variation of $\Delta\beta$ with wavelength we need to know its value at λ_0 or at any other wavelength in the dual mode region. Figure 6.8 shows the variation in $\Delta\beta$ from the value at λ_0 as a function of wavelength λ. It simply is the plot of the second term in the right hand side of Equation 6.11.

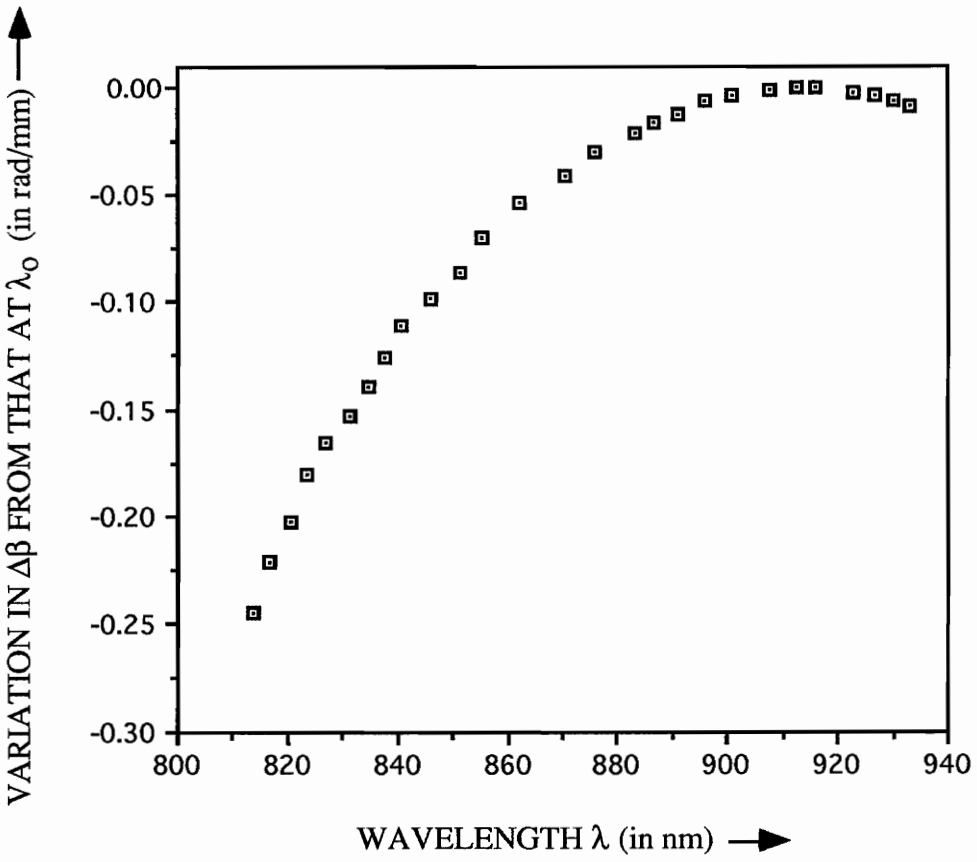

Figure 6.8. Variation of the differential propagation constant ($\Delta\beta$) from the value at λ_0 as a function of wavelength (λ) for Andrew elliptical-core fiber.

To find the exact curve one has to first determine $\partial(\Delta\beta_i)/\partial\lambda$ from the technique described above and then strain the fiber at a single wavelength for the same input polarization as used to determine the slope. Straining the fiber would yield the beat length L_B and hence the propagation constant at the wavelength of operation,

$$L_B = \frac{2\pi}{\Delta\beta}, \tag{6.12}$$

or,

$$\Delta\beta = \frac{2\pi}{L_B}. \tag{6.13}$$

Then again by employing Equation (6.11) we can find the variation of $\Delta\beta$ with wavelength. This can then be used to determine axial strain and temperature changes from Equations (6.6) and (6.8).

Figures 6.9 (a) and (b) show plots of unstrained and strained fibers for different values of applied strain (on left) and the differences of the corresponding outputs (on right). The strain applied was arbitrary and no effort was made to quantify it. As is expected the intensity at each wavelength shifts changes due to the phase change from the applied axial strain. The difference output is sinusoidal, which is to be expected since the two outputs on the left are also sinusoidal. We can also use the wavelength shifting technique described in Chapter 5 to determine axial strain and temperature by simply monitoring the shift in a certain peak due to perturbation effects.

6.5 Other applications of White Light Interferometry to Two-Mode, Elliptical-Core Fibers

Apart from axial strain and temperature measurements, white light interferometry can also be employed in two-mode, elliptical-core fibers for a large number of other applications, such as those discussed in this section.

6.5.1 Determination of Zero Temperature and Strain Sensitivity Wavelengths

As is obvious from Equation 6.5, $\delta\phi_i/\delta l$ falls to zero at the wavelength λ_ε,

$$\Delta\beta_i = -0.635\lambda_\varepsilon\left[\frac{\partial(\Delta\beta_i)}{\partial\lambda}\right]_{\lambda_\varepsilon}. \tag{6.14}$$

If this wavelength λ_ε exists in the two-mode region, it should lie to the right of the zero

slope wavelength λ_0, where the slope is negative. We can fabricate special fibers which have a zero strain sensitivity wavelength in the two-mode domain. Also from Equation (6.7), the temperature sensitivity falls to zero at the zero slope wavelength λ_0.

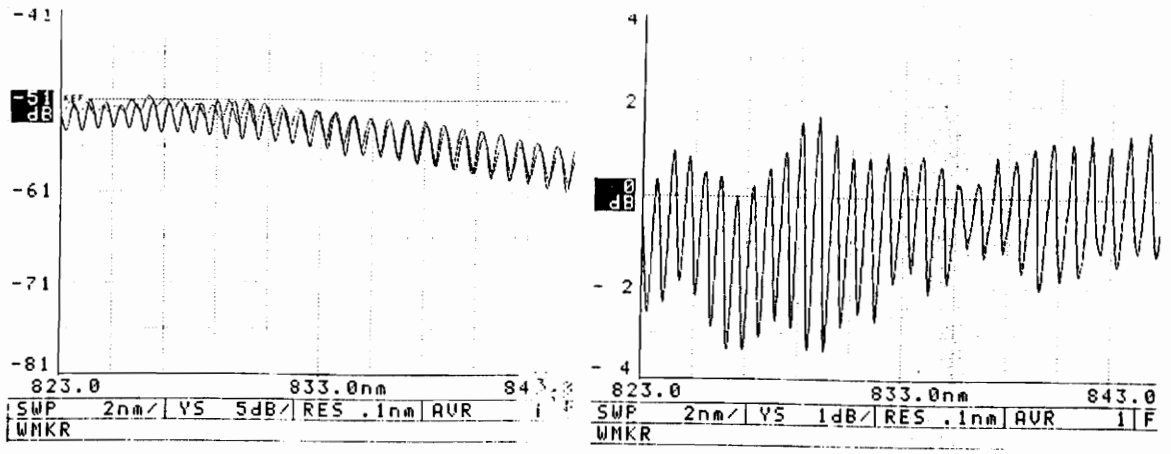

(a)

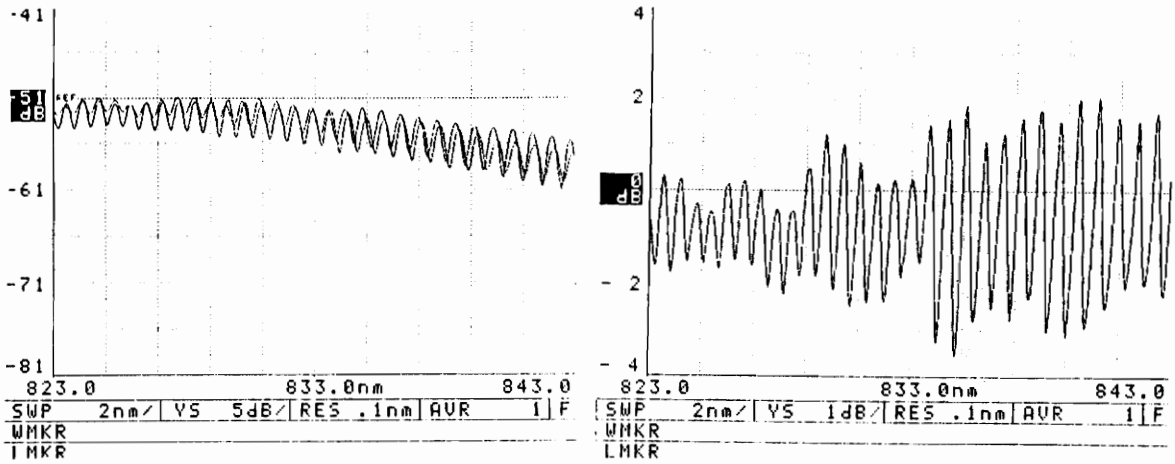

(b)

Figure 6.9. Outputs from the ANDO OSA for unstrained and strained fiber (left) and the difference between the unstrained and strained (right). (a) and (b) are the outputs for two different arbitrary values of applied strain.

Although theoretically the axial strain and temperature sensitivities are zero at λ_ε and λ_0 respectively, some effect of these perturbations still exists at these wavelengths due to variations from the model assumed in [25]. But still this effect is minimum at λ_ε and λ_0 and so this would help researchers develop two-mode, e-core fiber sensors which are sensitive to only axial strain at λ_0 and to only temperature at λ_ε. Thus, cross sensitivity between these parameters at these wavelengths is minimized.

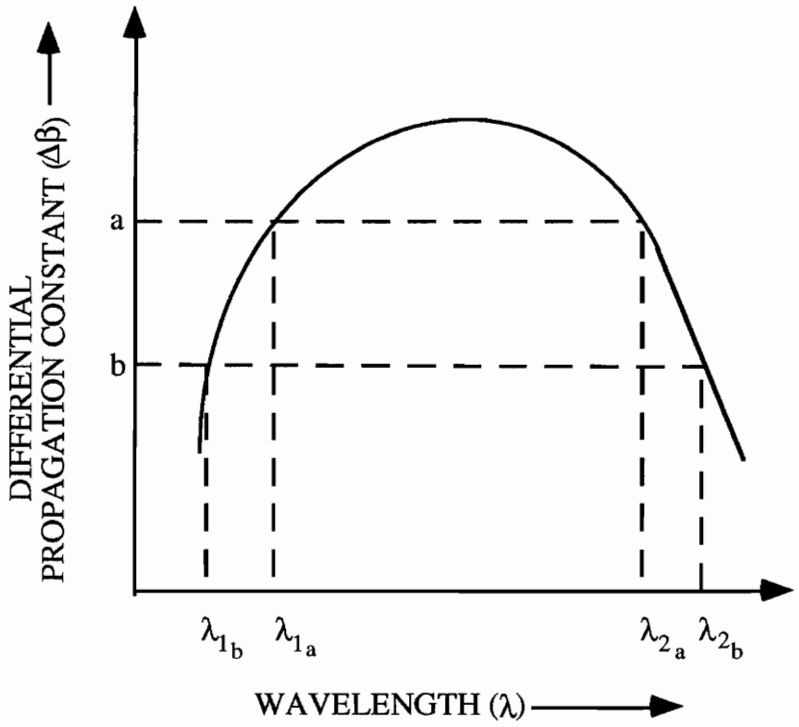

Figure 6.10. Determination of two wavelengths (λ_1 and λ_2) with the same differential propagation constant ($\Delta\beta$).

6.5.2 Application to Photoinduced Refractive Index Gratings

Two-mode, elliptical-core fibers have been used in the past [26] to induce permanent refractive index changes, termed as "gratings", in the fiber core for strain measurements. The gratings are "burnt" into the fiber using an intense high powered beam, in the two-mode region by utilizing the interference between the spatial LP_{01} and LP_{11}^{even} modes. This

causes beat length changes in the fiber depending on the $\Delta\beta$ versus wavelength λ curve for the orientation along which linearly polarized light is launched. The gratings are induced in the fiber by generally using a high powered laser (like the argon-ion laser at 40 mW) and perturbation sensing is implemented by interrogating the fiber at low power levels (about 2 mW). If the perturbation sensing is to be done at a remote site, it becomes cumbersome to move the heavy laser source and the associated equipment. But if we have the value of the differential propagation constant at different values of wavelength, we can find another higher wavelength, λ_2, at which the value of $\Delta\beta$ is the same as that at the wavelength, λ_1, (at which the grating is created), as seen in Figure 6.10. This wavelength can be in the semiconductor laser range and so we can use cheaper and portable sources to facilitate field measurements.

6.5.3 Determination of the Exact Fundamental Mode Cutoff Wavelength

Alavie and Grossman [27] have determined the exact cutoff wavelength of the LP_{01} mode in elliptical-core fibers by using a tunable laser source to find the modulation index of the interference between the LP_{01} and the LP_{11}^{even} modes. At the wavelength at which the modulation index becomes a very small value, the LP_{01} mode is said to be cut off.

To determine experimentally the exact cutoff wavelength of the LP_{01} mode in an e-core or even a circular core fiber, we need a broadband source, preferably a SLED, centered around the approximate cutoff wavelength of the fiber. The degeneracy of the polarization modes in LP_{01} and LP_{11}^{even} spatial modes is removed in an e-core fiber and hence the polarization eigen-modes have different cutoff wavelengths. Thus linearly polarized light has to be launched along the axis for which we need to determine the cutoff wavelength. The input polarization can be deduced by examining the output on the OSA for any presence of amplitude modulation. A halfwave plate can be used at the input to rotate the incoming polarization until the observed amplitude modulation vanishes. The modulation index is determined by calculating the number of output fringes in a fixed wavelength window, say 5 nm.

The wavelength at which this modulation index falls below a fixed low value, is the single mode cutoff wavelength of the LP_{01} mode. This value is important in applications where one wants to operate the fiber at a wavelength close to the single mode cutoff but away from the two-mode wavelength region. For example in optical communication systems to

reduce the intensity losses due to bends during fiber installation, the system is operated near the single mode cutoff wavelength, as the majority of the propagating energy is then confined to the core. A typical plot of the two-mode modulation depth versus wavelength is depicted in Figure 6.11 [27].

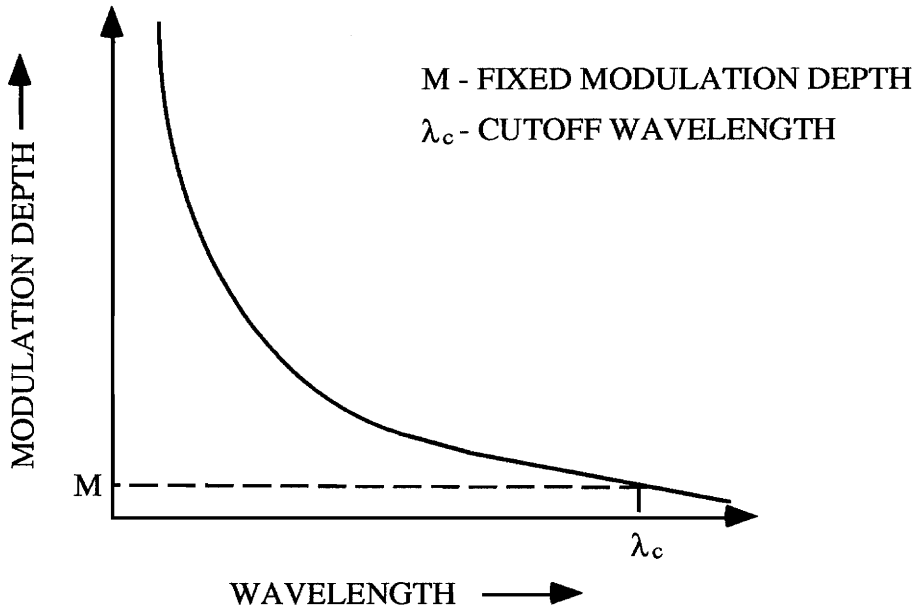

Figure 6.11. Two-mode modulation depth as a function of wavelength [27].

In all the applications discussed above it is necessary to get the best fringe contrast for the output on the OSA. For this we need to isolate one of the two output lobes. But since the output elliptical lobes are washed out due to the broadband source, we need a method to determine the spatial location of these lobes in the output far field. This can be done by placing an optical filter having a small bandwidth (2-4 nm) between the SLED and the fiber under investigation and then isolating a single lobe using a pin-hole spatial filter. Once this has been done the filter can be removed and maximum fringe contrast is obtained on the OSA screen.

To our knowledge, the work described in this chapter is a pioneering step in attempts to extract absolute information regarding applied perturbations in two-mode, elliptical-core

fibers. Thus white light interferometry in two-mode, e-core fibers is at present in a rudimentary state and prodigal magnitudes of research and development efforts are required in order to commercialize this technology for sensing and other mentioned applications.

Chapter 7 - Conclusions

An absolute strain and temperature sensing system based on the principle of white light interferometry has been developed. It uses a broadband light source and consists of a spectrum analyzer to demodulate information from the sensing head. The strain sensor, which can have either an EFPI or a TIMI as the sensing interferometer, is self-calibrating and has a resolution of 100 με. The temperature sensor requires calibration and possesses a resolution of 2 °C. Both these sensors give real-time outputs and have a large dynamic range. Thus most of the features desired in an ideal fiber optic sensor are available in this system. The limitations of this system include a low detectable strain and temperature rates. Thus the system can only be used in applications where the strain or temperature varies slowly with time. The applications could include monitoring of strain and temperature changes in concrete and composite curing processes. These sensors could also be embedded inside civil and military structures such as buildings, ships and aircraft to detect strain and temperature variations during the life-time of these structures.

Other techniques for signal processing in white light interferometry have been discussed and compared. Of these, path matching and intensity peak shift (or wavelength shifting) hold the most potential. Path matching is technique which can be employed in low cost temperature and strain sensing. Wavelength shifting can be used in applications where the perturbation to be measured undergoes only a small change in magnitude. For wavelength shifting the EFPI cavity length should just be a few microns, while the limitation of path matching is that the reference interferometer has to be kept independent of the measurand.

White light interferometry in two-mode, elliptical fibers is introduced. Novel methods for distributed strain and temperature sensing have been proposed. Applications to photoinduced refractive index gratings and to characterization of dual-mode fibers have also been discussed.

Future directions

The frequency response of the AEFPI system can be improved by using a better spectrum analyzer with a smaller integration time. This implies that the system would then conform to desired industry standards for strain and temperature sensors. Techniques like path matching and wavelength shifting should be subjected to detailed investigation in order to develop these into commercially available products.

Of the work described here, white light interferometry in two-mode, elliptical-core fibers appears to be most promising. Its applications to strain and temperature sensing, two-mode gratings and fiber characterization should be evaluated and compared to existing techniques in terms of performance and cost.

References

1. J. Dakin and B. Culshaw, Optical Fiber Sensors: Principles and Components, Artech House, MA, 1988.

2. T. G. Giallorenzi, J. A. Bucaro, A. Dandridge, G. H. Sigel, Jr., J. H. Cole, S. C. Rashleigh, and R. G. Priest, "Optical fiber sensor technology," *IEEE Journal of Quantam Electronics*, vol. 18, pp. 626-665, 1982.

3. A. Wang, A. Plante, V. Bhatia, K. A. Murphy, and R. O. Claus, "Split-Spectrum intensity based optical fiber sensors," *FEORC Fiber Optics Review Conference*, Blacksburg, VA, April 1993.

4. A. Wang, S. Gollapudi, K. A. Murphy, R. G. May, and R. O. Claus, "Sapphire-fiber-based intrinsic Fabry-Perot interferometer," *Optics Letters*, vol. 17, pp. 1021-1023, 1992.

5. C. E. Lee and H. F. Taylor, "Fiber-optic Fabry-Perot temperature sensor using a low-coherence light source," *Journal of Lightwave Technology*, vol. 9, pp. 129-134, 1991.

6. R. O. Claus, M. F. Gunther, A. Wang, and K. A. Murphy , "Extrinsic Fabry-Perot sensor for strain and crack opening displacement measurements from -200 to 900 °C," *Smart Materials and Structures*, vol. 1, pp. 237-242, 1992.

7. K. A. Murphy, M. F. Gunther, A. M. Vengsarkar, and R. O. Claus, "Quadrature phase-shifted, extrinsic Fabry-Perot optical fiber sensors," *Optics Letters*, vol. 16, pp. 273-275, 1991.

8. M. Johnson, "White light interferometry," *Proceedings of the SPIE Conference on Fiber Optics*, vol. 1314, pp. 307-314, September 1990.

9. B. R. Fogg, A. Wang, M. S. Miller, K. A. Murphy, and R. O. Claus, "Optical fiber sensor for absolute measurement," *FEORC Fiber Optics Review Conference*, Blacksburg, VA, 1992.

10. C. E. Lee, W. N. Gibler, R. A. Atkins, and H. F. Taylor, "In-line fiber Fabry-Perot interferometer with high reflectance internal mirrors," *Journal of Lightwave Technology*, vol. LT-4, pp. 382-385, 1986.

11. J. Stone and D. Marcuse, "Ultrahigh finesse fiber Fabry-Perot interferometers," *Journal of Lightwave Technology*, vol. 10, pp. 1376-1379, 1992.

12. M. Born and E. Wolf, Principles of Optics, Pergamon Press, New York, 1985.

13. C. Dufour and R. Picca, *Rev. d' Opt.*, vol. 24, p. 19, 1945.

14. R. Chabbal, *J. Rech. Cent. Nat. Rech. Sci.*, Bellevue (Paris), vol. 24, p. 138, 1953.

15. O. S. Heavens, Optical properties of thin film solids, pp. 76-77, 1955.

16. T. A. Tran, J. A. Greene, M. S. Miller, V. Bhatia, K. A. Murphy, A. Wang, and R. O. Claus, "Absolute strain measurements using the extrinsic Fabry-Perot interferometer," *FEORC Fiber Optics Review Conference*, Blacksburg, VA, April 1993.

17. OEM Interface Guide, Ocean Optics, Dunedin, Florida.

18. K. A. Murphy, W. V. Miller III, T. A. Tran, A. M. Vengsarkar, and R. O. Claus, "Miniaturized fiber-optic Michelson-type interferometric sensors," *Applied Optics*, vol. 30, pp. 5063-5067, 1991.

19. J. A. McClintock and J. P. Andrews, "Fabry-Perot readout technique using wavelength tuning," Martin Marietta Aero and Naval Systems, Baltimore, MD.

20. S. F. Masri and R. O. Claus, "Developments in actuators and sensors for structural response under seismic and dynamic loads," *U.S.-Japan Seminar on Experimental Methods in Earthquake Engineering*, Honolulu, Hawaii, 1993.

21. C. Belleville and G. Duplain, "White light interferometric multimode fiber optic strain sensor," *Optics Letters*, vol. 18, pp. 78-80, 1993.

22. G. Zuliani, D. Hogg, Kexing Liu, and R. M. Measures, "Demodulation of a fiber Fabry-Perot strain sensor using white light interferometry," *Proceedings of the SPIE Conference on Fiber Optic Smart Structures and Skins IV*, vol. 1588, pp. 308-313, September 1990.

23. K. A. Murphy, M. S. Miller, A. M. Vengsarkar, and R. O. Claus, "Elliptical-core, two-mode optical-fiber sensor implementation methods," *Journal of Lightwave Technology*, vol. 8, pp. 1688-1696, 1990.

24. V. Bhatia, A. Wang, G. Z. Wang, K. A. Murphy, and J. A. Greene, "Elliptical-core, two-mode wavelength division multiplexer," *FEORC Fiber Optics Review Conference*, Blacksburg, VA, April 1993.

25. S. Y. Huang, J. N. Blake, and B. Y. Kim, "Perturbation effects on mode propagation in highly elliptical core two-mode fiber," *Journal of Lightwave Technology*, vol. 8, pp. 23-33, 1990.

26. A. M. Vengsarkar, J. A. Greene, and K. A. Murphy, "Photoinduced refractive-index changes in two-mode, elliptical-core fibers: sensing applications," *Optics Letters*, vol. 16, pp. 1541-1543, 1991.

27. A. T. Alavie and B. G. Grossman, "Accurate measurement of effective cutoff in elliptical-core fibers," *Optics Letters*, vol. 18, pp. 343-345, 1993.

Vita

Vikram Bhatia was born in Srinagar, India on August 9, 1970. He graduated with a B. E. in Electronics and Communication Engineering from the Birla Institute of Technology, Ranchi in May 1992. He joined the Fiber and Electro-Optics Research Center at Virginia Tech as a Graduate Research Assistant in September 1992. Mr. Bhatia received his M. S. from the Bradley Department of Electrical Engineering in 1993.

He is a member of the IEEE and his professional interests include fiber optic sensing and communication.

Vikram Bhatia.